

Electronic excitations in light absorbers for photoelectrochemical energy conversion: first principles calculations based on many body perturbation theory†

Yuan Ping,^{‡a} Dario Rocca^{‡§b} and Giulia Galli^{*c}

Cite this: *Chem. Soc. Rev.*, 2013, **42**, 2437

Received 10th January 2013

DOI: 10.1039/c3cs00007a

www.rsc.org/csr

We describe state of the art methods for the calculation of electronic excitations in solids and molecules, based on many body perturbation theory, and we discuss some applications of these methods to the study of band edges and absorption processes in representative materials used as photoelectrodes for water splitting.

1 Introduction

The production of hydrogen and oxygen from water through photoelectrochemical energy conversion is a promising strategy to take advantage of the Earth's main energy source, the Sun.^{1,2}

For example, upon absorption of sunlight by a semi-conducting electrode (*e.g.* a solid oxide) interfaced with liquid water, electron–hole pairs may be formed, leading to coupled electron–proton transfers at the interface and eventually to water splitting. One of the challenges in the optimization of this process is to find Earth abundant and stable materials that are at the same time efficient absorbers of sunlight (*e.g.* direct band gap semiconductors absorbing mostly in the visible), and have band edges appropriately aligned with water reduction and oxidation potentials to permit efficient proton-coupled electron transfer reactions. Therefore, from a theoretical standpoint, an essential prerequisite to predict materials for photoelectrochemical energy conversion is the development of efficient methods to describe electronic excitation in solids and molecules.

^a Department of Chemistry, University of California, Davis, Davis, 95616, USA. E-mail: yping@ucdavis.edu

^b Department of Chemistry, University of California, Davis, Davis, 95616, USA

^c Department of Chemistry and Department of Physics, University of California, Davis, Davis, 95616, USA. E-mail: gagalli@ucdavis.edu

† Part of the solar fuels themed issue.

‡ These authors contributed equally to this work.

§ Present address: Université de Lorraine, CRM², UMR 7036, Institut Jean Barriol, 54506 Vandoeuvre-lès-Nancy, France; CNRS, CRM², UMR 7036, 54506 Vandoeuvre-lès-Nancy, France.



Yuan Ping

Yuan Ping received her BSc degree in Chemical Physics at the University of Science and Technology of China, in 2007. She is currently a graduate student in the Chemistry Department of the University of California, Davis and scheduled to graduate in Summer 2013. Her research interests include excited state properties of molecules and solids and electronic structure calculations for light absorbers in photoelectrochemical cells.



Dario Rocca

Dario Rocca received a BSc degree in Physics from the University of Pavia, Italy and a PhD in Physics from the International School of Advanced Studies in Trieste, Italy in 2007. He then joined the Chemistry Department of the University of California, Davis as a postdoctoral scholar and he is currently an assistant professor at the University of Lorraine, Nancy, France. His research interests include excited state properties of molecules and solids and electronic structure calculations of nanomaterials.

Desirable methods to study electronic excitations should allow one to tackle condensed and molecular systems on the same footing, and be applicable to broad classes of materials with various compositions. Indeed, depending on the desired design of the photoelectrochemical cell, one may need to describe interfaces between liquid water and a solid surface with a molecular catalyst attached to it, or between water and a complex, possibly disordered and defective solid with a thin film acting as a catalyst deposited on top. In addition, it is necessary to have a general theoretical framework to handle both charged and neutral electronic excitations; the prediction of band edge alignments between photoelectrodes and water, requires the ability to describe charge excitations, that is photoemission and inverse photoemission processes, through which one determines the energy of valence and conduction bands. The optimization of photoelectrodes for light absorption involves instead the description of neutral electron hole pair excitations formed upon the interaction of the material with light, and the description of the subsequent formation of a bound exciton.

Given the breadth of materials which are interesting to explore for photoelectrochemical research, and the complexity of electronic excitations involved, the choice of theoretical methods naturally falls on first principles approaches. First principles (or *ab initio*) calculations do not require any fit to experimental data and are thus not limited to specific classes of systems nor to predetermined morphologies of materials. Density Functional Theory³ (DFT) is one of the most successful *ab initio* theories adopted in the last thirty years by chemists and physicists alike, to compute ground state properties of molecules and solids.⁴ It is in principle an exact theory which however requires approximations for the exchange–correlation potential (V_{xc}) of the electrons in practical calculations

(the exact V_{xc} is unknown). While used mostly by condensed matter physicists until the early 1990s, within the so called local density approximation⁵ (LDA) of V_{xc} , DFT was also adopted by chemists in the last 25 years. The adoption of DFT by the quantum chemistry community came after the development of generalized gradient corrected approximations^{6–8} (GGA) to V_{xc} . Such approximations yield reasonably accurate results for ground state properties of many solids and molecules, unlike the LDA which overall appears to work better for condensed than for molecular phases.

Within DFT, a set of self-consistent independent-electron Schrödinger equations is solved, for a given, approximate V_{xc} , to obtain the density of interacting electrons within a solid or a molecule. These equations are named after Kohn and Sham (KS).⁵ The density uniquely determines all properties of the system. The eigenvalues of the KS equations cannot be interpreted as excitation energies involving addition (electron affinity) or removal (ionization potential) of an electron, except for the highest eigenvalue of a finite system which is minus the ionization energy.^{9,10} Therefore KS eigenvalues should not be used to describe photoemission processes, nor, for example, to compute band offsets and band edges in solids. However, in solids electronic gaps obtained as the difference between the KS energies of the top of the valence band and the bottom of the conduction band, were often compared to experimental data, and likewise the difference between HOMO and LUMO energies in molecules. In many cases it was found that trends within given classes of solids or molecules are well reproduced by KS electronic gaps; however absolute values often show large errors compared to experiments (*e.g.* a factor of approximately two in the case of the band gap of Si). An alternative method to compute excitation energies of molecules and clusters, called the Delta (Δ) self-consistent approach,¹¹ consists in performing DFT ground-state calculations for neutral and charged systems (*i.e.* with an electron either removed or added to the system) and in obtaining the first electron affinity or first ionization potential as differences of total energies. Recently this method was generalized to treat periodic solids.¹²

Furthermore, DFT is not suitable for describing electronic excitations probed by optical absorption experiments. In the simplest linear optical process, an electron undergoes a transition from the ground to an excited state upon interaction with an external electromagnetic field; in a semiconductor or insulator, the excited electron may then bind to the corresponding hole, forming an exciton. In order to describe such an excitation, an extension of DFT to include time dependent perturbations, *i.e.* the electromagnetic field impinging upon a solid or molecule, is required. Such generalization was developed in the 1980s, and goes by the name of time-dependent density functional theory (TDDFT).¹³ The performance of TDDFT in describing absorption processes and exciton binding energies depends again on the choice of the (time dependent) exchange correlation potential. When using adiabatic local or GGA-based approximations, the results of TDDFT for semi-conducting solids and insulators are usually rather poor;¹⁴ they appear to be in better agreement with experiments for several classes of



Giulia Galli

Giulia Galli is Professor of Chemistry and Physics at the University of California, Davis. She holds a PhD in Physics from the International School of Advanced Studies in Trieste, Italy. She is a Fellow of the American Physical Society (APS), and former chair of the Division of Computational Physics of the APS. She is the recipient of a Department of Energy award of excellence in technical computing (2000), and of the Science and

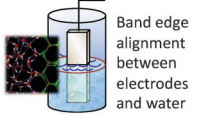
Technology Award from the Lawrence Livermore National Laboratory (2004). She is currently chair of the Extreme Physics and Chemistry of Carbon Directorate of the Deep Carbon Observatory (<https://dco.gl.ciw.edu/>). Her research activity is focused on quantum simulations of systems and processes relevant to condensed matter physics, physical chemistry, and materials science (<http://angstrom.ucdavis.edu/>).

molecules, although notable failures were observed, *e.g.* in the description of charge transfer excitations.^{15,16}

An alternative approach to compute electronic excitations of solids and molecules is based on many body perturbation theory (MBPT) and the Green's function formalism.^{17,18} In the last two decades single-particle Green's functions were widely used in the calculations of photoemission spectra, band offsets and band edges of solids^{19–22} and they are now applied to the calculation of ionization potentials and electron affinities of molecules as well.^{23–26} In a similar fashion, two-particle Green's functions, obtained through approximate solutions of the Bethe–Salpeter equation,^{17,27} (BSE) were employed for the calculation of neutral excitations involved in optical absorption experiments of solids.^{28–31} Recently the BSE was also used to compute optical excitations in molecules and clusters.^{30,32–34} The calculation of Green's functions requires first the determination of the ground state of the electronic system. This may be accomplished in different manners. In most of the condensed matter physics literature, Green's functions are built from single-particle states obtained by solving the KS equations.

Computational difficulties have long limited the application of MBPT to realistic systems of interest for photo-electrochemical energy conversion. However recent algorithmic advances in the computation of quasi-particle energies^{24,25} and in the solution of the BSE^{31,34} are permitting considerable progress in the application of MBPT to photoelectrode materials, including complex semi-conducting oxides. In this review we describe MBPT and Green's function based techniques, for first principle calculations of electronic excitation processes in solids and molecules (see Table 1); we include a discussion of recent algorithms allowing for the application of MBPT to realistic materials. One of our goals is to introduce the formalism of MBPT to the quantum chemistry community and to specify in detail the theoretical and numerical approximations used in *ab initio* calculations, so as to facilitate accurate comparisons with experiments.

Table 1 Electronic excitations discussed in this review (first row), together with experimental (second row) and theoretical (third row) approaches used to probe them. The fundamental equations of the theory described here are given in the fourth row of the table

Processes of interest		
Experiments	Photoemission spectroscopy	UV-vis and ellipsometry spectroscopy
Theory	Single particle Green's functions $G^{(1)}$: poles represent energies to add or remove an electron from a solid or molecule	Two particle correlation function L : poles correspond to neutral excitation energies of interacting electrons
Equations	Dyson's equation: relates $G^{(1)}$ to self energy Σ (effective potential of interacting electrons)	Bethe Salpeter equation: relates L to the variation of Σ with respect to $G^{(1)}$

The rest of the paper is organized as follows: we summarize the general concepts and equations of MBPT in Section 2, and in Section 3 we describe algorithms to solve, in approximate forms, the key equations of MBPT to obtain electronic excitation energies and spectra. We then give some examples of predictions of band alignments and absorption spectra of promising photoelectrode materials in Section 4. We focus on silicon based materials and oxides (TiO_2 and WO_3) for photocathode and photoanode materials, respectively. Finally we give our conclusions and outlook in Section 5.

2 first principles methods to compute photoemission and absorption spectra within many body perturbation theory

2.1 Single-particle Green's functions

In this section we discuss the basic concept of MBPT, that of single-particle many body Green's functions.¹⁸ For the purpose of this review, the term “particle” refers to an electron but the Green's function formalism is not restricted to electrons or fermions (for example, it can be applied to describe phonons). Single-particle Green's functions are useful concepts to compute electronic excitations involving the addition or the removal of an electron and thus to describe photoemission experiments (see Table 1). The time-ordered single-particle Green's function is defined as

$$G^{(1)}(1,2) = -i\langle\Psi_0^N|\hat{T}\hat{\psi}(1)\hat{\psi}^\dagger(2)|\Psi_0^N\rangle, \quad (1)$$

where $1 \equiv (\mathbf{r}_1, t_1)$ and $2 \equiv (\mathbf{r}_2, t_2)$ are compact notations to indicate space coordinates \mathbf{r} and time t (for simplicity the spin variable is not included in our discussion); Ψ_0^N is the normalized many body ground-state wavefunction of a system containing N electrons, \hat{T} is the time-ordering operator, and $\hat{\psi}^\dagger(\mathbf{r}, t)$ ($\hat{\psi}(\mathbf{r}, t)$) is an operator in the Heisenberg representation that creates (destroys) an electron at position \mathbf{r} at time t . In eqn (1) and hereafter, the hat “^” indicates quantum-mechanical operators. Atomic units ($\hbar = m = e = 1$) are used throughout the paper. Symbols frequently used in this review are summarized in Table 2.

In eqn (1) if $t_1 > t_2$ the Green's function $G^{(1)}$ gives the probability amplitude that a particle added to the system at time t_2 in position \mathbf{r}_2 be detected in position \mathbf{r}_1 at time t_1 .

Table 2 Summary of symbols frequently used in this review

$G^{(1)}$	Single-particle Green's function
$G_0^{(1)}$	Non-interacting single-particle Green's function
$G^{(2)}$	Two-particle Green's function
$\hat{\psi}^\dagger$	Creation field operator
$\hat{\psi}$	Annihilation field operator
Ψ_j^N, E_j^N	Wavefunctions and energies of a interacting N electron system; $j = 0$ corresponds to the ground-state
Φ_0^N	Ground state wavefunctions of a non-interacting N electron system
$\varphi_j, e_j^{\text{ind}}$	Independent-electron Hartree orbitals and energies
ϕ_j, e_j^{KS}	Kohn–Sham orbitals and energies
f_j, e_j	Lehmann amplitudes and energies
ϵ	Dielectric matrix

Similarly, if $t_2 > t_1$ a particle is removed from the system and the Green's function describes the time-evolution of the corresponding hole. From the single-particle Green's function it is possible to obtain the expectation value of any single-particle operator (e.g. the density) on the interacting ground-state, and to obtain the ground-state energy by using the Galitskii–Migdal formula.³⁵ The physical interpretation of the Green's function as a propagator of a state with an additional electron or a hole intuitively suggests that Green's function theory may be used to describe experiments that measure electron affinities or ionization potentials.

If the Hamiltonian that describes the time evolution of the field operators $\hat{\psi}(1)$ and $\hat{\psi}^\dagger(2)$ does not explicitly depend on time, the time-ordered Green's function in eqn (1) depends only on the difference ($t_1 - t_2$). In this case, by inserting a complete set of eigenstates of the system $\{\Psi_j^{N+1}\}$ and $\{\Psi_j^{N-1}\}$ with $(N + 1)$ and $(N - 1)$ particles, respectively, in eqn (1), and by applying a Fourier transform (from time t to energy ω), one obtains the so-called Lehmann representation of the Green's function:

$$G^{(1)}(\mathbf{r}_1, \mathbf{r}_2, \omega) = \sum_j \frac{f_j(\mathbf{r}_1) f_j^*(\mathbf{r}_2)}{\omega - \varepsilon_j + i\eta \text{sgn}(\varepsilon_j - \mu)} \quad (2)$$

where η is a positive infinitesimal and sgn denotes the sign function.

$$\left. \begin{aligned} f_j(\mathbf{r}) &= \langle \Psi_0^N | \hat{\psi}(\mathbf{r}) | \Psi_j^{N+1} \rangle \\ \varepsilon_j &= E_j^{N+1} - E_0^N \end{aligned} \right\} \text{ for } \varepsilon_j > \mu, \quad (3)$$

and

$$\left. \begin{aligned} f_j(\mathbf{r}) &= \langle \Psi_j^{N-1} | \hat{\psi}(\mathbf{r}) | \Psi_0^N \rangle \\ \varepsilon_j &= E_0^N - E_j^{N-1} \end{aligned} \right\} \text{ for } \varepsilon_j < \mu. \quad (4)$$

In eqn (3) and (4) μ is the chemical potential, E_0^N is the ground-state energy of the N electrons system and E_j^{N-1} and E_j^{N+1} are the energies of the system in which an electron is removed or added, respectively. Within the Lehmann representation, the poles of the time-ordered single-particle Green's function represent the energies necessary to add or remove an electron. In general the calculation of these energies is far from trivial, since when an electron is added to or removed from the system, all the other electrons readjust in a correlated manner. The Green's function $G^{(1)}$ (eqn (1) and (2)) accounts for all these correlation effects.

2.2 The Dyson's equation

The calculation of the full single-particle Green's function is a difficult task for any system of interacting electrons, in principle as difficult as determining the full many body wavefunction. Perturbation theory may be used to approximate the many body Green's function by considering the Coulomb interaction between electrons, v , as a perturbation acting on the non-interacting system. This approach is called Feynman–Dyson perturbation theory.¹⁸ The perturbation v is adiabatically

“switched on” from $t = -\infty$ (when the perturbation is absent) to $t = 0$, when the interacting Hamiltonian is obtained. The Gell-Mann and Low theorem¹⁸ ensures that the non-interacting ground-state Φ_0^N of the system at $t = -\infty$ (that can be easily computed) evolves, upon adiabatic application of v , to an eigenstate of the fully interacting Hamiltonian. Similarly, the perturbation can be adiabatically “switched off” from $t = 0$ to $t = +\infty$, bringing back the system to the non-interacting ground-state Φ_0^N .

Within this framework the single-particle Green's function is expressed in terms of an expectation value on the non interacting ground-state Φ_0^N . By using Wick's theorem¹⁸ the Green's function can then be expanded in a perturbative series whose terms depend only on the non-interacting single-particle Green's function $G_0^{(1)}$ and the Coulomb interaction v . Feynman diagrams are a convenient way of representing the integrals involved in this perturbative expansion. The analysis of the diagrammatic expansion of the Green's function $G^{(1)}$ leads to the definition of the Dyson's equation^{18,36}

$$G^{(1)}(1, 2) = G_0^{(1)}(1, 2) + \int G_0^{(1)}(1, 3) \Sigma(3, 4) G^{(1)}(4, 2) d(34) \quad (5)$$

where Σ is the self-energy, whose physical meaning will be discussed in detail in the next section. The Dyson's equation is a concise way of expressing the summation over an infinite number of diagrams (within the perturbative expansion).

If an accurate approximation of Σ were known, the Dyson's equation would provide a way to compute the interacting Green's function G from the non-interacting G_0 . The Green's function G_0 can be obtained by setting $\Psi_0^N = \Phi_0^N$ in eqn (1), where Φ_0^N is an independent-particle ground-state wavefunction (it corresponds to a Slater determinant within the first quantization formalism). The non-interacting G_0 can be written explicitly as:

$$\begin{aligned} G_0^{(1)}(1, 2) &= -i \sum_j \varphi_j(\mathbf{r}_1) \varphi_j^*(\mathbf{r}_2) e^{-i\varepsilon_j^{\text{ind}}(t_1 - t_2)} \\ &\times \left[\theta(t_1 - t_2) \theta(\varepsilon_j^{\text{ind}} - \mu) - \theta(t_2 - t_1) \theta(\mu - \varepsilon_j^{\text{ind}}) \right], \end{aligned} \quad (6)$$

where θ is the Heaviside function. The independent single-particle orbitals φ_j and energy levels $\varepsilon_j^{\text{ind}}$ are obtained from the independent electron equation

$$\hat{H}^{\text{ind}} \varphi_j = \left[-\frac{1}{2} \nabla^2 + \hat{V}_{e-I} + \hat{V}_H \right] \varphi_j = \varepsilon_j^{\text{ind}} \varphi_j, \quad (7)$$

where \hat{V}_{e-I} is the Coulomb potential due to the nuclei, \hat{V}_H is the Hartree potential $\int v(\mathbf{r}_1, \mathbf{r}_2) \rho(\mathbf{r}_2) d\mathbf{r}_2$, and ρ is the electron density. By Fourier transforming eqn (6), the Lehmann representation of the independent electron Green's function is obtained:

$$G_0^{(1)}(\mathbf{r}_1, \mathbf{r}_2, \omega) = \sum_j \frac{\varphi_j(\mathbf{r}_1) \varphi_j^*(\mathbf{r}_2)}{\omega - \varepsilon_j^{\text{ind}} + i\eta \text{sgn}(\varepsilon_j^{\text{ind}} - \mu)} \quad (8)$$

where η is a positive infinitesimal introduced to perform the Fourier transform from the time to the frequency domain.

By expressing eqn (8) as $G_0^{(1)} = 1/(\omega - \hat{H}^{\text{ind}})$ and using eqn (2), the Fourier transform of eqn (5) leads to the following eigenvalue equation:

$$\hat{H}^{\text{ind}}(\mathbf{r}_1)f_j(\mathbf{r}_1) + \int \Sigma(\mathbf{r}_1, \mathbf{r}_2, \varepsilon_j)f_j(\mathbf{r}_2)d\mathbf{r}_2 = \varepsilon_j f_j(\mathbf{r}_1) \quad (9)$$

If Σ is known, this equation determines the Lehmann amplitudes and energies defined in eqn (3) and (4).

2.3 The concepts of self-energy and quasi-particle

Eqn (9) is an independent-particle Schrödinger-like equation in which the electrons move in a mean-field determined by the self-energy Σ , which thus plays the role of an effective potential. However, there are a few differences between eqn (9) and a single-particle Schrödinger equation, (e.g. the KS equations of DFT): the self-energy Σ depends on the single-particle energy and is a non-local and non-Hermitian operator. Hence the functions $\{f_j(\mathbf{r})\}$ are not an orthonormal set and the eigenvalues of eqn (9) are not real; therefore it is not straightforward to interpret them in terms of single-particle energies. However, when the imaginary part of ε_j is small (i.e. the lifetime of the state is long), the corresponding spectral peak is narrow and exhibits a strong intensity; in this case ε_j and $f_j(\mathbf{r})$ define a quasi-particle state. The condition of long lifetimes is usually best fulfilled by electronic states near the Fermi energy.³⁷

As already mentioned, the self-energy in eqn (5) and (9) may be approximated through a diagrammatic expansion, within the Feynman–Dyson perturbation theory. The simplest approximation yields the exchange self-energy:¹⁸

$$\Sigma_x(1,2) = iG^{(1)}(1,2)v(1^+,2) \quad (10)$$

Here $v(1,2) \equiv v(\mathbf{r}_1, \mathbf{r}_2)\delta(t_1^+ - t_2)$ and $1^+ \equiv (\mathbf{r}_1, t_1^+) \equiv (\mathbf{r}_1, t_1 + \gamma)$ where γ is a positive infinitesimal. Since Σ_x depends explicitly on the Green's function G , the Dyson's equation and eqn (9) must be solved self-consistently. By performing a Fourier transform from t to ω and computing the corresponding integrals in the frequency domain, eqn (10) becomes:

$$\Sigma_x(\mathbf{r}_1, \mathbf{r}_2) = - \sum_{j=1}^{N_{\text{occ}}} f_j(\mathbf{r}_1)f_j^*(\mathbf{r}_2)v(\mathbf{r}_1 - \mathbf{r}_2) \quad (11)$$

where N_{occ} is the number of occupied states. By using the definition of the exchange self-energy (eqn (11)) in eqn (9), one recovers the Hartree–Fock (HF) equations. Within the HF approximation, the self-energy Σ does not depend on the energy ω , is Hermitian and the self-consistent solution of eqn (9) is straightforward. For practical purposes the HF approximation may be accurate to treat some excitation energies in molecules³⁸ but it is not reliable for solids.^{39,40} In a first quantization framework the HF ground-state wavefunction is a single Slater determinant, namely the electrons are independent particles. In Section 2.6 we will discuss the GW approximation to the self-energy, which introduces correlation effects. We now turn to the definition of the two particle Green's function.

2.4 Two-particle Green's function and the Bethe–Salpeter equation

As mentioned in 2.1, single-particle Green's functions may be used to model photoemission experiments. However, these Green's functions cannot describe the excitations involved in optical absorption experiments. Indeed the simplest linear optical process involves two quasi-particles, an electron and an hole, interacting with each other to form an exciton. The description of such a bound excitation requires a Green's function that represents at the same time the propagation of a hole and of an electron (see Table 1). To describe absorption spectra, we define the two-particle Green's function:¹⁸

$$G^{(2)}(1,2;1',2') = -\langle \Psi_0^N | \hat{T} \hat{\psi}(1)\hat{\psi}(2)\hat{\psi}^\dagger(2')\hat{\psi}^\dagger(1') | \Psi_0^N \rangle. \quad (12)$$

Eqn (12) can be interpreted as a propagator of a state with two additional particles. Depending on the time ordering, these two particles can be two holes, two electrons or an electron-hole pair (i.e. the case of interest to this review). Within this formalism it is convenient to introduce the two-particle correlation function

$$iL(1,2;1',2') = -G^{(2)}(1,2;1',2') + G^{(1)}(1,1')G^{(1)}(2,2') \quad (13)$$

where the product of the single-particle Green's functions $G^{(1)}(1,1')$ and $G^{(1)}(2,2')$ (second term on the right hand side) represents the independent evolution of two quasi-particles. The two-particle correlation function satisfies the following form of the Bethe–Salpeter equation:^{18,41}

$$L(1,2;1',2') = L_0(1,2;1',2') + \int d3456 L_0(1,4;1',3)\Xi(3,5;4,6)L(6,2;5,2') \quad (14)$$

where $iL_0(1,2;1',2') = G^{(1)}(1,2')G^{(1)}(2,1')$; the kernel Ξ is an effective two-particle interaction that can be expressed as the sum of the derivatives of the Hartree potential and of the self-energy (see eqn (5) and (9)) with respect to the single-particle Green's function:

$$\Xi(3,5;4,6) = v(3,6)\delta(3,4)\delta(5,6) + i \frac{\delta\Sigma(3,4)}{\delta G^{(1)}(6,5)}. \quad (15)$$

In order to obtain the two-particle correlation function L from eqn (14), approximations of the single-particle Green's function $G^{(1)}$ and of the kernel Ξ are required. As apparent from eqn (5) and (15), the evaluation of the self-energy Σ is crucial to compute both $G^{(1)}$ and Ξ . If one uses the exchange self-energy (eqn (10)) in eqn (14) and (15), an equation equivalent to the time-dependent Hartree–Fock (TDHF) equation is recovered.⁴²

We note that in eqn (12) the two-particle Green's function contains more information than actually necessary to model any optical absorption experiment and, in general, any neutral excitation involving an electron–hole pair. To model optical absorption, it is sufficient to consider the Green's function¹⁸

$$G^{(2)}(1,2;1,2) = -\langle \Psi_0^N | \hat{T} \hat{\psi}^\dagger(1)\hat{\psi}(1)\hat{\psi}^\dagger(2)\hat{\psi}(2) | \Psi_0^N \rangle, \quad (16)$$

obtained by setting $1' = 1^+$ and $2' = 2^+$ in eqn (12). In eqn (16), $G^{(2)}$ determines the time-evolution of an electron-hole pair, described by the operator $\hat{\psi}^\dagger\hat{\psi}$ (where $\hat{\psi}$ creates a hole and $\hat{\psi}^\dagger$ a particle). Similar to the case of single-particle Green's functions, one may introduce the Lehmann representation for the two-particle correlation function L corresponding to $G^{(2)}$ in eqn (16):

$$L(\mathbf{r}_1, \mathbf{r}_2; \mathbf{r}_1, \mathbf{r}_2, \omega) \equiv L(\mathbf{r}_1, \mathbf{r}_2, \omega) \\ = \sum_{j \neq 0} \left[\frac{\langle \Psi_0^N | \hat{\psi}^\dagger(\mathbf{r}_1) \hat{\psi}(\mathbf{r}_1) | \Psi_j^N \rangle \langle \Psi_j^N | \hat{\psi}^\dagger(\mathbf{r}_2) \hat{\psi}(\mathbf{r}_2) | \Psi_0^N \rangle}{\omega - (E_j^N - E_0^N) + i\eta} \right. \\ \left. \frac{\langle \Psi_0^N | \hat{\psi}^\dagger(\mathbf{r}_2) \hat{\psi}(\mathbf{r}_2) | \Psi_j^N \rangle \langle \Psi_j^N | \hat{\psi}^\dagger(\mathbf{r}_1) \hat{\psi}(\mathbf{r}_1) | \Psi_0^N \rangle}{\omega + (E_j^N - E_0^N) - i\eta} \right] \quad (17)$$

where $\{\Psi_j^N\}$ represents excited state wavefunctions of the system with N electrons and E_j^N the corresponding energies. Since the application of the operator $\hat{\psi}^\dagger(1)\hat{\psi}(1)$ (or $\hat{\psi}^\dagger(2)\hat{\psi}(2)$) to the ground state Ψ_0^N does not change the total number of electrons, only the states Ψ_j^N with N electrons yield non-zero matrix elements in eqn (17). Because of the product $G^{(1)}(1,1')G^{(2)}(2,2')$ entering the definition of L (eqn (13)), the term $j = 0$ does not contribute to the summation in eqn (17).

The physical meaning of L in eqn (17) will be discussed further in the next section; we note here that the poles of L correspond to the neutral excitation energies of the many body system. In Section 3.3 we will show that the calculation of neutral excitations through the solution of the Bethe-Salpeter equation (eqn (14)) can be reformulated in terms of an eigenvalue problem.

2.5 Two-particle correlation functions and linear response theory

Given a many-particle system, one may use linear response theory to study the first order variation of the ground-state expectation value of any physical observable (described by an operator \hat{A}) due to the application of a weak external perturbation $V_{\text{ext}}(\mathbf{r}, t)$. Our interest in linear response theory is twofold: (i) we wish to describe optical absorption experiments, where the electric field of the incident light (the perturbation) is small compared to the internal field of the system (see Section 3.3); (ii) the definition of response functions, such as the dielectric matrix, is necessary to introduce the screened Coulomb interaction and the GW approximation (see Section 2.6). Below we relate the two-particle correlation function introduced in the previous section to the first order response (ρ') of the density of a multi-electron system to an applied perturbation.

Consider the ground-state electronic density $\hat{\rho}$ (namely $\hat{A} = \hat{\rho}$); the first order response to an external perturbation V_{ext} is:

$$\rho'(1) = \int L^R(1, 2) V_{\text{ext}}(2) d(2) \quad (18)$$

Here we use the prime symbol $'$ to indicate a perturbed quantity. The first-order response of any other observable represented by

an operator \hat{B} can be obtained as $\delta\langle B \rangle(t) = \int B(\mathbf{r})\rho'(\mathbf{r}, t)d\mathbf{r}$. In eqn (18) we have introduced the retarded two-particle correlation function L^R , that by definition is the response function of the system. At variance with the time-ordered case, retarded correlation functions fulfill the requirement of causality, which is necessary in linear response theory, where a response is obtained only after a perturbation is applied. However, we note that the use of time-ordered Green's functions is necessary to develop Feynman-Dyson perturbation theory and to derive Hedin's equations discussed in the next section.

In eqn (18) $L^R(1, 2)$ is a particular case of the full (four indexes) retarded correlation function and its Fourier transform to the frequency domain (Lehmann representation) may be easily defined from the time-ordered correlation function of eqn (17):

$$L^R(\mathbf{r}_1, \mathbf{r}_2, \omega) = \text{Re}[L(\mathbf{r}_1, \mathbf{r}_2, \omega)] + i \text{sgn}(\omega) \text{Im}[L(\mathbf{r}_1, \mathbf{r}_2, \omega)], \quad (19)$$

where sgn denotes the sign function. This relation shows how L^R may be obtained from L . Furthermore, for $\omega \geq 0$ L and L^R coincide. Eqn (19) represents the formal link between the two-particle correlation function L defined in Section 2.4 within a Green's function formalism, and linear response theory; in particular, it links L to the first order response of the charge density due to an external perturbation (eqn (18)).

In the following, we introduce the notation used in the literature of many body perturbation theory (MBPT) applied to solids and we relate such notation to that of linear response theory. We define:

$$\chi(1, 2) \equiv L(1, 2) \quad \text{and} \quad \chi_r(1, 2) \equiv L^R(1, 2), \quad (20)$$

where χ is often called time-ordered reducible polarizability and χ_r is the retarded reducible polarizability. For the purpose of this review it is also convenient to define the retarded dielectric matrix ϵ_r and its inverse ϵ_r^{-1} :

$$V'_{\text{scr}}(1) = \int \epsilon_r^{-1}(1, 2) V_{\text{ext}}(2) d(2) \quad (21)$$

Within linear response eqn (21) defines the total screened potential V'_{scr} induced in the system by the external perturbation V_{ext} . By considering $V'_{\text{scr}} = V_{\text{ext}} + V'_H$, where $V'_H = v\chi_r V_{\text{ext}}$ (we have used eqn (18) and the integrals are implicit), we obtain the relation:

$$\epsilon_r^{-1}(1, 2) = \delta(1, 2) + \int v(1, 3)\chi_r(3, 2)d(3). \quad (22)$$

Using the definition of V'_{scr} in eqn (21), one can alternatively define an irreducible polarizability $\tilde{\chi}_r$, which relates the induced density response to the screened potential V'_{scr} :

$$\rho'(1) = \int \tilde{\chi}_r(1, 2) V'_{\text{scr}}(2) d(2). \quad (23)$$

Through eqn (19), the definitions of ϵ_r and relations between ϵ_r , χ_r and $\tilde{\chi}_r$ may be extended to the corresponding time-ordered quantities ϵ , χ and $\tilde{\chi}$. From the next section, we drop the subscript " r " for simplicity.

Table 3 Response functions (first column) used in this review are defined in the second column. The reducible polarizability (χ) is related to the two particle correlation function (L) (see eqn (19) and (20)); the irreducible polarizability ($\tilde{\chi}$) can be expressed by the product of single particle Green's functions (see eqn (32)) within the Random Phase Approximation (RPA); the dielectric matrix (ϵ) defines the screened Coulomb interaction (eqn (24))

Response Function	Definition
Reducible Polarizability χ	Response of the charge density to the external perturbation V_{ext} $\rho' = \chi V_{\text{ext}}$
Irreducible Polarizability $\tilde{\chi}$	Response of the charge density to the screened potential V'_{scr} $\rho' = \tilde{\chi} V'_{\text{scr}}$
Dielectric Matrix ϵ	Relates screened potential V'_{scr} to the external perturbation V_{ext} $V'_{\text{scr}} = \epsilon^{-1} V_{\text{ext}}$

A summary of response functions introduced in this review is given in Table 3. In the next section we use the concept of dielectric matrix to define an effective (screened) Coulomb interaction W , a basic quantity entering the GW approximation.

2.6 Hedin's equations and the GW approximation to the self-energy

In principle, electronic removal and addition energies, necessary to model photoemission measurements, can be computed by solving eqn (9); however, the exact self-energy is unknown. As discussed in Section 2.2, an approximation of Σ may be found by applying Feynman–Dyson perturbation theory to the Coulomb interaction v . In the simplest case this approach leads to the Hartree–Fock approximation, which by definition does not account for any correlation effect. In order to introduce correlation effects, Hedin proposed an approach^{37,43} based on the Schwinger's functional derivative method.^{44,45} Instead of expressing Σ in terms of the bare Coulomb potential v , one expresses the self-energy in terms of the dynamically screened Coulomb potential defined by:

$$W(1,2) = \int \epsilon^{-1}(1,3)v(3,2)d(3). \quad (24)$$

Here ϵ^{-1} is the inverse time-ordered dielectric matrix, which describes the screening of the bare Coulomb potential due to all other electrons in the system. Eqn (24) is a specific case of

eqn (21) in time-ordered form; all the response functions used in this section will be considered in their time-ordered form.

One may view the screened Coulomb potential W as the Coulomb interaction attenuated by ϵ^{-1} ; hence in principle a perturbative expansion of the self-energy in powers of W may be more rapidly convergent than Feynman–Dyson perturbation theory, which is based on the bare v .

Using the polarizabilities defined in Section 2.5, the screened Coulomb potential can be expressed as

$$\begin{aligned} W(1,2) &= v(1,2) + \int v(1,3)\chi(3,4)v(4,2)d(34) \\ &= v(1,2) + \int v(1,3)\tilde{\chi}(3,4)W(4,2)d(34) \end{aligned} \quad (25)$$

Hedin³⁷ introduced a closed set of equations determining Σ and $G^{(1)}$ in terms of W :

$$\Sigma(1,2) = i \int G^{(1)}(1,3)\Gamma(3,2;4)W(4,1)d(34), \quad (26)$$

$$\tilde{\chi}(1,2) = -i \int G^{(1)}(1,3)G^{(1)}(4,1)\Gamma(3,4;2)d(34), \quad (27)$$

$$\begin{aligned} \Gamma(1,2;3) &= \delta(1,2)\delta(1,3) \\ &+ \int \frac{\delta\Sigma(1,2)}{\delta G^{(1)}(4,5)}G^{(1)}(4,6)G^{(1)}(7,5)\Gamma(6,7;3)d(4567) \end{aligned} \quad (28)$$

where $G^{(1)}$ is given by eqn (5) and W by eqn (25). Here $v(1,2) = v(\mathbf{r}_1, \mathbf{r}_2)\delta(t_1 - t_2)$ and $\Gamma(1,2;3)$ is the so-called vertex function. In principle, the set of eqn (5), (25)–(28) must be solved self-consistently to obtain the exact self-energy and the exact many body single-particle Green's function $G^{(1)}$. However, from a computational standpoint the full self-consistent solution of Hedin's equations is a formidable task. Following Hedin,³⁷ by setting the self-energy Σ to 0 in eqn (28), one obtains:

$$\Gamma(1,2;3) = \delta(1,2)\delta(1,3) \quad (29)$$

which provides a first order expansion of Σ in terms of W , through eqn (26) and (27):

$$\Sigma(1,2) = iG^{(1)}(1,2)W(1,2) \quad (30)$$

$$W(1,2) = v(1,2) + \int d(34)v(1,3)\chi_0(3,4)W(4,2) \quad (31)$$

$$\tilde{\chi}(1,2) = \chi_0(1,2) = -iG^{(1)}(1,2)G^{(1)}(2,1). \quad (32)$$

Eqn (32) defines χ_0 which is the random-phase approximation (RPA) to the irreducible polarizability; this approximation treats quasi-particles as independent entities. Eqn (30) defines the GW approximation to the self-energy. By comparison with eqn (10), a formal analogy between the GW and the Hartree–Fock approximation is evident: In the GW approximation instead of the bare Coulomb potential v , used within HF, one uses the dynamically screened Coulomb potential W . Since the self-energy (eqn (30)) depends on the Green's function, eqn (5) or eqn (9) must be solved self-consistently. However, in most

practical implementations the self-consistent procedure is avoided and the GW self-energy is approximated starting from DFT orbitals and energies (see Sections 3.2.1 and 3.2.2).

By performing a Fourier transform, eqn (30) can be expressed as a convolution:

$$\Sigma(\mathbf{r}_1, \mathbf{r}_2, \omega) = \frac{i}{2\pi} \int e^{i\omega'\eta} G^{(1)}(\mathbf{r}_1, \mathbf{r}_2, \omega + \omega') W(\mathbf{r}_1, \mathbf{r}_2, \omega') d\omega'; \quad (33)$$

where η is an infinitesimal. This expression is often used in numerical calculations, and its evaluation is a challenging task. To simplify such a task, Hedin introduced the Coulomb-hole plus screened exchange (COHSEX) approximation to the GW self-energy:⁴³

$$\begin{aligned} \Sigma_{\text{COHSEX}}(\mathbf{r}_1, \mathbf{r}_2) &= \Sigma_{\text{COH}}(\mathbf{r}_1, \mathbf{r}_2) + \Sigma_{\text{SEX}}(\mathbf{r}_1, \mathbf{r}_2) \\ &= \frac{1}{2} \delta(\mathbf{r}_1, \mathbf{r}_2) W_p(\mathbf{r}_1, \mathbf{r}_2, 0) \\ &\quad - \sum_{j=1}^{N_{\text{occ}}} f_j(\mathbf{r}_1) f_j^*(\mathbf{r}_2) W(\mathbf{r}_1, \mathbf{r}_2, 0), \end{aligned} \quad (34)$$

where $W_p = W - v$ and W is the statically screened Coulomb interaction. The term Σ_{COH} describes the interaction of a quasi-particle with the potential induced by the quasi-particle itself. The term Σ_{SEX} represents a statically screened Hartree-Fock exchange operator (see eqn (11)). The COHSEX self-energy presents several practical advantages over the full GW self-energy (eqn (33)). The operator Σ_{COHSEX} is Hermitian, static, (*i.e.* it does not depend on ω) and requires only a summation up to N_{occ} (the number of occupied electronic states); instead the use of the GW approximation (see the definition of the Green's function $G^{(1)}$ in eqn (2)), requires a summation over all the states (occupied and empty). However, the COHSEX approximation is known to overestimate the electronic gaps of several materials,¹⁹ despite some recent improvements.⁴⁶ We note that in most computational applications,^{29,30,47} a static approximation to the self-energy is used to represent the kernel of the Bethe-Salpeter equation (see eqn (15)), as discussed in Section 3.

As mentioned in Section 1, in first principles calculations the KS energy levels and orbitals are often used to build approximations to the Green's functions and response functions and hence to W . The screened Coulomb potential W is a fundamental ingredient both for the solution of the Dyson's equation in the GW approximation, and for the solution of the Bethe-Salpeter equation. Therefore in the next section we describe in detail how W is evaluated in practical calculations starting from KS orbitals (see Table 4 for a summary).

2.7 Dielectric matrices and polarizabilities

The key quantity entering the definition of the screened Coulomb potential (eqn (24)) is the dielectric matrix ϵ . The main purpose of this section is to discuss how ϵ is approximated in first principles calculations based on MBPT. These approximations will then be used in Section 3, where we describe practical implementations of the GW approximation and the Bethe-Salpeter equation. We first

Table 4 Theoretical approximations (second row) and algorithmic challenges (fourth row) involved in the calculation of photoemission and absorption spectra. Quasiparticle energies and absorption spectra are defined in the third row of the table

Physical observables	Photoemission spectra	Absorption spectra
Theoretical Approximation	GW approximation: 1 st order, perturbative expansion of the self energy Σ in terms of the screened Coulomb interaction W : $\Sigma \approx iGW$; $W = \epsilon^{-1}v$	Solution of the BSE: approximate self-energy (e.g. using GW) in two particle Hamiltonian (\mathcal{L}), defined within 1 st order perturbation theory
Practical calculations	Ground state single particle orbitals from KS equations; Quasi-particle energy corrections to KS eigenvalues from the expectation value of Σ on KS orbitals	Frequency dependent polarizability (molecules) or macroscopic dielectric function (solids) from iterative diagonalization of two-particle Hamiltonian
Algorithmic Challenges	Evaluate sums on virtual states for G and W ; Frequency dependence and inversion of ϵ	Evaluate sums on virtual states for \mathcal{L} and W , and inversion of ϵ

discuss the calculation of the static ϵ ($\omega = 0$) and later we will illustrate practical approaches adopted to introduce dynamical effects. The response functions discussed here are retarded response functions (see Section 2.5); however, in order to simplify the notation the subscript “*r*” is not included. We emphasize again that in the static limit ($\omega = 0$) there is no difference between time-ordered and retarded Green's functions.

In most first principles MBPT calculations the dielectric matrix ϵ is computed using KS single-particle orbitals and energies.^{19,29,47–49} Hence before discussing ϵ , we summarize the definition of polarizabilities within DFT. The Kohn-Sham equations of DFT have the following form:⁵

$$\left[-\frac{1}{2}\nabla^2 + V_{\text{KS}}(\mathbf{r}) \right] \phi_j(\mathbf{r}) = \epsilon_j^{\text{KS}} \phi_j(\mathbf{r}). \quad (35)$$

where ϕ_j and ϵ_j^{KS} are KS orbitals and KS single particle energies, respectively, and we have defined the KS effective potential:

$$\begin{aligned} V_{\text{KS}}(\mathbf{r}) &= V_{\text{H}}(\mathbf{r}) + V_{\text{xc}}(\mathbf{r}) + V_{e-I}(\mathbf{r}) \\ &= \int \frac{\rho(\mathbf{r}')}{|\mathbf{r} - \mathbf{r}'|} d\mathbf{r}' + \frac{\delta E_{\text{xc}}[n]}{\delta n(\mathbf{r})} + V_{e-I}(\mathbf{r}). \end{aligned} \quad (36)$$

In eqn (36) $\rho(\mathbf{r})$ is the electronic density, V_{H} is the Hartree potential, V_{xc} is the functional derivative with respect to the density of the exchange-correlation (xc) energy functional E_{xc} , and V_{e-I} is the external Coulomb potential due to the atomic nuclei. If the exact V_{xc} were known, the self-consistent solution of eqn (36) would give the exact density of the many-electron system. The density is expressed as:

$$\rho(\mathbf{r}) = \sum_{j=1}^{N_{\text{occ}}} \phi_j^*(\mathbf{r}) \phi_j(\mathbf{r}), \quad (37)$$

where the sum is over the number of occupied orbitals N_{occ} . In practice, approximations are used for E_{xc} . Even simple approximations, such as the local density approximation (LDA), may lead to accurate results for several ground state properties of realistic materials.⁴

As a consequence of fundamental theorems³ of DFT, the response of the KS density to a static perturbation V_{ext} is the same as that of the full many body system. The response of the electronic density can be written as

$$\rho'(\mathbf{r}) = \int \chi_0(\mathbf{r}, \mathbf{r}') V'_{\text{KS}}(\mathbf{r}') d\mathbf{r}', \quad (38)$$

where

$$V'_{\text{KS}}(\mathbf{r}) = V_{\text{ext}}(\mathbf{r}) + V'_{\text{H}}(\mathbf{r}) + V'_{\text{xc}}(\mathbf{r}), \quad (39)$$

and we assumed that the position of atomic nuclei is not modified by the application of the perturbation ($V'_{e-I} = 0$); χ_0 is the static RPA irreducible polarizability, which has the following explicit form:

$$\chi_0(\mathbf{r}, \mathbf{r}') = \sum_{jk} (n_k - n_j) \frac{\phi_k^*(\mathbf{r}) \phi_j(\mathbf{r}) \phi_j^*(\mathbf{r}') \phi_k(\mathbf{r}')}{\epsilon_k^{\text{KS}} - \epsilon_j^{\text{KS}} + i\eta}. \quad (40)$$

Here ϕ_j and ϕ_k are KS orbitals and ϵ_j^{KS} and ϵ_k^{KS} are KS energies (see eqn (35)); n_j and n_k are the occupation numbers of the states j and k , respectively. If j and k are both occupied or both empty states, their contribution to χ_0 vanishes. Note that in the static limit ($\omega = 0$) and within an approximation of $G^{(1)}$ based on DFT (*i.e.* when approximating the Lehmann amplitudes and energies of eqn (2) by ϕ_j and ϵ_j^{KS} , respectively), eqn (32) and (40) are equivalent. In eqn (39) we have introduced the first-order response of the Hartree and xc potential induced by the application of V_{ext} :

$$\begin{aligned} V'_{\text{Hxc}}(\mathbf{r}) &= V'_{\text{H}}(\mathbf{r}) + V'_{\text{xc}}(\mathbf{r}) \\ &= \int v(\mathbf{r}, \mathbf{r}') \rho'(\mathbf{r}') d\mathbf{r}' + \int K^{\text{xc}}(\mathbf{r}, \mathbf{r}') \rho'(\mathbf{r}') d\mathbf{r}' \end{aligned} \quad (41)$$

where $K^{\text{xc}} = \delta V_{\text{xc}} / \delta \rho$ is the functional derivative of the xc potential with respect to the density, evaluated at the ground-state density. By comparing the density response expressed by eqn (38) to the definition of eqn (18) (with $\omega = 0$, and using $\chi = L^{\text{R}}$), we obtain the following relation, by means of eqn (41):

$$\chi = \chi_0 + \chi_0(v + K^{\text{xc}})\chi. \quad (42)$$

Here the coordinate dependence and the integrals over space coordinates are implicit. The term $(v + K^{\text{xc}})$ describes correlation effects, absent in the non-interacting KS polarizability χ_0 . Indeed, by setting $(v + K^{\text{xc}})$ to zero, in eqn (42) we obtain $\chi = \chi_0$. Eqn (42) may be used to express χ in terms of χ_0 :

$$\chi = (1 - \chi_0 v - \chi_0 K^{\text{xc}})^{-1} \chi_0. \quad (43)$$

Having derived an explicit expression for χ , we finally determine the inverse dielectric matrix entering eqn (21) and defining the screened Coulomb interaction. By interpreting the KS response potential V'_{KS} in eqn (39) as the effective potential V'_{scr} acting on the electrons, we can easily derive the result

$$\epsilon^{-1} = 1 + (v + K^{\text{xc}})\chi; \quad (44)$$

this expression of ϵ is obtained for the case in which the electrons themselves are the probe of the system response.⁵⁰ In most practical implementations of first principles many

body perturbation theory the random-phase approximation (RPA) is used for ϵ^{-1} instead of the full DFT expression of eqn (42). The RPA consists in discarding the term K^{xc} in eqn (42) and leads to the following expression of ϵ^{-1} :

$$\epsilon_{\text{RPA}}^{-1} = 1 + v\chi = 1 + v(1 - \chi_0 v)^{-1} \chi_0 \quad (45)$$

that can also be written in the more common form:

$$\epsilon_{\text{RPA}} = 1 - v\chi_0. \quad (46)$$

In several first principles MBPT calculations the frequency dependence of ϵ is described by using models, such as the plasmon-pole model,^{21,51} which will be discussed in detail in Section 3.1.1. Alternatively, by defining the RPA independent electron dynamical polarizability

$$\chi_0(\mathbf{r}, \mathbf{r}', \omega) = \sum_{jk} (n_k - n_j) \frac{\phi_k^*(\mathbf{r}) \phi_j(\mathbf{r}) \phi_j^*(\mathbf{r}') \phi_k(\mathbf{r}')}{\omega + (\epsilon_k^{\text{KS}} - \epsilon_j^{\text{KS}}) + i\eta}, \quad (47)$$

an equation formally identical to eqn (42) may be derived for the frequency dependent χ . However, in this case the derivation must be carried out within the time-dependent density functional theory framework, and the kernel K^{xc} depends explicitly¹³ on the energy ω . For practical purposes the adiabatic approximation $K^{\text{xc}} \approx K^{\text{xc}}(\omega = 0)$ is adopted in most cases.⁵² The definition of the RPA dielectric matrix given in eqn (45) and (46) is valid also in the dynamical case. The solution of eqn (42) or the analogous RPA equation ($K^{\text{xc}} = 0$) could be used to describe the optical spectra at the TDDFT and DFT-RPA levels of theory.

3 Algorithms to compute quasi-particle energies and optical spectra

Having established the theoretical framework of MBPT, we discuss below the main algorithms used in first principles calculations to compute photoemission and absorption spectra (see Table 4). Our discussion is split into three parts and includes algorithms to compute the dielectric matrix, the self-energy, and to solve approximate forms of the BSE.

3.1 Algorithms to compute dielectric matrices

The algorithms discussed in this section are divided into methods where explicit summations on empty states are performed (Section 3.1.1) and methods that avoid these explicit summations (Section 3.1.2) by using, *e.g.* density functional perturbation theory.

3.1.1 Direct calculation of dielectric matrices. Most calculations of dielectric matrices are based on a plane wave (PW) representation^{21,50,53,54} of the orbitals and density, although calculations using localized orbitals have been proposed in the literature.^{55–57} With PW basis sets, both periodic systems and molecules can be treated in a straightforward way, by using a supercell approach. Here we discuss practical calculations of dielectric matrices using a plane-wave basis set for the KS orbitals and charge density. However, our discussion is general and valid irrespective of the basis set chosen.

Within a plane-wave representation,

$$\epsilon^{-1}(\mathbf{r}, \mathbf{r}') = \frac{1}{\Omega} \sum_{\mathbf{q}, \mathbf{G}, \mathbf{G}'} e^{i(\mathbf{q}+\mathbf{G})\cdot\mathbf{r}} \epsilon_{\mathbf{G}, \mathbf{G}'}^{-1}(\mathbf{q}) e^{-i(\mathbf{q}+\mathbf{G}')\cdot\mathbf{r}'}, \quad (48)$$

where Ω denotes the crystal volume, \mathbf{q} is the transferred momentum and \mathbf{G} and \mathbf{G}' are the reciprocal lattice vectors. The limit $q \rightarrow 0$ is well defined, as discussed in ref. 50 and 54, but for $G' = G = 0$ the calculation of ϵ^{-1} requires a special treatment. For a homogeneous system, ϵ depends only on $|\mathbf{r} - \mathbf{r}'|$ and is diagonal in reciprocal space ($\epsilon(\mathbf{G}, \mathbf{G}') = 0$ for $\mathbf{G} \neq \mathbf{G}'$). For an inhomogeneous system, the off-diagonal elements $\epsilon(\mathbf{G}, \mathbf{G}')$ yield the so called local field effects.

The first step to compute $\epsilon_{\mathbf{G}, \mathbf{G}'}^{-1}$ is the evaluation of the irreducible polarizability χ_0 (eqn (40)):

$$(\chi_0)_{\mathbf{G}, \mathbf{G}'}(\mathbf{q}) = \frac{4}{\Omega} \sum_{\mathbf{c}, \mathbf{v}, \mathbf{k}} \frac{\langle \phi_{\mathbf{v}\mathbf{k}} | e^{-i(\mathbf{q}+\mathbf{G})\cdot\mathbf{r}} | \phi_{\mathbf{c}\mathbf{k}+\mathbf{q}} \rangle \langle \phi_{\mathbf{c}\mathbf{k}+\mathbf{q}} | e^{i(\mathbf{q}+\mathbf{G}')\cdot\mathbf{r}'} | \phi_{\mathbf{v}\mathbf{k}} \rangle}{\epsilon_{\mathbf{v}\mathbf{k}}^{\text{KS}} - \epsilon_{\mathbf{c}\mathbf{k}+\mathbf{q}}^{\text{KS}}} \quad (49)$$

where a factor 2 has been introduced to account for spin degeneracy and the indexes \mathbf{v} and \mathbf{c} label valence and conduction states, respectively, in the case of a solid. (In the case of molecules, \mathbf{v} and \mathbf{c} represent occupied and virtual states, respectively). Eqn (49) is the Adler–Wiser formulation^{58,59} of χ_0 . The evaluation of χ_0 using eqn (49) requires the explicit calculation of the conduction states $\phi_{\mathbf{c}}$. In principle all the empty states of the KS Hamiltonian should be included in the summation. In practical calculations only a finite number of them is included and the convergence of the sum is systematically tested. In addition, the expression of eqn (49) requires the evaluation of all possible combinations of \mathbf{c} , \mathbf{v} , \mathbf{k} , and \mathbf{q} . The calculation of the integrals $\int \phi_{\mathbf{v}\mathbf{k}}^*(\mathbf{r}) e^{-i(\mathbf{q}+\mathbf{G})\cdot\mathbf{r}} \phi_{\mathbf{c}\mathbf{k}+\mathbf{q}}(\mathbf{r}) d\mathbf{r}$ scales as $N_{\text{pw}}^2 \times N_{\mathbf{c}} \times N_{\mathbf{v}} \times N_{\mathbf{k}} \times N_{\mathbf{q}}$ where here N_{pw} is the number of basis functions (plane-waves) used to represent the charge density; $N_{\mathbf{c}}$ and $N_{\mathbf{v}}$ is the number of conduction and valence states, respectively and $N_{\mathbf{k}}$ and $N_{\mathbf{q}}$ are the number of \mathbf{k} and \mathbf{q} points (defined as the difference between \mathbf{k} points) included in the BZ summation. (For calculations of molecules and clusters one uses only the $\mathbf{k} = (0,0,0)$ point and $N_{\mathbf{k}} = N_{\mathbf{q}} = 1$). Once χ_0 is obtained, ϵ^{-1} is computed through eqn (45), which requires the inversion of the matrix $(1 - \chi_0 \nu)$ and a subsequent matrix multiplication. The number of reciprocal \mathbf{G} vectors (that determines the dimension of χ_0) used in first principles calculations is often large (many thousands) even for systems with a relatively small number of electrons, and the direct inversion of ϵ becomes very demanding. If the dielectric matrix is computed for multiple frequencies, the inversion must be repeated for each frequency.

For example, in the calculation of quasi-particle energies within the GW approximation, dynamical effects are included in the screened Coulomb potential by evaluating the inverse dynamical dielectric matrix $\epsilon^{-1}(\omega)$, which thus needs to be inverted for each ω . Furthermore ϵ^{-1} has poles on the real ω axis. To overcome these difficulties several numerical

implementations use a plasmon-pole model (PPM), where the dependence of ϵ^{-1} on ω is described by a single plasmon-pole:

$$\epsilon_{\mathbf{G}, \mathbf{G}'}^{-1}(\mathbf{q}, \omega) \approx \delta_{\mathbf{G}\mathbf{G}'} + \frac{R_{\mathbf{G}\mathbf{G}'}(\mathbf{q})}{\omega - \tilde{\omega}_{\mathbf{G}\mathbf{G}'}(\mathbf{q}) + i\eta} - \frac{R_{\mathbf{G}\mathbf{G}'}(\mathbf{q})}{\omega + \tilde{\omega}_{\mathbf{G}\mathbf{G}'}(\mathbf{q}) - i\eta}, \quad (50)$$

where $R_{\mathbf{G}\mathbf{G}'}$ and $\tilde{\omega}_{\mathbf{G}\mathbf{G}'}$ are parameters to be determined for each specific system. Once eqn (45) is solved, the value of $\epsilon_{\mathbf{G}, \mathbf{G}'}^{-1}(\mathbf{q}, \omega = 0)$ can be used to fix one of the two parameters in eqn (50) (this operation is required for each value of $\mathbf{G}\mathbf{G}'$, and \mathbf{q}). In the plasmon-pole approximation proposed by Hybertsen and Louie²¹ the f-sum rule is used as a constraint for the determination of the remaining parameter. In the approach proposed by Godby and Needs⁵¹ the remaining parameter is determined by computing ϵ^{-1} for an additional imaginary frequency ($i\omega$). The PPM approach considerably simplifies the numerical workload necessary to include dynamical effects in quasi-particle calculations. However, the accuracy of the PPM to compute GW quasi-particle energies is difficult to assess, and the results may considerably depend on the choice of the specific model.^{22,60}

Alternatively, one may solve eqn (45) starting from the dynamical polarizability χ_0 defined in eqn (47). Since χ_0 and the inverse dielectric matrix ϵ^{-1} have poles on the real axis, they are usually computed on the imaginary axis ($\omega \rightarrow i\omega$).^{20,48} On the imaginary axis ϵ^{-1} is a smooth function of ω and the integrals necessary to evaluate the self-energy Σ are easier to compute. The expectation value of the self-energy on the imaginary axis is then fitted to a multipole function, which is used to evaluate the final result for real energies.

3.1.2 Projective dielectric eigenpotential method. Recently an alternative approach was introduced for the calculation^{61,62} of the dielectric matrix ϵ called projective dielectric eigenpotential method (PDEP). Applied so far within the RPA approximation, this approach is based on the iterative diagonalization of the dielectric matrix and is of general validity beyond the RPA. At each iterative step, the dielectric matrix is applied to an approximate set of eigenvectors using density-functional perturbation theory (DFPT).⁵⁴ The method was first used to compute ϵ for the evaluation of ground-state correlation energies,^{63,64} and more recently it was incorporated in many body perturbation theory calculations.^{24,31,34}

The dielectric matrix ϵ is not Hermitian and it is convenient to introduce the following symmetrized form:

$$\bar{\epsilon}_{\mathbf{G}, \mathbf{G}'}(\mathbf{q}) = \frac{|\mathbf{q} + \mathbf{G}|}{|\mathbf{q} + \mathbf{G}'|} \epsilon_{\mathbf{G}, \mathbf{G}'}(\mathbf{q}). \quad (51)$$

The matrix $\bar{\epsilon}$ is easier to handle from a numerical point of view, since iterative algorithms to diagonalize Hermitian matrices, such as the Davidson algorithm,⁶⁵ are in general more stable and efficient than those used for non-Hermitian matrices. Within PDEP one considers a spectral decomposition of $\bar{\epsilon}$:

$$\bar{\epsilon} = \sum_{i=1}^{N_{\text{eig}}} \lambda_i |U_i\rangle \langle U_i| = \sum_{i=1}^{N_{\text{eig}}} (\lambda_i - 1) |U_i\rangle \langle U_i| + I. \quad (52)$$

where the eigenvectors (or eigenpotentials) U_i and eigenvalues λ_i are obtained iteratively.

A number N_{eig} of random trial potentials U_i^0 is first generated and then orthonormalized. Starting from this guess, an iterative algorithm, such as Davidson⁶⁵ or Ritz acceleration, is used to diagonalize $\bar{\epsilon}$. At each iteration (iter) the dielectric matrix is applied to the current approximation of the eigenpotentials U_i^{iter} : $(\bar{\epsilon} - I)U_i^{\text{iter}} = -v^{\frac{1}{2}}\chi_0 v^{\frac{1}{2}}U_i^{\text{iter}} = -v^{\frac{1}{2}}\rho'$, where ρ' is determined from:

$$\rho'(\mathbf{r}) = 4\text{Re} \sum_{j=1}^{N_{\text{occ}}} \phi_j^*(\mathbf{r})\phi_j'(\mathbf{r}), \quad (53)$$

and

$$(\hat{H}_{\text{KS}} - \epsilon_j^{\text{KS}})|\phi_j'\rangle = -\hat{Q}V'_{\text{KS}}|\phi_j\rangle \quad (54)$$

by setting $V'_{\text{KS}} = v^{\frac{1}{2}}U_i^{\text{iter}}$. In eqn (53) and (54) \hat{Q} is the projector onto the virtual state subspace, V'_{KS} is defined in eqn (39), and ϕ_j' represents the linear response of KS orbitals. Once the required accuracy in the diagonalization is reached, the iterative procedure is stopped.

The eigenvalue decomposition of eqn (52) is useful for practical purposes only if the number of eigenpotentials N_{eig} necessary to approximate $\bar{\epsilon}$ is much smaller than the dimension of the full matrix.⁶⁶ The eigenvalues λ_i are larger than or equal to 1 and for many systems^{61,62} they rapidly decay to 1 as a function of the index i . This finding implies that $(\lambda_i - 1)$ rapidly goes to 0 as a function of i and the summation in eqn (52) can be truncated to a small number N_{eig} . Recent GW and BSE calculations^{24,31,34} demonstrated that the number N_{eig} is indeed much smaller than the size of the full matrix $\bar{\epsilon}$ for several classes of systems.

The use of eqn (52) to represent the dielectric matrix has several advantages: a small number of eigenpotentials needs to be stored in memory instead of the full matrix $\bar{\epsilon}$; the size of $\bar{\epsilon}$ as function of the number of PWs does not need to be truncated, and the inversion of the dielectric matrix is avoided. Furthermore, the eigenvalue decomposition of $\bar{\epsilon}$ is obtained within DFPT and does not require the explicit inclusion of virtual (empty) states in any summation: all the virtual states described by the chosen basis set are automatically included.

The PDEP procedure may also be applied to compute the frequency dependent dielectric function. In the case of imaginary frequencies, the operator on the left hand side of eqn (54) is $(\hat{H}_{\text{KS}} - \epsilon_j^{\text{KS}} - i\omega)$. The corresponding linear problem is no longer Hermitian and can be solved by a biconjugate gradient algorithm. The eigenvalue decomposition is carried out⁶³ for each value of ω .

An alternative, more efficient approach consists in using the eigenpotentials $\{U_j\}$ at $\omega = 0$ as a basis set for $\bar{\chi}_0(i\omega) = v^{\frac{1}{2}}\chi_0(i\omega)v^{\frac{1}{2}}$; the definition of $\bar{\chi}_0$ is computationally more convenient than that of χ_0 , and it is similar to the definition of $\bar{\epsilon}$.

The expansion coefficients $\bar{\chi}_0^{ij}(i\omega) = \int U_i(\mathbf{r})\bar{\chi}_0(\mathbf{r}, \mathbf{r}'; i\omega)U_j(\mathbf{r}')d\mathbf{r}d\mathbf{r}'$ are expressed in the form:²⁴

$$\bar{\chi}_0^{ij}(i\omega) = 2 \sum_{k=1}^{N_{\text{occ}}} \left\{ \left\langle \phi_k(v^{\frac{1}{2}}U_i) \left| \hat{Q}(\hat{H}_{\text{KS}} - \epsilon_k^{\text{KS}} - i\omega)^{-1} \hat{Q} \right| \phi_k(v^{\frac{1}{2}}U_j) \right\rangle + c.c. \right\} \quad (55)$$

and they can be efficiently computed by using the Lanczos algorithm.⁶⁷ By introducing $\bar{\chi}(i\omega) = v^{\frac{1}{2}}\chi(i\omega)v^{\frac{1}{2}}$ from eqn (42) in the RPA approximation ($K^{\text{xc}} = 0$) we have $\bar{\chi} = (1 - \bar{\chi}_0)^{-1}\bar{\chi}_0$. This equation can be easily solved to compute $\bar{\chi}$ and the reducible polarizability, and the basis set $\{U_j\}$ is usually much smaller than that used for the wavefunctions and density.

3.2 Algorithms to compute the self-energy

Similar to the previous section we first discuss methods where explicit summations on empty states are performed (Section 3.2.1) and then methods that avoid these summations (Section 3.2.2). Recent developments beyond the G_0W_0 approximation are presented in Section 3.2.3.

3.2.1 G_0W_0 calculations based on direct summations.

Calculations of quasi-particle energies of realistic systems within the GW approximation have been performed both in the time domain (eqn (30))⁶⁸ and in the frequency domain (eqn (33)).^{20,21} In particular, the time domain approach⁶⁸ takes advantage of the simple multiplicative form of the self-energy (eqn (30)) and of the polarizability in eqn (32), within a real space and (imaginary) time representation. However, it includes FFT transforms of ϵ from imaginary frequencies and reciprocal space to real time and space, and summations over empty states are not avoidable in any straightforward way.

The solution of eqn (9) with the self-energy approximated at the GW level of theory (eqn (33)) is numerically challenging for several reasons: the GW self-energy depends on the solution of the Dyson's equation, and explicitly on the energy; in addition, it is non-local in space. Most of practical implementations are based on the G_0W_0 approach.^{19,21} Within this scheme the Green's function (eqn (2)) is evaluated by approximating the quasi-particle amplitudes with KS orbitals and the quasi-particle energies with KS energy levels:

$$G^{(1)}(\mathbf{r}_1, \mathbf{r}_2, \omega) \approx \sum_j \frac{\phi_j(\mathbf{r}_1)\phi_j^*(\mathbf{r}_2)}{\omega - \epsilon_j^{\text{KS}} + i\eta \text{sgn}(\epsilon_j^{\text{KS}} - \epsilon_F)}. \quad (56)$$

The screened Coulomb potential is approximated by using the inverse dielectric matrix in eqn (45); when using the KS orbitals to evaluate the screened Coulomb potential, one uses the notation W_0 instead of W . The effects of the dynamical screening are often introduced by a plasmon-pole model (eqn (50)) or by evaluating ϵ on the imaginary axis. The quasi-particle energies are then computed as corrections to KS eigenvalues by using first order perturbation theory:

$$\epsilon_j^{\text{GW}} = \epsilon_j^{\text{KS}} + \langle \phi_j | \Sigma(\epsilon_j^{\text{GW}}) - V_{\text{xc}} | \phi_j \rangle \quad (57)$$

Eqn (57) must be solved self-consistently in ϵ_j^{GW} ; alternatively, using a Taylor expansion one has $\epsilon_j^{\text{GW}} \approx \epsilon_j^{\text{KS}} + Z_j \langle \phi_j | \Sigma(\epsilon_j^{\text{KS}}) - V_{\text{xc}} | \phi_j \rangle$ with $Z_j = \left[1 - \langle \phi_j | \partial \Sigma / \partial \epsilon |_{\epsilon = \epsilon_j^{\text{KS}}} | \phi_j \rangle \right]^{-1}$.

The G_0W_0 approximation implicitly assumes that KS orbitals are a reasonably accurate representation of quasi-particle wavefunctions. In principle there is no sound theoretical justification for this assumption. In practice the G_0W_0 approximation has been shown to work reasonably well for a variety of periodic solids.^{19–21} For molecules the use of this approximation is more controversial⁶⁹ but overall it has given accurate results for the ionization potentials of several systems.^{24–26}

For computational convenience, one normally writes $iGW = iGv + iGv\chi v \equiv \Sigma_x + \Sigma_c$, where the term iGv is the Hartree–Fock self-energy Σ_x (eqn (10)). The evaluation of the expectation value of Σ_x is equivalent to evaluating the exchange term in the Hartree–Fock theory but using DFT orbitals instead of self-consistent HF orbitals. In quantum chemistry codes, this operation is efficiently performed with localized basis, but it is not straightforward in a plane wave representation; in particular care must be exercised to integrate divergences.^{63,70} The most expensive component of G_0W_0 calculations is the evaluation of Σ_c , which requires summations over virtual states of the KS Hamiltonian. These sums are necessary to evaluate both eqn (56) and (40) (or equivalently eqn (49)). In particular it has been shown that the convergence of G_0W_0 can be extremely slow both for some bulk materials, e.g. ZnO^{60,71} and molecular systems, e.g. benzene.²⁵

Unless a PPM is used, the sum over states in the screened Coulomb potential must be evaluated for each value of ω' ; in the case of $G^{(1)}$ it must be evaluated for each value of $(\omega + \omega')$ (namely on a mesh twice as large as that of the ω domain). The convolution in eqn (33) can then be computed through a direct integration or a Fourier transform.

3.2.2 G_0W_0 calculations based on the spectral decomposition of the dielectric matrix. To avoid the explicit summations over a large number of virtual states required for the calculation of the GW self-energy Σ_c , one may use the PDEP technique. We rewrite eqn (56) as:

$$G^{(1)}(i\omega) \approx \frac{1}{\hat{H}_{\text{KS}} - i\omega}. \quad (58)$$

We then use the definition of the GW self-energy in the frequency domain (eqn (33)) and the expansion of the dielectric matrix in terms of the static eigenpotentials (see Section 3.1.2); we arrive at the following expression for the expectation value of Σ_c for imaginary frequencies:

$$\begin{aligned} & \langle \phi_k | \Sigma_c(i\omega) | \phi_k \rangle \\ &= \frac{i}{2\pi} \sum_{i,j=1}^{N_{\text{eig}}} \int d\omega' \bar{\chi}_{ij}(i\omega') \left\langle \phi_k \left(v \frac{1}{2} U_i \right) \left[\hat{H}_{\text{KS}} - i(\omega + \omega') \right]^{-1} \left| \phi_k \left(v \frac{1}{2} U_j \right) \right\rangle \right\rangle; \end{aligned} \quad (59)$$

the coefficients $\bar{\chi}_{ij}$ are computed from eqn (55) by using the definition $\bar{\chi} = (1 - \bar{\chi}_0)^{-1} \bar{\chi}_0$. In eqn (59) the matrix element can be computed with the Lanczos algorithm proposed in ref. 26 and 27. Such algorithm has the advantage that only a single iterative

Lanczos chain is performed for all the frequencies $(\omega + \omega')$. Within this approach all summations over the virtual states are avoided, and all the virtual states described by the chosen basis set are implicitly included. In addition the convergence of the calculation is controlled by a single parameter: N_{eig} (eqn (52)).

The computational workload^{61–63} to generate the dielectric matrix with N_{eig} eigenvectors scales as $N_{\text{iter}} \times N_{\text{eig}} \times N_{\text{pw}} \times N_{\text{v}}^2$, with N_{iter} being the number of iterations needed to converge the dielectric eigenvectors in the iterative diagonalization procedure (N_{iter} is typically not more than 10 for systems with tens to several hundred electrons). In addition, the cost of Lanczos chains generation to compute $\bar{\chi}_0$ and Σ_c is $N_{\text{Lanczos}} \times N_{\text{eig}} \times N_{\text{pw}} \times N_{\text{v}}^2$ where N_{Lanczos} is the number of Lanczos iterations, which is typically just a few tens. Therefore the total workload of our approach is $(N_{\text{iter}} + N_{\text{Lanczos}}) \times N_{\text{eig}} \times N_{\text{pw}} \times N_{\text{v}}^2$, and it is proportional to the fourth power of the system size.

This workload represents a substantial improvement over that of conventional approaches (with explicit sums over all the conduction states), $N_{\text{pw}}^2 \times N_{\text{v}} \times N_{\text{c}}$, which is also proportional to the fourth power of the system size, but with a substantially larger prefactor. The number of occupied states N_{v} is often an order of magnitude smaller than the number of unoccupied states N_{c} required to converge summations in the dielectric matrix and Green's function. Furthermore, the number of eigenvectors N_{eig} is usually several orders of magnitude smaller than the number of PWs.

Recently, in addition to PDEP several other techniques were proposed, to improve the efficiency of GW calculations by removing the explicit summations over empty states entering the expression of Σ_c . For example, the approach of ref. 25 and 26 uses an optimal basis set to represent the polarizability; a Lanczos algorithm is then adopted to numerically compute an expression similar to eqn (59). In order to eliminate the summation over virtual states necessary to compute the optimal basis set, in ref. 26 the projector onto the virtual state subspace, \hat{Q} , was approximated by an expansion in plane-waves orthogonalized to the occupied state subspace. DFPT was also used in ref. 72 to avoid the calculation of empty states: the inverse dielectric matrix $\epsilon_{G,G'}^{-1}(\mathbf{q},\omega)$ was computed by solving eqs (54) for each perturbation, namely for each set of parameters $[\mathbf{q},G,\omega]$. The solution of such equation for all possible perturbations is computationally very demanding with PW basis sets, but it can be efficiently implemented in a localized basis set approach.⁷³ In ref. 74 and 75 the summation over empty states in the GW self-energy was avoided by defining and systematically approximating an effective energy that takes into account the contribution of all empty states. Finally we would like to mention that other approaches were proposed that, while retaining summations over empty states, attempt to reduce the number of unoccupied states needed⁷⁶ to reach convergence, or to approximate them by a combination of plane-waves and resonant orbitals.⁷⁷

3.2.3 Self-consistent GW calculations and vertex corrections. The G_0W_0 approach was used in most implementations appeared so far in the literature. However, fully or partially self-consistent calculations were performed using either the

full energy dependent GW self-energy^{69,78} or a static approximation.^{79,80} In some cases partial self-consistency was included, by approximating the quasi-particle wavefunctions at the DFT level of theory and performing a self-consistent calculation only on the energy levels (in G , in W , or in both).^{81,82} In ref. 83, it was suggested that GW quasi-particle wavefunctions can be accurately approximated by those obtained in self-consistent COHSEX calculations (eqn (34)); this approach was applied to bulk silicon, aluminum, and argon and gave reasonable estimates of self-consistent GW results, at a much lower computational cost. The usefulness of the GW self-consistent approach is still controversial; in some cases it was proven to decrease significantly the dielectric screening and to worsen the agreement between theory and experiment,⁸⁴ with respect to G_0W_0 .

Some implementations also attempted to go beyond the GW approximation and introduce vertex corrections by improving the approximation of Γ in eqn (29). A possible practical way to proceed consists in approximating the initial self-energy by the DFT (LDA) exchange and correlation potential $\Sigma(1,2) = V_{xc}(1)\delta(1,2)$.⁸⁵ After an iterative step of the Hedin's equations, one obtains an expression formally similar to the GW approximation (eqn (33)). However, in this case the reducible polarizability χ is approximated through eqn (42) and the screened Coulomb potential is obtained by using the inverse dielectric matrix in eqn (44). This formalism, called $GW\Gamma$, was applied to compute the quasi-particle spectrum of silicon and it was suggested that, although the computed quasi-particle gap is similar to that of the G_0W_0 approach, the vertex corrections might introduce substantial changes in the absolute position of the energy levels.^{85,86} In ref. 87 it was shown that the $GW\Gamma$ method improves the agreement with experiment for the values of the ionization potentials and electron affinities of several molecules (e.g. benzene and naphthalene) and it was also applied to the study of silicon nanoparticle electronic properties as a function of diameter.

3.3 Algorithms to solve the Bethe-Salpeter equation and compute optical spectra

In this section we first define the physical quantities related to optical absorption measurements in molecules and solids (Section 3.3.1) and we then present algorithms to solve the BSE and compute absorption spectra (Section 3.3.2). We close this section by comparing time dependent DFT and the BSE (Section 3.3.3).

3.3.1 Macroscopic polarizability and macroscopic dielectric function. In optical absorption or reflectivity experiments, for example by UV-vis spectrometry or ellipsometry, the intensity of the electromagnetic field of the incident light is much weaker than that of internal fields, and it can be treated within linear response theory. Here we discuss how the response functions that describe optical absorption experiments are calculated.

In molecules the macroscopic polarizability tensor α_{ij} relates the induced dipole (d^i) and the applied field E :

$$d_i^i(\omega) = \sum_j \alpha_{ij}(\omega) E_j(\omega), \quad (60)$$

where i and j indicate Cartesian coordinates; α is related to the retarded reducible polarizability (eqn (20)), by the equation $\alpha = \int r\chi(r, r') r' dr dr'$, where the external perturbing potential is $V_{\text{ext}} = -E(\omega) \cdot r'$, and r is proportional to the dipole induced in the system. The absorption coefficient $I(\omega)$ is proportional to the imaginary part of the trace of the dynamical polarizability tensor: $I(\omega) \propto \omega \text{Im}(\text{Tr}(\alpha(\omega)))$. For an isolated molecule there is no preferred orientation and one averages over the diagonal components of the macroscopic polarizability.

In the case of solids the optical absorption spectrum is given by the imaginary part of the macroscopic dielectric function, which is related to the dielectric matrix (a microscopic quantity) by:^{58,59}

$$\epsilon^M = \lim_{q \rightarrow 0} \frac{1}{\epsilon_{G=0, G'=0}^{-1}(q, \omega)}. \quad (61)$$

In principle eqn (61) requires the calculation of the full dielectric matrix and its inversion to obtain the single matrix element in the denominator. In practice, as shown in ref. 61, the value of ϵ^M (or α) may be obtained by computing the matrix element of the resolvent of an effective two-particle operator (such operator will be discussed below in Section 3.3.2); the eigenvalues of this operator correspond to the excitation energies of the system.

3.3.2 Density matrix perturbation theory formulation of the Bethe-Salpeter equation. Here we derive a specific form of the BSE using linear response theory applied to density matrices, and we present practical ways of computing neutral two-particle excitation energies as eigenvalues of an effective two-particle operator. The approach presented below may be considered as equivalent to solving a time-dependent Dyson's equation. We note that the formalism presented here may not be used to solve the full BSE of eqn (14); indeed only the response function χ of eqn (20) is considered, instead of the full (four-indexes) correlation function of eqn (13). As discussed in Sections 2.4 and 2.5, the response function χ is sufficient to describe optical absorption experiments. The starting point of our derivation is the quantum-Liouville equation (for simplicity we omit k -point labeling of states):

$$i \frac{d\hat{\rho}(t)}{dt} = [\hat{H}(t), \hat{\rho}(t)], \quad (62)$$

where the square brackets indicate commutators. Within a real space representation, we have $\rho(r, r', t) = \sum_{j=1}^{N_{\text{occ}}} \phi_j(r, t) \phi_j^*(r', t)$; here we use ϕ to indicate time-dependent orbitals and ϕ° to indicate unperturbed ground-state orbitals. The time-dependent quasi-particle Hamiltonian is:

$$\begin{aligned} & \int \hat{H}(r, r', t) \phi(r', t) dr' \\ &= \left(-\frac{1}{2} \nabla^2 + V_H(r, t) + V_{e-I}(r) + V_{\text{ext}}(r, t) \right) \phi(r, t) \\ &+ \int \Sigma(r, r', t) \phi(r', t) dr', \end{aligned} \quad (63)$$

where we assumed that the electron-ion potential is not modified by the external potential $V_{\text{ext}}(r, t)$. We consider a static approximation to the self-energy, hence Σ depends on time only

through the dependence on $\hat{\rho}(t)$. The static approximation is justified in the case of the COHSEX self-energy (eqn (34)) but not for the GW self-energy (eqn (33)), that includes dynamical effects and depends explicitly on $G^{(1)}$. The quasi-particle amplitudes f_j in eqn (3) and (4) are approximated by KS orbitals, as usually done in practical implementations to solve the BSE.^{29,47,88,89} However, the derivation below is valid in general as long as the $\{f_j(\mathbf{r})\}$ are an orthonormal basis set.

By considering \hat{V}_{ext} in eqn (63) as a small perturbation, the linearization of eqn (62) leads to:

$$i \frac{d\hat{\rho}'(t)}{dt} = \mathcal{L} \cdot \hat{\rho}'(t) + [\hat{V}_{\text{ext}}(t), \hat{\rho}^\circ], \quad (64)$$

$$\mathcal{L} \cdot \hat{\rho}'(t) = [\hat{H}^\circ, \hat{\rho}'(t)] + [\hat{V}'_H[\hat{\rho}'](t), \hat{\rho}^\circ] + [\hat{\Sigma}'[\hat{\rho}'](t), \hat{\rho}^\circ], \quad (65)$$

where variables with superscript “ \circ ” represent unperturbed quantities, and those with prime denote linear variations; specifically in this case $\hat{\rho}' = \hat{\rho} - \hat{\rho}^\circ$ denotes the linear variation of the charge density. Note the dependence of \hat{V}'_H and $\hat{\Sigma}'$ on the linear-response of the density matrix $\hat{\rho}'$. In eqn (65) a non-Hermitian operator \mathcal{L} acting on $\hat{\rho}'$ has been defined, which is known as Liouvillian super-operator,^{67,90} as its action is defined on a space of operators (the density matrices). By Fourier transforming eqn (65) into the frequency domain, one obtains

$$(\omega - \mathcal{L}) \cdot \hat{\rho}'(\omega) = [\hat{V}_{\text{ext}}(\omega), \hat{\rho}^\circ]. \quad (66)$$

The solution of this equation yields $\hat{\rho}'(\omega)$. If in eqn (66) the external perturbation is set to $V_{\text{ext}}(\mathbf{r}, \omega) = -\mathbf{E}(\omega) \cdot \mathbf{r}$, the response of the i -th component of the dipole in eqn (60) can be obtained as $d'_i(\omega) = \text{Tr}(\hat{r}_i \hat{\rho}'(\omega))$, where Tr indicates the trace operator. By solving explicitly eqn (66), we obtain the components of the polarizability tensor:

$$\alpha_{ij}(\omega) = -\langle \hat{r}_i | (\omega - \mathcal{L} + i\eta)^{-1} | \hat{r}_j, \hat{\rho}^\circ \rangle; \quad (67)$$

where η is a positive infinitesimal, and we wrote the scalar product of two operators A and B as $\langle \hat{A} | \hat{B} \rangle \equiv \text{Tr}(\hat{A}^\dagger \hat{B})$. The excitation energies of the system are obtained by diagonalizing \mathcal{L} (indeed the excitation energies correspond to the poles of the response function).

The formalism introduced here can be applied to any approximation of the non-local and static self-energy operator $\Sigma(\mathbf{r}, \mathbf{r}', \omega = 0)$ (see Table 5).

If $\Sigma(\mathbf{r}, \mathbf{r}') = V_{\text{xc}}(\mathbf{r})\delta(\mathbf{r} - \mathbf{r}')$ the adiabatic TDDFT formalism is recovered.^{67,90} Here we consider the COHSEX self-energy given in eqn (34) and we call the corresponding Hamiltonian H_{COHSEX} . Since this self-energy depends explicitly on the density matrix, it can be easily linearized and inserted in eqn (65). This approach can be considered as a time-dependent COHSEX method and the corresponding equations are equivalent to the BSE with static screening in the electron-hole interaction.

3.3.2.1 Electron-hole representation. The practical solution of eqn (67) requires a basis set for $\hat{\rho}'$. A commonly used one is the ensemble of occupied and virtual states of the unperturbed Hamiltonian, as the only non zero matrix elements of $\hat{\rho}'$ are

Table 5 The choice of the self energy (first column) in the solution of the quantum Liouville equation within first order perturbation theory (see eqn (63)), determines the level of theory used in the calculation of absorption spectra (second column), including time-dependent (TD) Hartree-Fock (HF) and density functional theory (DFT) and the Bethe-Salpeter Equation (BSE) (see text)

Self-energy	Level of theory
$\Sigma(\mathbf{r}, \mathbf{r}') = V_{\text{xc}}(\mathbf{r})\delta(\mathbf{r} - \mathbf{r}')$	TD-DFT in the adiabatic approximation
$\Sigma = \Sigma_{\text{HF}}$ $\Sigma_{\text{HF}}(\mathbf{r}, \mathbf{r}', t) = -\sum_{\mathbf{v}} \phi_{\mathbf{v}}(\mathbf{r}, t) \phi_{\mathbf{v}}^*(\mathbf{r}', t) v(\mathbf{r}, \mathbf{r}')$	TD-HF
$\Sigma = \Sigma_{\text{COH}} + \Sigma_{\text{SEX}}$ $\Sigma_{\text{COH}}(\mathbf{r}, \mathbf{r}') = \frac{1}{2} \delta(\mathbf{r} - \mathbf{r}') (W(\mathbf{r}, \mathbf{r}') - v(\mathbf{r}, \mathbf{r}'))$ $\Sigma_{\text{SEX}}(\mathbf{r}, \mathbf{r}', t) = -\sum_{\mathbf{v}} \phi_{\mathbf{v}}(\mathbf{r}, t) \phi_{\mathbf{v}}^*(\mathbf{r}', t) W(\mathbf{r}, \mathbf{r}')$	Statically screened BSE

those between unperturbed occupied and virtual orbitals:⁶⁷ $\langle \phi_{\mathbf{c}}^\circ | \rho' | \phi_{\mathbf{v}}^\circ \rangle$ and $\langle \phi_{\mathbf{v}}^\circ | \rho' | \phi_{\mathbf{c}}^\circ \rangle$. Note that $\langle \phi_{\mathbf{v}}^\circ | [\hat{r}_j, \hat{\rho}^\circ] | \phi_{\mathbf{v}}^\circ \rangle = \langle \phi_{\mathbf{c}}^\circ | [\hat{r}_j, \hat{\rho}^\circ] | \phi_{\mathbf{c}}^\circ \rangle = 0$, $\forall \mathbf{v}, \mathbf{v}'$ and \mathbf{c}, \mathbf{c}' ; $\langle \phi_{\mathbf{v}}^\circ | \hat{r}_i | \phi_{\mathbf{v}}^\circ \rangle \neq 0$ and $\langle \phi_{\mathbf{c}}^\circ | \hat{r}_i | \phi_{\mathbf{c}}^\circ \rangle \neq 0$, however one needs only the matrix elements $\langle \phi_{\mathbf{c}}^\circ | \hat{r}_i | \phi_{\mathbf{v}}^\circ \rangle$ and $\langle \phi_{\mathbf{v}}^\circ | \hat{r}_i | \phi_{\mathbf{c}}^\circ \rangle$ when computing⁶⁷ the scalar product (trace) in eqn (67).

This so called electron-hole basis set is used in many current implementations to solve the BSE.^{29,30,47,91-93} Within this framework, for spin singlet excitations the operator \mathcal{L} takes the form:³⁰

$$\mathcal{L} = \begin{pmatrix} \mathcal{D} + 2\mathcal{K}^{1x} - \mathcal{K}^{1d} & 2\mathcal{K}^{2x} - \mathcal{K}^{2d} \\ -2\mathcal{K}^{2x*} + \mathcal{K}^{2d*} & -\mathcal{D} - 2\mathcal{K}^{1x*} + \mathcal{K}^{1d*} \end{pmatrix}, \quad (68)$$

where \mathcal{D} , the exchange terms \mathcal{K}^{1x} and \mathcal{K}^{2x} and the direct terms \mathcal{K}^{1d} and \mathcal{K}^{2d} are defined as

$$\mathcal{D}_{\mathbf{vc}, \mathbf{v}'\mathbf{c}'} = (\varepsilon_{\mathbf{c}} - \varepsilon_{\mathbf{v}}) \delta_{\mathbf{vv}'} \delta_{\mathbf{cc}'}, \quad (69)$$

$$\mathcal{K}_{\mathbf{vc}, \mathbf{v}'\mathbf{c}'}^{1x} = \int \phi_{\mathbf{c}}^{\circ*}(\mathbf{r}) \phi_{\mathbf{v}}^\circ(\mathbf{r}) \frac{1}{|\mathbf{r} - \mathbf{r}'|} \phi_{\mathbf{v}'}^{\circ*}(\mathbf{r}') \phi_{\mathbf{c}'}^\circ(\mathbf{r}') d\mathbf{r} d\mathbf{r}', \quad (70)$$

$$\mathcal{K}_{\mathbf{vc}, \mathbf{v}'\mathbf{c}'}^{1x} = \int \phi_{\mathbf{c}}^{\circ*}(\mathbf{r}) \phi_{\mathbf{v}}^\circ(\mathbf{r}) \frac{1}{|\mathbf{r} - \mathbf{r}'|} \phi_{\mathbf{v}'}^{\circ*}(\mathbf{r}') \phi_{\mathbf{c}'}^\circ(\mathbf{r}') d\mathbf{r} d\mathbf{r}', \quad (71)$$

$$\mathcal{K}_{\mathbf{vc}, \mathbf{v}'\mathbf{c}'}^{1d} = \int \phi_{\mathbf{c}}^{\circ*}(\mathbf{r}) \phi_{\mathbf{c}'}^\circ(\mathbf{r}) W(\mathbf{r}, \mathbf{r}') \phi_{\mathbf{v}'}^{\circ*}(\mathbf{r}') \phi_{\mathbf{v}}^\circ(\mathbf{r}') d\mathbf{r} d\mathbf{r}', \quad (72)$$

$$\mathcal{K}_{\mathbf{vc}, \mathbf{v}'\mathbf{c}'}^{2d} = \int \phi_{\mathbf{c}}^{\circ*}(\mathbf{r}) \phi_{\mathbf{v}}^\circ(\mathbf{r}) W(\mathbf{r}, \mathbf{r}') \phi_{\mathbf{c}'}^{\circ*}(\mathbf{r}') \phi_{\mathbf{v}'}^\circ(\mathbf{r}') d\mathbf{r} d\mathbf{r}', \quad (73)$$

and W is the statically screened Coulomb interaction (namely the static limit of the Fourier transform of eqn (24)). In eqn (69) $\varepsilon_{\mathbf{c}}$ (conduction) and $\varepsilon_{\mathbf{v}}$ (valence) are quasi-particle energies. In principle these energies should be approximated at the COHSEX level of theory, for consistency with the choice of

the Hamiltonian; in practice a more accurate approximation may be chosen and usually the GW approximation is adopted to evaluate the term \mathcal{D} in eqn (69).

The matrix form of the operator \mathcal{L} , as defined by eqn (69)–(73), can be diagonalized to obtain the excitation energies of the system. Alternatively, a linear system involving \mathcal{L} can be solved in order to compute the macroscopic polarizability defined by eqn (67). Note that the operator \mathcal{L} in eqn (67) is non-Hermitian and thus the solution of the corresponding eigenvalue problem may not be achieved by using iterative solvers adopted for Hermitian problems. For this reason Hermiticity is often enforced by neglecting the off-diagonal blocks of \mathcal{L} ; this approximation is known as the Tamm–Dancoff approximation (TDA).⁹⁴ The TDA greatly reduces the computational complexity of the BSE solution and has successfully predicted the absorption spectra of several solids.^{29,30,47,95–97} However, the TDA does not always hold: for example it does not account for plasmons in solids⁹⁸ and it breaks down for some confined systems,^{34,99,100} such as carbon nanotubes¹⁰⁰ and silicon clusters.³⁴

The definition of \mathcal{L} through eqn (69)–(73) requires the calculation of the unoccupied single particle states (virtual orbitals) of the unperturbed Hamiltonian and the corresponding matrix must be explicitly evaluated and stored. A large number of virtual orbitals ϕ_c° is usually necessary for calculations that require the evaluation of a spectrum in a large energy range and/or involve large systems; even for small molecules, obtaining converged spectra may be challenging, in cases where the inclusion of many virtual states is necessary.¹⁰¹

3.3.2.2 Use of density functional perturbation theory. The explicit inclusion of virtual orbitals ϕ_c° may be avoided with the use of DFPT.⁵⁴ In this framework one considers the projector operator onto the unperturbed empty state subspace $\hat{Q} = \hat{I} - \hat{P} \equiv \hat{I} - \sum_{j=1}^{N_{\text{occ}}} |\phi_j^\circ\rangle\langle\phi_j^\circ|$, where \hat{I} is the identity operator; the evaluation of \hat{Q} only requires the evaluation of the occupied states ϕ_v° . At variance from the electron–hole representation, the operators entering eqn (66) (ρ' , \hat{r}_i and $[\hat{r}_j, \hat{\rho}^\circ]$) are expressed in the so-called *batch* representation,^{34,67} and eqn (69)–(73) become:

$$\mathcal{D}_{v,v'}|a_{v'}\rangle = \left(\hat{H}_{\text{COHSEX}}^\circ - \varepsilon_{v'}\right)\delta_{v,v'}|a_{v'}\rangle, \quad (74)$$

$$\mathcal{K}_{v,v'}^{1x}|a_{v'}\rangle = \hat{Q}\left(\int \frac{1}{|r-r'|}\phi_{v'}^{\circ*}(\mathbf{r}')a_{v'}(\mathbf{r}')d\mathbf{r}'\right)|\phi_v^\circ\rangle, \quad (75)$$

$$\mathcal{K}_{v,v'}^{2x}|b_{v'}\rangle = \hat{Q}\left(\int \frac{1}{|r-r'|}b_{v'}^*(\mathbf{r}')\phi_v^\circ(\mathbf{r}')d\mathbf{r}'\right)|\phi_v^\circ\rangle, \quad (76)$$

$$\mathcal{K}_{v,v'}^{1d}|a_{v'}\rangle = \hat{Q}\left(\int W(\mathbf{r},\mathbf{r}')\phi_{v'}^{\circ*}(\mathbf{r}')\phi_v^\circ(\mathbf{r}')d\mathbf{r}'\right)|a_{v'}\rangle, \quad (77)$$

$$\mathcal{K}_{v,v'}^{2d}|b_{v'}\rangle = \hat{Q}\left(\int W(\mathbf{r},\mathbf{r}')b_{v'}^*(\mathbf{r}')\phi_v^\circ(\mathbf{r}')d\mathbf{r}'\right)|\phi_v^\circ\rangle, \quad (78)$$

where for a generic operator \hat{A} , the so called “batch” components $|a_{v'}\rangle$ and $|b_{v'}\rangle$ are defined as:

$$|a_{v'}\rangle = \hat{Q}\hat{A}|\phi_v^\circ\rangle \quad (79)$$

$$\langle b_{v'}| = \langle\phi_v^\circ|\hat{A}\hat{Q}. \quad (80)$$

The index v runs over the number N_{occ} of occupied states. Hence in this representation no calculation of virtual orbitals is necessary. As a result the required computational workload is comparable to that of a ground state HF calculation. Specifically, in a plane wave (PW) representation, the evaluation of \mathcal{K}^{1d} and \mathcal{K}^{2d} scales as $\kappa[N_v^2 \times N_{\text{pw}} \times \ln N_{\text{pw}}]$, where κ is constant with respect to system size however, within an electron–hole approach, the evaluation of \mathcal{K}^{1d} and \mathcal{K}^{2d} scales as $\kappa[N_c \times N_v \times N_{\text{pw}} \times \ln N_{\text{pw}}]$, where N_c is in general much larger than N_v .

As mentioned in the previous section, quasi-particle corrections to the unoccupied states may be introduced either through the COHSEX Hamiltonian of eqn (74) or through more accurate quasi-particle corrections (*i.e.*, GW corrections), as discussed in ref. 31 and 34.

In principle, the evaluation of the statically screened Coulomb potential W entering eqn (77) and (78) requires summations over empty states; these are avoided by computing the dielectric matrix as described in Section 3.1.2.

Although in general the size of the operator \mathcal{L} in the DFPT-based representation (see eqn (74)–(78)) is larger than in the electron–hole representation, the full matrix does not need to be built explicitly. Indeed iterative techniques, that require only matrix by vector multiplications, are used to diagonalize \mathcal{L} or to solve the corresponding linear system in eqn (67). The operator \mathcal{L} can be efficiently applied to a vector by exploiting techniques developed for ground-state calculations, such as fast Fourier transforms used in plane-wave implementations of ground state DFT calculations. The DFPT-based approach described in this section was applied to the calculation of the optical properties of molecules (an example is shown in Fig. 1) and solids without relying on the Tamm–Dancoff approximation;⁹⁴ either the non-Hermitian Lanczos algorithm developed in ref. 34 and 67, was used or diagonalization was carried out with the algorithm of ref. 102.

3.3.3 Comparison between calculations using time dependent DFT and the Bethe–Salpeter equation. TDDFT is an alternative approach to the Bethe–Salpeter equation to compute neutral excitations of materials. In principle TDDFT is a formally exact theory.¹³ However, in practical calculations it is necessary to approximate the exchange–correlation potential $V_{\text{xc}}(\mathbf{r},\omega)$ and, within the linear response regime, the corresponding kernel $K^{\text{xc}}(\mathbf{r},\mathbf{r}',\omega) \equiv \delta V_{\text{xc}}(\mathbf{r},\omega)/\delta\rho(\mathbf{r}',\omega)$ (see eqn (41)). The most commonly used forms of the TDDFT kernel rely on the adiabatic approximation.⁵² The latter consists in using local, semi-local or hybrid functionals commonly adopted in ground-state calculations, to approximate the TDDFT kernel by discarding memory effects ($\omega = 0$). This approximation accurately reproduced the excitation energies of molecules but it is known to fail to describe excitons in extended systems.¹⁰³

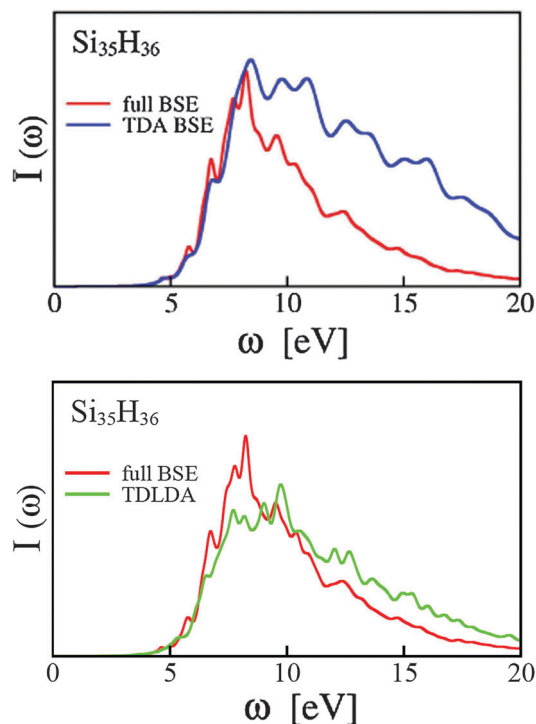


Fig. 1 Absorption spectra of a 1 nm hydrogenated Si cluster ($\text{Si}_{35}\text{H}_{36}$) as obtained by using many body perturbation theory and the techniques to solve the Bethe–Salpeter equation (BSE) described in Section 3.3.2.2 and in ref. 34. Results without (full BSE) and with the Tamm–Damcoff approximation (TDA) are presented in the upper panel. The lower panel compares the full BSE results with time dependent DFT results obtained using the LDA approximation (TDLDA).

In contrast, the Bethe–Salpeter equation appears to describe more accurately the electron–hole interaction in extended systems.^{29,47,89}

Recently, there have been several attempts to improve the accuracy of TDDFT for extended systems. For example the approximate long-range kernel $K^{\text{xc}} = -\alpha/|\mathbf{q} + \mathbf{G}|^2$ was found accurate for the calculation of the absorption spectra of several solids.^{103,104} The final result depends on the parameter α , which is system dependent. A more systematic way to find an approximation of K^{xc} for solids relies on the comparison between the BSE and the TDDFT equations.¹⁰⁵ Since K^{xc} depends only on two indexes (eqn (42)) and Ξ depends on four indexes (eqn (14)), this comparison is possible by considering a symmetrized version of eqn (42), in its dynamical form. This approach requires the calculation of GW quasi-particle corrections and the same matrix elements involved in the solution of the BSE equation in the electron–hole representation (eqn (69)–(73)). In ref. 106 and 107 an xc kernel was developed by requiring TDDFT reproduce the perturbative expansion of the BSE in terms of the screened Coulomb interaction; at the first order this approach is equivalent to the one of ref. 105. In general the TDDFT kernels derived from the BSE are dynamical ones (K^{xc} depends on ω) and include the correct long-range limit $1/|\mathbf{q} + \mathbf{G}|^2$. Many of the absorption spectra of solids computed by BSE-based kernels are in excellent agreement

with experimental spectra; the computational cost of this method is comparable to that of solving the full BSE.

Recently, Sharma *et al.*¹⁰⁸ proposed a new approximation for K^{xc} , that gives accurate results for the optical properties of solids within TDDFT. This kernel, called bootstrap kernel, takes the form

$$K_{\text{boot}}^{\text{xc}}(\mathbf{q}, \omega) = \frac{\epsilon^{-1}(\mathbf{q}, \omega = 0)}{\chi_0^{00}(\mathbf{q}, \omega = 0)}, \quad (81)$$

where χ_0^{00} indicates the $G = G' = 0$ component of the independent-particle polarizability in eqn (49), while ϵ^{-1} is the static inverse dielectric matrix. The bootstrap kernel (eqn (81)) is designed to reproduce the correct asymptotic behavior $1/|\mathbf{q} + \mathbf{G}|^2$ necessary to describe the optical spectra of extended systems. Since the kernel itself depends on ϵ^{-1} , the numerical solution of the TDDFT equations must be performed self-consistently. At the first iteration K^{xc} is set to 0, eqn (42) (in its dynamical form) is solved to determine χ , which is then used to compute the inverse dielectric matrix ϵ^{-1} through eqn (22); by inserting ϵ^{-1} in eqn (81), one can compute a new approximation for K^{xc} and the procedure is repeated until self-consistency is achieved. Since local or semi-local functionals are known to underestimate electronic gaps, the independent-electron polarizability χ_0 used in the bootstrap kernel is approximated starting from GW or LDA + U^{109–111} calculations. The bootstrap kernel was applied to different systems including small to medium band gap bulk semiconductors and materials with strongly bound excitons, such as LiF and noble gas solids;¹⁰⁸ for the cases considered so far a good agreement with experiments was found.

We now turn to the application of the many body techniques described in Sections 2 and 3 to the calculations of electronic excitations in materials used as photocathodes and photoanodes in photoelectrochemical cells.

4 Band edge and absorption spectra calculations of semiconductor photoelectrodes

In this section we first briefly recall the basic steps involved in photoelectrochemical (PEC) energy conversion and we introduce the excitation processes of interest; we then focus on specific materials. In each case we will point out the effects on the final results, of the numerical approximations described in Section 3. The main goal of this section is to illustrate what can be computed at present using MBPT, which physical properties can be predicted and how calculations may contribute to interpret specific measurements of interest for PEC cells.

The photoelectrochemical path to water splitting involves separating the oxidation and reduction processes into half reactions. Photoelectrolysis, or semiconductor-based PEC water splitting, can be accomplished by following two main strategies:^{2,112} one uses photovoltaic (PV) modules connected directly to electrolyzers and/or catalytic electrodes; another one uses semiconductor–liquid junctions, where water splitting occurs at the semiconductor surface. The latter has several advantages over

carried out which, depending on the surface morphology, may require the use of large supercells.

In the following, we discuss the computation of quasi-particle gaps and band alignment for representative bulk materials (Section 4.1.1) and surfaces (Section 4.1.2). We focus on TiO₂ and WO₃ as promising photoanode materials and on silicon with functionalized surfaces as a promising photocathode material. We recall that TiO₂ has been extensively used as a photoanode material,^{129–133} since the pioneering experiments of Fujishima and Honda.¹³⁴ Tungsten trioxide (WO₃) has also been considered as a good photoanode material in the study of PEC water-splitting systems because it has sufficient absorption within the solar spectrum to generate modest photocurrents, good electron transport properties, and stability against photocorrosion.¹³⁵

With a band gap of 1.12 eV, p-type Si (p-Si) is a desirable small band gap absorber for use as photocathode in dual band gap p/n-PEC water splitting configurations.¹³⁶ Several groups demonstrated that a p-Si photocathode, combined with metal catalysts, can be used to produce H₂ electrochemically with a reduced voltage.^{137,138} For example, photon to hydrogen conversion efficiencies as high as 6% was reported for p-Si decorated with Pt nanoparticles.¹³⁸ Other Earth abundant metal catalysts such as Ni or Ni–Mo can be alternatives to Pt¹³⁹ to provide similar photoelectrode efficiencies when deposited onto Si microwire arrays. BiPt alloys¹⁴⁰ were also shown to have improved catalytic activity to hydrogen evolution reaction performance, compared with pure Pt.

4.1.1 Calculations of band edges of bulk materials. Here we illustrate state of the art calculations for the band edges of bulk materials and we discuss in particular the case of TiO₂ and WO₃.

The quasiparticle gap of rutile TiO₂ was measured using different spectroscopies: XPS-BIS (X-ray photoelectron and bremsstrahlung isochromate spectroscopy) experiments reported a value of 3.3 ± 0.5 eV¹⁴¹ while UPS-IPS (ultraviolet photoemission spectroscopy and inverse photoemission spectroscopy measurements) yielded 3.6 ± 0.2 eV¹⁴² (data are not available for anatase). The difference between XPS-BIS and

UPS-IPS data may be representative of the difference between bulk and surface fundamental gaps, as the former spectroscopy is expected to probe the bulk region, and the latter surface layers.¹⁴³ Both gaps are obtained from a linear extrapolation of the leading edges of the integrated photoemission spectra, which do not allow one to discern between surface and bulk states. Computed values of the TiO₂ quasiparticle gap are shown in Table 6. Overall the agreement between GW calculations (see Section 2.6) and measured values is good, with computational results varying within 3.4–3.8 eV.

Differences between the various calculations stem from several factors, encompassing the basis sets chosen, the way summation over empty states are carried out and the calculation of (or model for) the frequency dependence of the dielectric matrix (see Section 2.7). Ref. 144 pointed out that the use of a plasmon-pole model for the frequency dependence of dielectric matrices^{21,145} results in a significant overestimate of the quasiparticle gap of TiO₂. Therefore, the use of different procedures to compute the matrix elements of dielectric matrices as a function of frequency could be partially responsible for the different GW results obtained in ref. 144 and 146. We note that variations of G₀W₀ quasiparticle gaps depending on the chosen ground state wavefunctions and eigenvalues – e.g. from LDA/PBE, PBE + U or screened hybrid functionals (HSE06)¹⁴⁷ ground state calculations – are non-negligible, ranging from 0.3–0.6 eV (see Table 6). Self-consistent GW calculations for rutile TiO₂,⁸⁰ which in principle eliminate the dependence on the ground state eigenvalues and eigenfunctions, give a band gap of 3.78 eV, larger than all the results obtained at the G₀W₀ level of theory.^{80,144,146,148,149}

Results for the electronic properties of WO₃ are not as abundant as for TiO₂. Recently¹⁵⁷ we computed the band gaps of WO₃ at several levels of theory: LDA, modified Δ SCF¹² and G₀W₀.¹⁵⁷ All calculations were carried out at the experimental geometry, given the lack of consensus in geometrical parameters found using, e.g. LDA, PBE, or Van der Waals density functionals.¹⁵⁸ As shown in Table 7, the computed G₀W₀ quasiparticle gap is 3.26 eV for RT-monoclinic WO₃, in

Table 6 Calculated electronic band gaps (eV) of rutile and anatase (TiO₂) using different levels of theory, specified in the first column (acronyms defined in the text). Most GW results are at G₀W₀ level; the rutile direct gap (3.78 eV) was obtained⁸⁰ with self consistent GW calculations

Theory	Rutile $E_{\text{gap}}^{\text{Direct}}$	Rutile $E_{\text{gap}}^{\text{Indirect}}$	Anatase $E_{\text{gap}}^{\text{Direct}}$	Anatase $E_{\text{gap}}^{\text{Indirect}}$
LDA	1.75 ¹⁴⁴		2.44 ¹⁴⁴	2.01 ¹⁴⁴
PBE	1.88, ^{149–151} 1.77, ¹⁵² 1.93, ¹⁴⁶ 1.82 ¹⁴⁸		2.36, ^{150,151} 2.43 ¹⁴⁶	2.05, ^{150,151} 2.15, ¹⁴⁶ 1.94, ¹⁴⁹ 2.08 ¹⁴⁸
PBE + U	2.83 ¹⁴⁸			3.27 ¹⁴⁸
HSE06	3.05, ¹⁵² 3.39 ¹⁴⁹			3.60 ¹⁴⁹
GW	3.38, ¹⁴⁴ 3.78, ⁸⁰ 3.59, ¹⁴⁶ 3.40, ¹⁴⁸ 3.46 ¹⁴⁹	3.34 ¹⁴⁴	4.14, ¹⁴⁴ 4.29 ¹⁴⁶	3.79, ¹⁵³ 3.56, ¹⁴⁴ 3.83, ¹⁴⁶ 3.70, ¹⁴⁸ 3.73 ¹⁴⁹
GWU	2.85 ¹⁴⁸			3.27 ¹⁴⁸
HSE06-GW	3.73 ¹⁴⁹			4.05 ¹⁴⁹
Exp(PES-IPES)	3.3, 3.6 ^{141,142}			

Ref. 144: experimental geometry; LDA-KS eigenvalues and wavefunctions; norm-conserving pseudopotentials; full frequency dependent dielectric matrix; energy cutoff (E_{cut}) = 60 (20) Ry for Σ_x (Σ_c); 160 bands included in the calculation of Σ . Ref. 146: geometry optimized at the PBE level; PBE-KS eigenvalues and wavefunctions; plasmon-pole approximation for the frequency dependent ϵ . Ref. 153: geometry optimized at the PBE level; PBE-KS eigenvalues and wavefunctions; norm-conserving pseudopotentials; E_{cut} = 36 (30) Ry for Σ_x (Σ_c); 100 bands included in the calculation of ϵ and Σ . Ref. 148: experimental geometry; PBE-KS eigenvalues and wavefunctions; Godby–Needs plasmon-pole model⁵¹ for the frequency dependent ϵ ; E_{cut} = 80 (10) Ry for Σ_x (Σ_c); 568 unoccupied bands included for ϵ and Σ ; U = 7.5 eV in GWU calculations. Ref. 149: PBE and HSE06 KS eigenvalues and wavefunctions; projector-augmented wave pseudopotentials;^{154,155} full frequency dependent dielectric matrix.¹⁵⁶ Ref. 80: LDA-KS eigenvalues and wavefunctions; GW calculations are self-consistent.

apparent good agreement with the results of UPS-IPES measurements (3.38 ± 0.2 ¹⁵⁹ and 3.28 ± 0.14 ¹²⁷).

However including relativistic effects (spin-orbit coupling) in our band structure calculations brings the G_0W_0 gap to a value of ~ 3.1 eV; this value is further decreased by ~ 0.2 – 0.3 eV once electron phonon interaction is taken into account by using a model Frölich Hamiltonian (see the value GW w/SO/e-ph in Table 7). Therefore our computed quasiparticle gaps appear to underestimate the measurements of ref. 127 and 159. We note that UV photoemission (UPS) experiments were performed using He I (21 eV) and He II (41 eV) excitations, which have great surface sensitivity and hence the measured gap is the gap of the surface, while our calculations were carried out for the bulk. Higher photo energies (e.g. hard X-ray measurements¹⁴³) are required to study the bulk properties of materials and avoid surface effects. Ref. 127 noted that an increased band gap at the surface of a polycrystalline semiconductor with respect to the bulk is not unusual. For example, the observed electronic surface band gap of CuInSe₂ films (1.4 eV)¹⁶⁷ is significantly larger than the corresponding optical bulk band gap (1.0 eV). Both structural as well as compositional differences between bulk and surface could be responsible for the observed enhancement of the surface band gap. Further studies are necessary to clarify the difference between surface and bulk WO₃ quasiparticle gaps.

To compare with optical measurements, we¹⁵⁷ computed the exciton binding energy by calculating the difference between the first excitation energy of optical spectra (obtained by solving the BSE) and the G_0W_0 gap; we found a value of 0.15 eV, bringing our computed optical gap, 2.7–2.8 eV (see entry before the last in Table 7), in agreement with the experimental value extrapolated from 300 K to 0 K (2.8–2.9 eV).¹⁶⁶

Table 7 Electronic band gap (eV) of monoclinic WO₃ computed using different levels of theory (acronyms are defined in the text). E_g^{opt} denotes the optical gap. The last column indicates whether the gap is direct (D), indirect (I) or pseudo-direct (PD). The values of I and D gaps differ by less than ~ 0.05 eV. From ref. 157

Theory	Band gaps [eV]	Type
LDA	1.87, ^c 1.31 ¹⁶⁰	D, PD
PW91	0.90, ¹⁶¹ 1.19 ^{162 b} 1.36, ^{162 b} 1.57 ^{162 b}	D
RPBE	1.73 ¹⁶³	ID
B3LYP	3.13 ¹⁶²	D
HSE06	2.80 ¹⁶²	D
PBE0	3.94, ^c 3.67 ¹⁶²	D
Δ SCF	2.92 ^c	—
G_0W_0	3.26 ^c	D
$G_0W_0(\text{w/SO}^a)$	3.16 ^c	D
$G_0W_0(\text{w/SO/e-ph}^a)$	2.86 ^c –2.96 ^c	D
Exp(UPS-IPES)	3.38 ± 0.2 , ¹⁵⁹ 3.28 ± 0.14 ¹²⁷	—
E_g^{opt}	2.71 ^c –2.81 ^c	D
$E_g^{\text{opt}}(\text{exp})$ ^{164–166}	2.6–2.7(300 K), 2.8–2.9(0 K)	ID, D

^a SO: spin orbit; e-ph: electron phonon. ^b Ref. 162 (PW91): 1.19 eV computed by ultrasoft pseudopotentials; 1.36 eV computed by PAW pseudopotentials; 1.57 eV computed by Gaussian-type basis sets with a linear combination of atomic orbitals approach. ^c In ref. 157 all band gaps were computed at the experimental geometry; the other calculations shown in the table were carried out at the optimized geometries of the corresponding functionals.

Systematic studies of the band gap of family of oxides within MBPT are rare; a recent one¹⁶⁸ considered the family of (A₂B'BO₆) V⁵⁺ and Cr⁶⁺ double perovskites. Different levels of theory were used, including LDA, HSE06 and G_0W_0 @LDA (i.e. G_0W_0 using KS eigenvalues and eigenfunctions computed at the LDA level). The authors found that the G_0W_0 @LDA results overestimate the optical gaps by an average of 0.92 eV. The overestimate is not surprising, as the electron–hole interaction is not included in the GW approximation; however, in these materials the exciton binding energies are expected to be of the order of 0.1–0.2 eV; thus their inclusion in the calculation is not expected to yield computed optical gaps in agreement with experiments. Therefore in ref. 168 a semi-empirical method was used to rationalize trends in computed gaps. The authors exploited the linear dependence of the electronic part of the static dielectric constants (ϵ_∞)¹⁶⁹ and the difference between the band edge Fock exchange energies (Δ_x) in d⁰ perovskite compounds; then they defined a semi-empirical correction to computed values by fitting the LDA gap errors as a function of ϵ_∞ and Δ_x . This semi-empirical approach successfully predicted the optical gaps of several perovskite oxides, spanning the visible region of the solar spectrum.

As mentioned at the beginning of this section, once quasiparticle gaps are computed, one needs to obtain absolute positions of the VBM and CBM with respect to vacuum in order to align band edges with water redox potentials. To define the absolute zero (vacuum level) of the electrostatic potential, a common practice is to construct a periodic cell containing a slab sufficiently thick to mimic the bulk of the material, and inclusive of a vacuum region large enough to avoid the interaction with neighboring replica. One then computes the average electrostatic potential in the bulk region ($\bar{V}_{\text{bulk-region}}$) of the slab relative to the vacuum region (V_{vacuum}). The value of $\bar{V}_{\text{bulk-region}}$ is usually very similar to that of the bulk materials (\bar{V}_{bulk})¹⁷⁰ as obtained with periodic bulk calculations. Therefore the VBM (CBM) of the bulk material can be computed relative to \bar{V}_{bulk} first and then the difference ($\Delta\bar{V}_{\text{bulk-vac}} = \bar{V}_{\text{bulk-region}} - V_{\text{vacuum}}$) is added in order to obtain the VBM (CBM) relative to the vacuum level. In most cases appeared in the literature, the calculation of average potentials was carried out at the LDA or PBE level of theory.

However, the VBM (CBM) obtained by local or semi-local DFT calculations may be inaccurate and in particular suffer from self-interaction errors. In order to solve this problem, GW corrections ($\delta E_{\text{VBM/CBM}}^{\text{QP}}$) to VBM/CBM energies obtained at the KS level were sometimes used.^{128,144,171} The equation to compute VBM/CBM relative to vacuum at the GW level can then be written as follows:

$$E_{\text{VBM/CBM}}^{\text{QP}} = \Delta\bar{V}_{\text{bulk-vac}} - \bar{V}_{\text{bulk}} + E_{\text{VBM/CBM}}^{\text{LDA}} + \delta E_{\text{VBM/CBM}}^{\text{QP}} \quad (82)$$

The band edge positions relative to vacuum are schematically shown in Fig. 3, where we also indicated a possible alignment with water redox potentials. We emphasize again that the band positions with respect to water redox potential depend not only

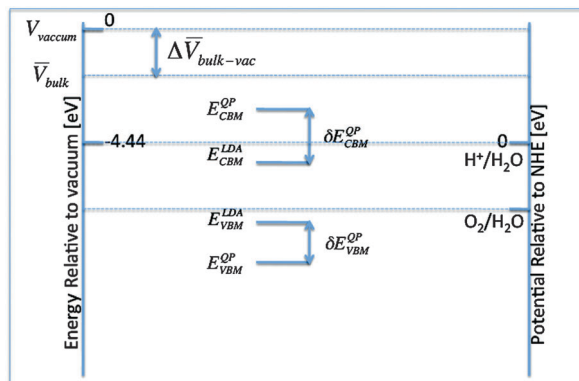


Fig. 3 Schematic computation of band edges with quasiparticle correction relative to vacuum and water redox potential (see text).

on the bulk properties but also on the hydration layer at the interface and on the specific chemical interactions leading to proton–electron transfers at the interface.

First principle calculations of band alignment between VBM/CBM of photoelectrodes and water redox potentials are not abundant, especially at a level of theory higher than local or semilocal DFT.^{119,121,124} In the following, we briefly summarize some examples of band edge calculations at the GW level of theory. The authors of ref. 144 used eqn (82) to compute the TiO₂ rutile VBM alignment with the vacuum level, obtaining 7.8 eV, which compares well with the experimental values^{172,173} of 8.0–8.2 eV. The authors of ref. 128 computed instead the BGC first, following the theorem by Perdew and Levy¹⁷⁴ stating that the exact Kohn–Sham band structure predicts exactly the center of the fundamental energy gap relative to the vacuum level. However, in ref. 128 BGC was computed by approximate KS band structure calculations (PBE+U and LDA+U for FeO); a slab model (BGC_{slab}), referenced to the electrostatic potential in the vacuum region was adopted and the band gaps were obtained for the bulk system ($E_{g,bulk}$) using the GW approximation. Finally the VBM and CBM energies relative to vacuum were obtained from (BGC_{slab} – 1/2 $E_{g,bulk}$) and (BGC_{slab} + 1/2 $E_{g,bulk}$) respectively. This approach was applied to several TMOs, for which the BGC_{slab} was found to be insensitive to the parameters used in the (DFT+U) calculations and to the chosen exchange correlation functional (e.g. HSE06 or PBE0).¹²⁸ The difference between experimental and calculated values of the VBM of several TMOs (MnO, FeO, Fe₂O₃, NiO, Cu₂O) computed at the (DFT+U) optimized geometries varied between 0.1 and 0.9 eV.¹²⁸

A slightly different approach was proposed to compute the GW corrections of the bulk KS-VBM energies (δE_{bulk}^{QP}) in ref. 171: ($E_{VBM}^{QP} = \delta E_{VBM,bulk}^{QP} + E_{VBM,slab}^{KS} - V_{slab-vac}$); this approach implicitly assumes that the GW corrections for the bulk KS-VBM ($\delta E_{VBM,bulk}^{QP}$) are similar to the ones for the slab ($\delta E_{VBM,slab}^{QP}$). The method¹⁷¹ was applied to the computation of VBM and CBM of molybdenum and tungsten dichalcogenides MX₂ (M = Mo and W; X = S and Se) which are considered to be promising photocathode materials. The authors of ref. 171 found errors of 0.1–0.2 eV, compared with experimental values.

We now turn to the calculations of surface band edges with a specific focus on silicon and protected silicon surfaces.

4.1.2 Calculations of band edge of surfaces. Many semiconductor surfaces are not stable in air or water and they readily oxidize. As a consequence, their properties as photoelectrode materials may be greatly degraded. Therefore widespread efforts were devoted to protect semiconductor surfaces from oxidation, especially in the case of silicon. For example, it was found that methyl-terminated silicon surfaces^{136,175,176} with close to complete coverage can effectively inhibit oxidation. Unfortunately methyl termination is also an effective barrier towards further useful chemistry, e.g. to covalently attach catalysts for hydrogen production. Lewis' group pioneered research into using mixed surface functionality^{177,178} to balance the two goals of stability and reactivity to useful chemistry. Another important effect of surface functionalization is to modify the photoelectrochemical device energetics¹³⁶ through covalent chemical modifications, so as to eliminate the pH dependence of the band edge position of the solid,¹³⁶ while allowing for pH control of the electrochemical potentials of the H⁺–H₂ and O₂–H₂O systems.¹⁷⁹ In this way, one can effectively manipulate the relative position of the band edges of the solid and the H₂O redox potentials.

Several *ab initio* studies of the electronic structure of functionalized Si surfaces were published recently^{180–182} at the semi-local DFT level of theory, and only few using the GW approximation.^{183,184} The authors of ref. 183 studied the electronic and spectroscopic properties (STM and STS) of the hydrogen terminated Si(111)-(1 × 1) surface using both LDA and GW calculations, and some of their results are shown in Table 8. The table reports the results of G₀W₀(GW₀) calculations for both the energy positions of surface states and the electronic gap; a comparison is also given with experiments and other studies.¹⁸⁵ Note the differences of 0.3–0.5 eV from previous calculations (e.g. ref. 185), which may stem from the use of a specific plasmon-pole model (PPM) approximation²¹ in ref. 185, instead of direct frequency integration as done in ref. 183 (see Section 3.1.1). The explicit frequency dependence employed in the direct integration, although more accurate than the PPM, yields valence-band width and surface states in worse agreement with experiments. This discrepancy could be due, at least in part, to inaccuracies of the non self-consistent G₀W₀ treatment of the electronic structure.

Interestingly, as shown in Fig. 4, self-energy corrections lead to a downward shift of surface states (red solid lines) relative to the VBM, with respect to their corresponding positions found at the LDA level; on the other hand, the energy position of surface resonance states (dashed blue lines in Fig. 4) relative to the VBM as obtained within LDA is almost unaffected by self-energy corrections because of their bulk-like nature.

As mentioned previously, the methyl-termination of Si(111) surfaces constitutes a promising protection from oxidation. Ref. 193 studied the structural and electronic properties of the methyl-terminated Si(111) surface, which were found to be very similar to those of the hydrogen-terminated Si(111).

Table 8 Quasiparticle energies computed at the $G_0W_0(GW_0)$ level of theory for a 12-layer H-Si(111) slab. We report the valence-band width (E_W), the band gap between $\bar{\Gamma}$ and \bar{M} ($E_g^{\bar{\Gamma}-\bar{M}}$), and energies of surface states at \bar{K} and \bar{M} relative to the VBM. Frequency integration was performed with the contour deformation method (ref. 186), full frequency integration (No PPM) or by using plasmon-pole models proposed by Godby and Needs [ref. 51(GN)] and by Hybertsen and Louie [ref. 21(HL)]. All energies are in eV. Reprinted with permission from ref. 183. Copyright 2010 by the American Physical Society

	No PPM	GN	HL	HL ^a	HL (ref. 185)	Expt. (ref. 187 and 188)
E_W	11.6 (11.7)	11.3 (11.3)	11.8 (12.0)	11.9 (12.1)		12.5 ± 0.6
$E_g^{\bar{\Gamma}-\bar{M}}$	1.46 (1.53)	1.45 (1.54)	1.48 (1.57)	1.32 (1.41)		1.32
\bar{K}	-3.49 (-3.54)	-3.52 (-3.57)	-3.62 (-3.69)	-3.68 (-3.75)	-3.82	-3.80
	-4.37 (-4.44)	-4.43 (-4.49)	-4.49 (-4.57)	-4.62 (-4.68)	-4.76	-4.78
	-7.96 (-8.03)	-8.04 (-8.10)	-8.28 (-8.44)	-8.38 (-8.52)	-8.47	-8.64
\bar{M}	-4.13 (-4.19)	-4.18 (-4.24)	-4.30 (-4.38)	-4.38 (-4.46)	-4.63	-4.76

^a Parameters used for GW calculations were extracted from ref. 185, with 350 empty states and energy cutoffs of 11.6 Ry, 7.8 Ry and 4.4 Ry for ϵ , bare exchange, and dynamical part of Σ , respectively.

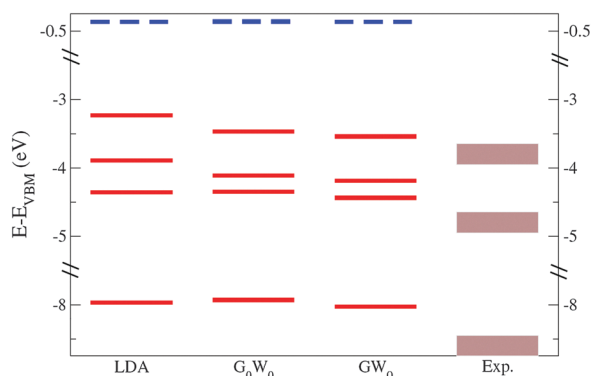


Fig. 4 Energy levels of surface states of the hydrogen terminated Si(111)-(1 × 1) surface at \bar{K} and \bar{M} (red solid line) and the surface resonance state at $\bar{\Gamma}$ (blue dashed line) relative to the valence-band maximum, as predicted by three different levels of theory: LDA, G_0W_0 , and GW_0 . Energy positions of measured surface states are shown as thick horizontal bars with thickness equal to the width (~ 0.3 eV) of experimental photoemission spectra. Reprinted with permission from ref. 183. Copyright 2010 by the American Physical Society.

For example, no states in the gap are induced by the presence of the adsorbate; VBM and CBM states remain bulk-like. More complex than the hydrogen-terminated Si(111) surface, the description of the methyl-terminated one requires the inclusion of van der Waals (vdW) dispersion forces between the methyl groups, which were taken into account by the DFT + D approach¹⁹⁴ in ref. 193.

As to more complex functionalizations, a study was recently reported in ref. 184. By comparing H-, CH_3 -, C_2H_5 -, Cl- and Br-terminated Si(111) surfaces, the authors of ref. 184 found that GW calculations are required to accurately compute the absolute positions of the valence band edges with different surface terminations; however the relative shifts of band edges between different surface terminations may be well described at the DFT-LDA level, with results in good agreement with experiment, as shown in Table 9. Interestingly, ref. 184 also found that the sign and magnitude of surface dipole moments of different surface terminations follow a trend that may be explained by simple electronegativity rules. Such a trend may be useful to understand other surfaces and predict the relative band edge shift and surface dipole with additional surface terminations. Similar concepts were discussed in ref. 195, where it was shown that by changing the size and orientation of the ligand's intrinsic dipole moment *via* functionalization, one can control the direction and magnitude of the shifts of the electronic level of another material, CdSe, and thus the band alignment with water redox potentials.

4.2 Absorption spectra of semiconductor photoelectrodes

Similar to the previous section, we separate our discussion into bulk systems (4.2.1) and surfaces (4.2.2). We close this section with a discussion of absorption spectra of nanostructures (4.2.3).

4.2.1 Absorption spectra of bulk systems. We now turn to calculations of optical spectra and again we consider TiO_2 , WO_3 and silicon as representative examples.

Table 9 Band gaps (E_g) and ionization potentials (IPs) of H-, CH_3 -, C_2H_5 -, Cl-, and Br-terminated Si(111) surfaces, and relative IP with respect to that of H-Si(111) ($\Delta IP_{R:H}$) (all energies are in eV). Reprinted from ref. 184

R-	LDA		G_0W_0		Exp. IP [$\Delta IP_{R:H}$]
	E_g^a	IP [$\Delta IP_{R:H}$]	E_g	IP [$\Delta IP_{R:H}$]	
H-	0.73	4.83 [$\equiv 0$]	1.53	5.46 [$\equiv 0$]	5.29 ^b 5.31 ^c
CH_3 -	0.70	4.06 [-0.8]	1.50	4.71 [-0.8]	4.80 ^b [-0.5], 4.76 ^c [-0.6], [-0.7], ^d [-0.6] ^e
C_2H_5 - ^f	0.72	3.83 [-1.0]	1.53	4.52 [-0.9]	4.94 ^b [-0.4], 4.79 ^c [-0.7], [-0.7], ^d [-0.7] ^e
Cl-	0.65	5.89 [1.1]	1.46	6.56 [1.1]	[1.2-1.5], ^g [0.7] ^d
Br-	0.62	5.59 [0.8]	1.44	6.27 [0.8]	[0.5] ^d

^a E_g was evaluated between $\bar{\Gamma} = \{0,0,0\}$ and $\bar{M} = \{1/2,0,0\}$. ^b Ref. 189 and 190, high-resolution synchrotron photoelectron spectroscopy measurements. ^c Ref. 191, estimated from barrier heights of Hg-Si junctions using forward bias J - v data as: $IP = W_f^{Hg} - q\Phi_{b,J-v} + E_g$, where $W_f^{Hg} = 4.49$ eV is the work function of Hg and E_g is assumed to be 1.12 eV. ^d Ref. 184, determined from UPS measurements of the work function shift and estimated band bending. ^e Ref. 184, similar to ref. 191 but using C_{diff} - V data. ^f Surface coverage of the C_2H_5 -Si(111) surface was estimated to be 0.6 in ref. 184 and 65–95% in ref. 190, while a full coverage was assumed in ref. 184. ^g Ref. 192, Kelvin probe measurements.

Optical properties of TiO₂ (rutile and anatase) were studied from first principles in several papers.^{144,146,149,196} Ref. 144 and 146 compared TiO₂ rutile (anatase) BSE absorption spectra with experimental reflectivity measurements over an energy range of 2–12 eV (2–25 eV).^{197,198} Computed BSE absorption spectra well reproduced the main absorption onset found experimentally near 4 eV and the intensity up to 6 eV of both rutile and anatase (see Fig. 5). However, several questions remain open: (i) The experimental fundamental optical gap of rutile is 3.03 eV while the UPS-IPES yields an electronic gap of 3.3–3.6 eV. The difference between the two measurements can not be explained by the first exciton binding energy¹⁹⁹ which is only 4 meV for rutile, as from measurements of low temperature absorption spectra.¹⁹⁹ (ii) The calculated first exciton binding energy is 0.13 eV¹⁴⁴ for rutile, which is two orders of magnitude larger than the experimental one and the calculated lowest excitation energy position exceeds the measured one by 0.22 eV. (iii) The systematic overestimate of the oscillator strength of the BSE spectra compared with TiO₂ experimental spectra in the high energy range (above 8 eV) is not understood. Ref. 144 suggested that the discrepancy between experimental and theoretical exciton binding energies as well as the lowest excitation

energy position could be due to electron phonon interaction, which was not included in the GW-BSE calculations; the overestimation of oscillator strength at higher energy might be due to the use of the Tamm–Dancoff approximation (see Section 3.3.2) and the assumption of statically screened Coulomb interactions.

Calculations of optical properties of WO₃ were reported only for the simple cubic structure. The structure of room temperature (RT) monoclinic WO₃ differs from that of simple cubic only by the location of the W atoms, that are off the octahedra centers and the tilt angles between octahedra deviate from 180° by 15°–25° in the RT-monoclinic phase. As a result, the electronic structure of simple cubic and monoclinic WO₃ are similar: the top of the valence band consists of the O 2p states and the bottom of the conduction band is composed of W 5d states (slightly hybridized with O 2p states). The transitions between O 2p states and W 5d states are allowed.

Most experimental absorption spectra of WO₃^{165,200,201} are measured by UV-vis spectrophotometers, over a narrow energy range nearby the fundamental absorption edge, and they are likely to be very sensitive to optical transitions with small intensity. Instead, measurements of reflectivity (*e.g.* with synchrotron radiation or by using ellipsometry) over a large energy range far from the absorption edge are less sensitive to the details of the edge, *e.g.* phonon assisted transitions. As computed BSE spectra of WO₃ do not include any phonon assisted transitions and electron phonon interaction was not included, it is meaningful to compare the computed GW-BSE calculations with the experimental ellipsometry spectrum. However, the experimental results for pure single crystal WO₃ are very limited²⁰² and rather uncertain: the authors of ref. 202 who measured pure WO₃ and sodium bronze's reflectivity by ellipsometry noted that their WO₃ samples may not behave as single crystals from an optical standpoint; ellipsometric measurements are probably influenced by contributions from domains with different crystallographic orientations, giving rise to an artificial double peak in the absorption spectra along one of the axes. To the best of our knowledge, no other reflectivity or absorption measurements of WO₃ over a wide energy range is available. Therefore in ref. 157 we compared the computed WO₃ BSE spectrum with that of sodium bronze (Na_{0.65}WO₃), which has a band structure similar to that of simple cubic WO₃: the extra electrons from Na fill the conduction bands of simple cubic WO₃²⁰³ without modifying the original band structure. As a consequence the WO₃ spectrum is similar to that of Na_xWO₃ ($x = 0.4$ – 1), except for a free-electron contribution at lower energies (about 2 eV below the onset of interband transitions). Fig. 6 shows the comparison between the spectrum of WO₃ computed by the BSE and the experimental sodium bronze (Na_{0.65}WO₃) one measured by reflectivity. The overall shape of the computed BSE spectrum is in good agreement with experiment.

Although WO₃ is a good photoanode material for oxidizing water, it is not an efficient absorber of sunlight because its large band gap falls on the ultraviolet-and-blue tail of the solar spectrum. Extensive work was done to reduce the band gap of

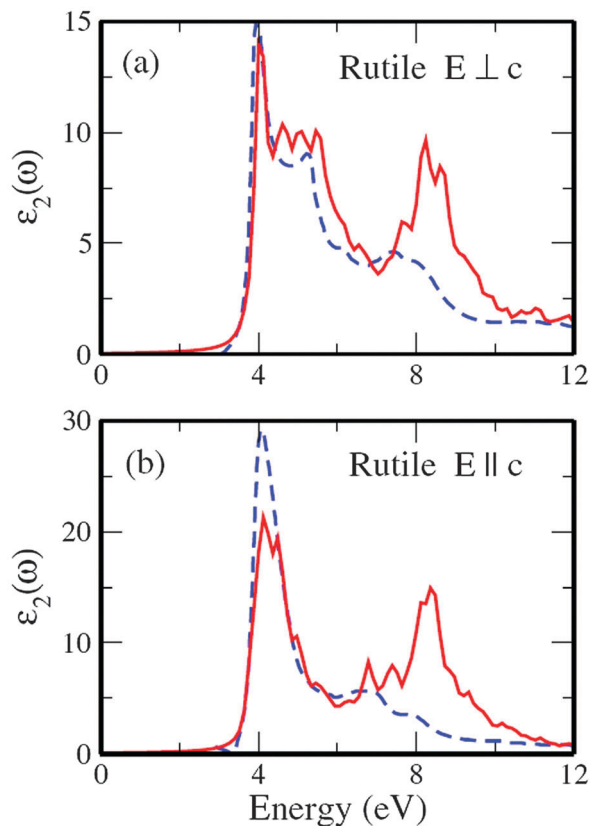


Fig. 5 The imaginary part of the frequency dependent dielectric function $\epsilon_2(\omega)$ of rutile from 0 to 12 eV. Solid curves are theoretical calculations with the BSE, and dashed curves are experimental results obtained at room temperature. In (a) the direction of polarization is perpendicular to the tetragonal axis *c*, and in (b) the direction of polarization is parallel to axis *c* (from ref. 144). Reprinted with permission from ref. 144. Copyright 2010 by the American Physical Society.

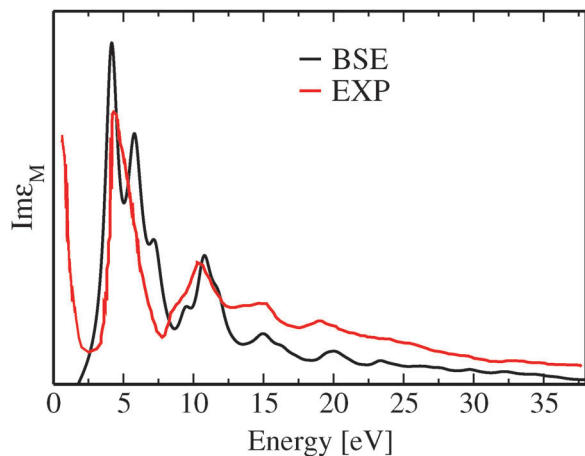


Fig. 6 Absorption spectrum ($\text{Im}\epsilon_M$) of WO_3 computed by solving the Bethe–Salpeter Equation (BSE) and that of $\text{Na}_{0.65}\text{WO}_3$ obtained by reflectivity experiments²⁰⁴ (EXP). A Lorentzian broadening of 0.04 Ry was added to the computed curve. The low energy rise of the experimental spectra is due to extra electrons from Na filling the bottom of the conduction band (see text). Reprinted from ref. 157.

WO_3 in order to optimize the visible light absorption, for example by atomic substitutions *e.g.* nitrogen (N).²⁰⁰ However, the high concentration of substituted N required for a significant decrease of the band gap gives rise to charged defects and increases carrier recombination rates, thus leading to a poor photocurrent density. Recent work by ref. 158 and 205 showed that molecular clathrates *e.g.* monoclinic WO_3 intercalated with nitrogen molecules can decrease its band gap up to 0.8 eV without introducing charged defects. The computed GW-BSE absorption spectrum of N_2 intercalated WO_3 ¹⁵⁷ (or $\text{N}_2@ \text{WO}_3$) shows two main features: the absorption edge is red shifted compared with that of pure WO_3 , consistent with the experimental observation; the oscillator strength of the first two peaks is redistributed to higher energy. This indicates that the N_2 presence increases the screening of the electron hole interaction and hence it decreases the exciton binding between electron and hole pairs. Indeed, the calculated lowest exciton binding energy decreased by 0.05 eV upon N_2 intercalation. The redistribution of the oscillator strength to higher energy is not ideal for solar applications; however, the presence of N_2 is mostly beneficial as the light absorption within the visible spectrum is enhanced by the presence of the molecule.

As in the previous section, after discussing the oxides, we turn to silicon. Optical properties of bulk silicon were extensively studied theoretically. Good agreement with experimental results was obtained using GW-BSE approaches.^{29,30,91} In particular, ref. 31 computed the absorption spectrum of bulk silicon by solving the BSE without explicitly including empty states, and using the approach described in Section 3.3 (see Fig. 7). The computed spectrum exhibits accurate position and intensity of the two main peaks, compared to experiments, with an error of at most 0.12 eV for the first (E_1) transition. However, the computed spectrum also shows a weak additional peak between the two main transitions that has a strong dependence

on the k -point mesh used in the calculation. This extra peak was also found in some of the earlier BSE calculations and in other recent publications.⁹¹ We note that even though the well accepted value of bulk silicon exciton binding energy is only 14.7 ± 0.4 meV,²⁰⁶ excitonic effects significantly modify the shape of the absorption spectra. For example TDLDA calculations (which do not contain any excitonic effect) yield an absorption threshold much lower than found both experimentally and using the BSE; in addition, the TDLDA spectrum exhibits a shoulder instead of a main peak.

The BSE and TDLDA spectra shown in Fig. 7 only involve direct optical transitions. The optical transitions between the indirect (1.1 eV) and direct band gap (3.4 eV²⁰⁷) of Si, which capture the main part of visible light absorption is not included in Fig. 7. Recently, ref. 208 studied the phonon-assisted interband optical absorption spectrum of bulk silicon at the quasi-particle level of theory. The calculated spectra near the onset of the indirect absorption are in good agreement with experimental measurements for a range of temperatures, as shown in Fig. 8. We note that the theoretical absorption spectra of Fig. 8 were rigidly shifted downward in energy by 0.15–0.23 eV in order to match the onset of the experimental curves. The need for such a shift may arise from finite-temperature effects that were not explicitly considered in the GW calculations of ref. 208. Moreover, the sharp features that appear near the onset of the experimental absorption spectrum were attributed to excitonic effects, which were not taken into account in the calculations. As noted in ref. 208, the modification of absorption spectra by excitonic effects is expected to be weaker for indirect optical transitions than for direct ones; this is due to the location of the band-extrema wave functions in indirect-gap materials, which are at different points in the BZ, resulting in smaller wave-function overlaps and hence smaller magnitude of the Coulomb interaction between an electron and a hole pair, than in the case of direct transitions.

4.2.2 Absorption spectra of surfaces. In this section, we consider absorption spectra of TiO_2 and silicon surfaces.

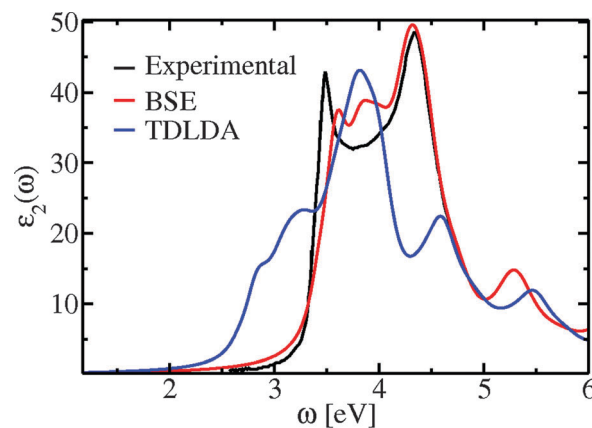


Fig. 7 Absorption spectrum of bulk silicon computed by solving the BSE and with the TDLDA, compared to the experimental results. A Lorentzian broadening of 0.11 eV has been added to the computed curves. Reprinted with permission from ref. 31. Copyright 2012 by the American Physical Society.

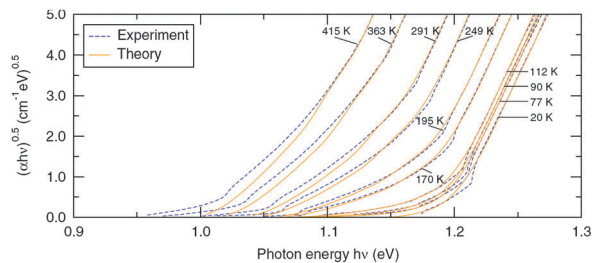


Fig. 8 Onset of the phonon-assisted optical absorption in silicon, as a function of photon energy and temperature. The theoretical results (solid lines) are in good agreement with experimental ones (dashed lines). Experimental data are from ref. 209. The theoretical curves were shifted horizontally to match the onset of the experimental spectra. Reprinted with permission from ref. 209. Copyright 2012 by the American Physical Society.

A particularly important role in the photocatalytic performances of anatase TiO_2 is played by the exposed surfaces.²¹⁰ the minority (001) facets seem to be more reactive^{211,212} than other orientations and present a lower concentration of defects^{213,214} compared to other anatase orientations and rutile surfaces. Both (1×4) reconstructed and (1×1) clean unreconstructed surfaces were obtained under particular experimental conditions. The connection between the optical properties and the structure of anatase $\text{TiO}_2(001)$ surfaces was studied in ref. 210. As shown in Fig. 9(c), the anatase surfaces and bulk anatase density of states (DOS) are similar except for a peak, mainly associated to the VBM states of the (1×1) unreconstructed and (1×4) reconstructed surfaces, respectively. Despite the similarity of DOS between the two reconstructed surfaces, Fig. 9(a) and (b) show that the VBM states have distinct characters on the two surfaces, which significantly affect the optical absorption. For example, the optical spectrum of the (1×4) reconstructed surface computed by GW-BSE (Fig. 10(d)) appears to be very similar to that of bulk anatase, while for the (1×1) unreconstructed surface, optical absorption is present below the first bulk absorption peak B_1 (Fig. 10(c)). The physical origin of the different optical absorption of the two surfaces is related to the different characters of the VBM states shown in Fig. 9(a) and (b) respectively. In addition, the experimentally observed enhanced photocatalytic activity of anatase nanostructures with a high percentage of (001)- (1×1) facets was explained by the different types of electron-hole spatial distributions between two reconstructed surfaces.²¹⁰ For example, in the (1×4) reconstructed anatase surface the exciton is completely delocalized in the subsurface region and bulk part of the slab; this is not a favorable configuration for electron and hole separation and subsequent chemical reactions of water splitting. Instead, in the (1×1) unreconstructed surface electrons and holes are spatially separated and both present at the surface, which is a desired feature for the photo-induced splitting of water molecules. These results suggest that anatase with (001) orientation, mainly its (1×1) unreconstructed surface, is photocatalytically efficient.²¹⁵

We now turn to silicon surfaces and before presenting specific results, we recall the effects of surface states on optical

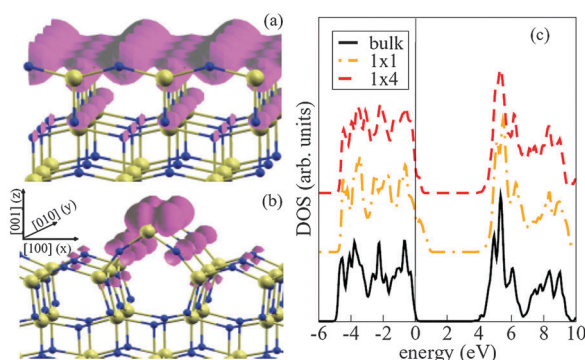


Fig. 9 (a) Large yellow (small, blue) spheres represent Ti(O) atoms for the (1×1) -(001) surface. Magenta isosurface: $|\psi|^2$ of the VBM, at Γ (at 1% of its maximum value). (b) As in (a) but for the (1×4) -(001) surface. (c) DOS of bulk anatase (black full line), (1×1) -(001) (dotted-dashed yellow line), of (1×4) -(001) (red dashed line). Reprinted with permission from ref. 210. Copyright 2011 by the American Physical Society.

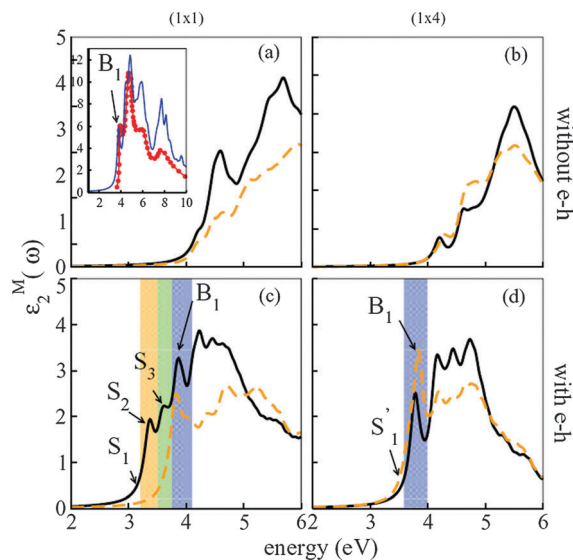


Fig. 10 Macroscopic dielectric function $\epsilon_2^M(\omega)$ for (1×1) (left column) and (1×4) -(001) (right column) case. (a) and (b) Spectra calculated at independent quasiparticle level. (c) and (d) As before but calculated including the local-field effects and the e-hole coulomb attraction. The black solid (orange dashed) curves are for light polarized along the $[100]$ ($[010]$) direction. Inset of panel (a): bulk BSE (blue curve) and experimental (red diamonds, ref. 36) spectrum for light polarized perpendicular to c . The arrows indicate the exciton energies under consideration. Reprinted with permission from ref. 210. Copyright 2011 by the American Physical Society.

absorption as they play an important role in the case of Si. For example, reconstructed surfaces such as $\text{Si}(111)-(2 \times 1)$ ^{216,217} or $\text{Si}(100)-(c4 \times 2)$ ²¹⁸ exhibit surface states in the middle of the bulk fundamental gap and these determine the main features of their reflectance anisotropy spectroscopy (RAS) or surface differential reflectivity (SDR) spectra; on the other hand, the passivation of the surface dangling bonds by hydrogen results in no surface states in the energy region probed by RAS *e.g.* for the $\text{Si}(110)\text{-H}$ terminated surface.²¹⁹ We also recall that the

basic features of surface absorption probes, RAS^{220,221} and SDR.^{222–224} RAS measures the difference in reflectance (ΔR) of normal incidence plane-polarized light between two orthogonal directions in the surface plane (x, y) normalized to the mean reflectance (R_0):

$$\frac{\Delta R}{R_0} = \frac{R_y - R_x}{R_0}. \quad (83)$$

SDR yields the relative change in reflectivity between the clean (R_{clean}) and adsorbate-covered (R_{ads}) surfaces:

$$\frac{\Delta R}{R} = \frac{R_{\text{clean}} - R_{\text{ads}}}{R_{\text{ads}}}. \quad (84)$$

The two methods are complementary: RAS yields the subtle difference of reflectance between two directions, which can be a small quantity, if the optical response of the surface is only weakly anisotropic; SDR yields instead the change of the surface optical reflectance due to the coverage. In general, the adsorbates bound to surface atoms are expected to suppress the presence of surface states in semiconductors. Consequently, the SDR spectra give mainly the contribution of the surface states to the surface reflectance.²¹⁸

When modeling a semiconductor solid within the repeated slab approach, the RAS can be calculated for normally incident light by:²²⁵

$$\frac{\Delta R_i(\omega)}{R_0(\omega)} = \frac{4\omega d}{c} \text{Im} \frac{4\pi(\alpha_{xx}^{\text{hs}}(\omega) - \alpha_{yy}^{\text{hs}}(\omega))}{\epsilon_b(\omega) - 1} \quad (85)$$

where $\epsilon_b(\omega)$ is the bulk macroscopic dielectric function (see eqn (61)); α_{ii}^{hs} ($i = x, y$) is the half-slab polarizability, obtained, e.g. by eqn (67); d is half of the slab thickness.

Calculations of surface optical spectra using MBPT are much more demanding than the corresponding ones for bulk materials. For example, the convergence of BSE spectra as a function of the size of supercells is much slower than the one of ground state calculations because of the long range electron hole interaction; in addition, many atomic layers are usually required to build a slab with a thickness appropriate to describe surface perturbed bulk wave functions. Calculations with thin slabs may overestimate excitonic effects due to insufficient screening. Furthermore, in several bulk semiconductors, self-energy corrections rigidly shift the conduction band energies, providing some theoretical basis for the use of scissor operators.²²⁶ However, such an approximation is usually not justified for surfaces, especially when surface states are present.^{183,217} In general, inclusion of self-energy corrections leads to a non-uniform shift of optical transition energies, affecting the RAS lineshape rather than simply shifting the energy scales.

Optical properties of Si surfaces were extensively studied. For example, calculations for the monohydride Si(001)-(2 × 1) surface,²²⁷ showed that the GW corrections and excitonic effects play a crucial role in achieving good agreement with experiments, while the local field effects appear to be less important, similar to the case of Si(110):H surface.²¹⁹ In ref. 227, the measured RAS signal is characterized by positive

and negative peaks around 3.4 and 4.3 eV, arising from surface induced bulk anisotropy or intrinsic contributions. Interestingly, the Si(001)-(2 × 1) clean surface with dangling bonds²¹⁸ has a reflectance anisotropy (RA) signal around 1.5 eV because of surface states π - π^* transition, which is strongly reduced in the case of monohydride Si(001)-(2 × 1) surface. Indeed the adsorbed H atoms on the monohydride Si(001)-(2 × 1) surface suppresses the presence of surface states which contribute to the RA signal around 1.5 eV in the Si(001)-(2 × 1) clean surface case.

4.2.3 Absorption spectra of nanostructured electrodes. For the last example of first principle calculations of realistic materials for PEC cells, we turn to nanostructured systems. Nanostructured electrode morphologies can be used to address some of the intrinsic limitations of bulk materials for PEC applications.²²⁸ The most obvious advantage of a nanostructured morphology is the increase of surface to volume ratio. The increase in the number of surface sites greatly enhances the overall charge transfer kinetics at the semiconductor/electrolyte interface and relaxes catalytic activity requirements. The second advantage is the shorter diffusion path lengths for the photogenerated charge carriers in one dimensional (1D) nanostructures. For example, in a traditional planar device, photogenerated carriers must cross the entire thickness of the cell in order to be collected before recombination. The cell thickness is dictated by how much material is necessary to absorb the incoming light. By using nanowires, the direction of light absorption and the direction of carrier collection is orthogonalized. For high-aspect ratio nanowires (*i.e.*, wires having a high length/radius ratio), the length necessary for full optical absorption can be readily obtained, while the distance over which carriers are collected can be minimized, being only the radius of the nanowire; such a design offers the potential for efficient charge-carrier collection from even very impure, low diffusion length materials.² Similar advantages are offered by nanostructures based on cauliflower-type morphologies or randomly packed spheres.^{229,230} The third possible advantage of using nanostructured materials is the so called quantum confinement effect. It is known²³¹ that spatial confinement of charge carriers to a volume that is less than their De Broglie wavelength results in a widening of the band gap. Even though the resulting blue shift of the absorption spectrum is usually not desirable for PEC absorbers, the widening of the band gap could be designed to shift the conduction or valence band edge toward ideal directions (band edge positions that straddle the water reduction and oxidation potentials),^{232,233} thus decreasing the required bias potential and increasing the solar to hydrogen conversion efficiency.

Despite nanoparticles being widely utilized for dye sensitized solar cell (DSSC) applications, their utilizations as photoelectrodes in photoelectrochemical cells for separating hydrogen and oxygen production is relatively rare.²²⁸ This is because the discrete nature of nanoparticle energy levels can be a major disadvantage for charge transport. However, some three-dimensional nanostructures (such as the cauliflower type hematite materials²²⁹) consisting of interconnected nanoparticles could offer higher accessible surface areas than

conventional bulk structure; and the interlinked branches could lead to superior charge transport. Several nanocrystalline films^{234–237} were reported for solar water splitting applications, for example nanocrystalline films of Fe₂O₃,²³⁴ WO₃,²³⁰ BiVO₄²³⁶ and Cu₂O.²³⁷

A great amount of research on the syntheses and characterizations of 1D nanostructures for solar water splitting purposes was reported, including TiO₂ nanotube²³⁸/nanowires,²³⁹ WO₃ nanowires,²⁴⁰ as well as silicon nanowires.^{241,242} Experimentally it was shown that Si nanowires (SiNW) have enhanced absorption and carrier collection for photovoltaic and PEC applications.^{241,242} In addition, porous silicon samples which closely resemble the geometry structure of free-standing Si rods, were investigated in photoelectrochemical cells.²⁴³ Introduction of a network of ~2–3 μm diameter, ~80 μm long pores into Si was found to lead to energy-conversion efficiencies in excess of 10%.

Many theoretical studies appeared in the literature on the optical properties of SiNW.^{244–250} Two fundamental effects were taken into account in order to obtain physically sound results:²⁵¹ (i) local field effects, which lead to a strong suppression of the absorption of light polarized perpendicular to the NW axis, dramatically increasing the optical anisotropy of the system; (ii) excitonic effects, which are stronger in one dimensional systems, due to the spatial overlap between electron and hole wavefunctions. Due to excitonic effects, the absorption spectra of wires can be red shifted and their oscillator strength can be redistributed, with respect to those of the bulk. Using a GW-BSE framework, the above two effects are both included in the calculations.

First principle calculations of optical spectra of wires are still challenging and numerical accuracy needs to be carefully controlled. Ref. 250 extensively discussed how to control all the numerical parameters entering such calculations and how to evaluate error bars on computed spectra. It is key to take into account numerical errors when comparing with experiments and with results obtained using the same level of theory, but different numerical techniques and algorithms. For example, the convergence of absorption spectra as a function of cell size is much more delicate at the BSE level of theory than within TDLDA, as the electron hole interaction is absent within TDLDA but present in BSE. The conventional cylindrical Coulomb cutoff²⁵² can speed up the convergence of cell sizes but cause slower convergence with *k* point sampling.²⁵⁰

Recent calculations showed that^{244,250} the absorption spectra of SiNWs depend significantly on the diameters, growth direction and surface structures. As an example, Fig. 11 shows the BSE spectrum for a 0.8 nm SiNW grown in the [110] direction with two different surface geometries, which are all hydrogen terminated. It is seen that in a broad energy range, the spectra are very sensitive to the surface structures. This indicates that care must be exercised when comparing theoretical and experimental results, as apparently small differences in the atomic arrangement may give rise to substantial differences in the band structure close to the Fermi level, and also to substantial differences in the matrix elements entering the

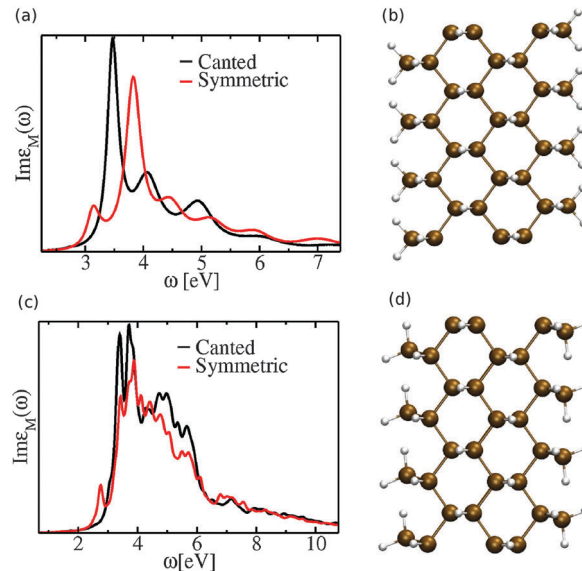


Fig. 11 Absorption spectra [$\text{Im}\epsilon_{\text{M}}(\omega)$] of a 0.8 nm Si nanowire grown in the [110] direction with canted (d) and symmetric (b) surface geometries (from ref. 250). (a) BSE spectra for Si NWs with different surface geometries. A cell size of 50 a.u. was used, and 16 *k* points for the BZ sampling, a kinetic energy cutoff of 12 Ry to solve the Kohn–Sham equations, the technique of ref. 63 and 70 to evaluate the Fock operator, and a Coulomb cutoff²⁵³ to evaluate the dielectric matrix. A scissor operator was obtained by computing the difference between the lowest energy gap within LDA and G_0W_0 . (c) TDLDA spectra for Si NWs with different surface geometries, obtained with a cubic cell of lateral dimension equal to 50 a.u. and 16 *k*-points for the BZ sampling. Reprinted with permission from ref. 250. Copyright 2012 by the American Physical Society.

definition of absorption spectra. An analysis of the band structure for the two geometries revealed the position of levels close to the top of the valence bands is influenced by the surface structure (*e.g.* the HOMO of the wire with a canted surface is 0.2 eV lower than that of the wire with a symmetric surface). The first peak to which the HOMO has a large contribution is blue shifted in the wire with a canted surface. However, in the wire with a canted surface the main excitonic peak is red shifted and merged with the first peak, indicating a stronger exciton binding. Differences are also visible at the TDLDA level (see Fig. 11(c)), especially in the low energy range, where transitions between levels close to the top of the valence bands and bottom of the conduction bands are involved.

Using GW-BSE calculations, ref. 244 obtained SiNW excitonic gaps in good agreement with the experimental photoluminescence gaps^{254,255} of porous silicon samples. The calculated exciton binding energy is 1.8 eV, much larger than the one of bulk Si (~14 meV); this result was explained by the confinement of electron hole wavefunctions in the nanowire structure.

Experimentally SiNW arrays instead of isolated SiNWs are used to build water splitting devices.²⁴¹ It is thus interesting to study how the interaction between wires modifies the optical absorption. Fig. 12 shows the RPA absorption spectra of SiNWs as a function of inter-wire distance ranging from 2.1 to 11.2 Å. As the local field effects strongly suppress the absorption of

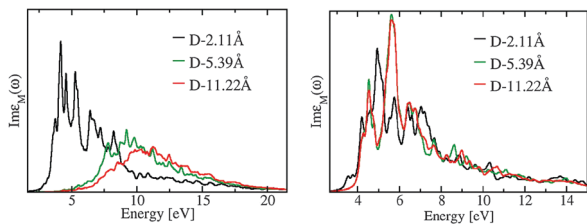


Fig. 12 Absorption spectra $[\text{Im}\epsilon_M(\omega)]$ of Si nanowires placed at different distances (D), computed within RPA with local field effects. Left: 0.4 nm Si nanowire grown in the [001] direction with light polarized perpendicular to the wire axis. Right: 0.4 nm Si nanowire grown in the [001] direction with light polarized parallel to the wire axis.

light polarized perpendicular to the NW axis, the optical absorption along the direction perpendicular to the wire axis starts after 5 eV for inter-wire distances larger than 5 Å. For distances larger than 9 Å, the absorption spectra of interacting and isolated NWs are very similar, indicating that the interaction is weak. Interestingly, as inter-wire distances decreases from 5 Å, the spectra along the perpendicular direction move towards the red part of the spectrum, indicating that the optical anisotropy is considerably decreased. At 2 Å inter-wire distance, the absorption edges in the parallel and perpendicular directions become very similar. By contrast, the absorption edge of light polarized parallel to the NW axis is almost unchanged as a function of the inter-wire distance, except at 2 Å. Although RPA spectra (including local field effects) do not include quasi-particle (QP) corrections and electron-hole (e-h) interaction, it is possible to use them to extract qualitative trends due to the partial cancellation of error arising from the two effects.²⁵¹ Ref. 244 found that for light polarized along the wire axis, a simultaneous reduction of the e-h interaction and of the QP gap correction result in an almost unchanged position of the BSE optical threshold, when comparing interacting with isolated SiNWs.

The influence of doping (n- or p-type) on the optical properties of SiNWs was not yet extensively studied. Some results were reported in ref. 247, where it was shown that peaks around 2 eV appear below the threshold of absorption of pure SiNWs, due to the presence of dopant related states. The quasiparticle corrections on the electronic gaps are only weakly dependent on the type of dopant, with variations of the order of 0.1 eV. The e-h exchange splittings of doped SiNWs, which can be compared with photoluminescence experiments, were computed by GW-BSE without considering spin-orbit interaction in ref. 247. A giant e-h exchange splitting, which is three times as large as that of bulk Si was predicted, and it can be explained by the dramatic enhancement of the e-h overlaps in the confined structure of SiNWs.

5 Conclusion and outlook

In summary, we presented the basic concepts underlying first principles calculations of charged and neutral excitations within many body perturbation theory (MBPT), with emphasis

on band structures and band edges, and on absorption spectra of solids. We focused on the properties of light absorbers used in photoelectrochemical cells. The theory was presented in Section 2 and the numerical methods were described in Section 3, while examples of specific calculations were given in Section 4.

In particular, we presented the basic definitions of Green's function theory and introduced the equations satisfied by single and two-particle Green's functions, the Dyson's equation^{18,36} and the Bethe Salpeter Equation²⁷ (BSE), respectively. The poles of the single particle Green's function represent the energies necessary to add or remove an electron from a given solid or molecule. These energies are directly comparable to those measured, *e.g.* in photoemission experiments. The poles of the correlation function defined from the two-particle Green's functions correspond to neutral excitation energies of interacting electrons. These neutral excitations may be, for example, an electron and a hole in a semiconductor, created by the interaction with incident light, and they are directly related to those measured in absorption experiments.

The Dyson's equation relates the single-particle Green's function to the effective many body potential of interacting electrons. Such complex interaction potential is called self-energy, and one may define a Schrödinger-like equation where the self-energy enters as a mean field potential acting on single-particle states. Those, among such states, with a long lifetime are called quasi-particles. The concepts of self-energy and quasi-particles are central concepts in MBPT, and in the interpretation of spectroscopic measurements of solids and molecules.

While the single-particle Green's function satisfies the Dyson's equation, the two body correlation function satisfies the BSE. The self-energy enters the Dyson's equation, while the derivative of the self-energy with respect to the single-particle Green's function enters the BSE. In the recent literature, solving the BSE to obtain absorption spectra has been the strategy of choice for most solids;^{28–31} in the case of molecules many calculations of absorption spectra are carried out using time dependent DFT.^{67,256–258} We emphasize that the BSE may be used for both molecules and solids and, in principle, for any material, irrespective of its morphology.

After introducing the basic concepts of Green's function theory, we discussed their relation to the key concepts entering linear response theory, including reducible and irreducible polarizabilities and the dielectric matrix. We used linear response theory to describe optical absorption experiments because the electric field of the incident light (the perturbation) is small compared to the internal field of the system. One of the key quantities of linear response theory and MBPT is the dielectric matrix, which describes how an external perturbing potential is screened within a solid and a molecule, by the presence of interacting electrons. The dielectric matrix is also used to define an effective, screened Coulomb potential (W) acting among the electrons. Using a perturbative series in terms of the screened Coulomb potential and an approximation of the self-energy in terms of such potential, we introduced the GW approximation⁴³ to compute quasiparticle energies.

Calculations at the GW level of theory represent the most advanced computations of band structures and band edges carried out at present for complex materials, including photoelectrodes.

Having established the basic concepts of Green's function, many body perturbation and linear response theories, we turned from theory to computation. We discussed numerical techniques to compute quasi-particle energies and optical spectra, with emphasis on algorithms that do not require the explicit calculation of empty (virtual) single particle states. Such algorithms are instrumental in making possible calculations of large systems and thus of realistic materials. We emphasize that in order to assess the accuracy of the theory, numerical parameters need to be controlled with great care. The same level of theory implemented with different levels of accuracy, from a numerical standpoint, may lead to qualitatively different predictions or interpretation of experiments. An example of such differences was presented for the optical gaps of TiO₂ and WO₃.

In our discussion of specific calculations, we chose representative photoanode and photocathode materials and we summarized MBPT results of band edges and absorption spectra. We mostly focused on two oxide materials for the photoanode, TiO₂ and WO₃ and on silicon for the photocathode, with emphasis on functionalized silicon surfaces.

Although much progress was made in recent years to compute the electronic properties of molecules and solids from first principles, beyond approximate DFT theories, outstanding challenges remain in the theoretical and computational description of materials for photoelectrochemical energy conversion. An accurate determination of band alignments of photoelectrodes with water redox potentials requires the explicit calculation of the electronic properties of semiconductor-liquid interfaces. This remains a challenging task, as it encompasses the determination of the interface structural properties, and GW calculations of systems with possibly thousands of electrons. Although GW calculations for systems containing several hundreds of electrons^{24,25} are now feasible, they are not yet routine tasks: they require substantial computational resources and are thus difficult to carry out for multiple samples at a time (and multiple samples may be required, e.g. to investigate different types of defects at the interface). In addition simulations of liquid water themselves, even in the absence of interfaces, are challenging,^{259,260} as the level of theory necessary to obtain, at the same time, reasonably good structural and electronic properties is yet unclear. Furthermore, one would need to simulate water with dissolved ions under different pH conditions, interfaced with a semiconductor, not just pure water. An accurate description of certain solvated ions (e.g. most of the anions) requires the use of hybrid functionals,²⁶¹ as semi-local ones often yield an incorrect localization of the charge around the anion, and hybrid functional calculations of liquid water are still computationally demanding²⁵⁹ for large samples. As for absorption spectra, even with methods that avoid the explicit calculation of empty single particle states, the solution of the BSE for several hundreds of electrons is a heavy computational task. In addition

improvements of the theory are necessary to include indirect transitions at the absorption onset and electron-phonon interaction.

We note in closing that here we only dealt with light absorbers for water splitting and thus with electronic structure calculations; clearly one will need to go beyond static electronic properties and acquire capabilities to describe charge transport, in order to fully understand water splitting processes.

This work was supported by the grant NSF-CHE-0802907. We thank Michiel Sprik and Márton Vörös for a critical reading of the manuscript, and Marco Govoni and Tuan Anh Pham for useful discussions.

References

- 1 N. S. Lewis and D. G. Nocera, *Proc. Natl. Acad. Sci. U. S. A.*, 2006, **103**, 15729–15735.
- 2 M. G. Walter, E. L. Warren, J. R. McKone, S. W. Boettcher, Q. Mi, E. A. Santori and N. S. Lewis, *Chem. Rev.*, 2010, **110**, 6446–6473.
- 3 P. Hohenberg and W. Kohn, *Phys. Rev.*, 1964, **136**, B864–B871.
- 4 R. M. Martin, *Electronic Structure Basic Theory and Practical Methods*, Cambridge University Press, 2004.
- 5 W. Kohn and L. J. Sham, *Phys. Rev.*, 1965, **140**, A1133–A1138.
- 6 F. Herman, J. P. Van Dyke and I. B. Ortenburger, *Phys. Rev. Lett.*, 1969, **22**, 807–811.
- 7 A. D. Becke, *Phys. Rev. A: At., Mol., Opt. Phys.*, 1988, **38**, 3098–3100.
- 8 J. P. Perdew, K. Burke and M. Ernzerhof, *Phys. Rev. Lett.*, 1996, **77**, 3865–3868.
- 9 J. F. Janak, *Phys. Rev. B: Solid State*, 1978, **18**, 7165–7168.
- 10 C.-O. Almbladh and U. von Barth, *Phys. Rev. B: Condens. Matter Mater. Phys.*, 1985, **31**, 3231–3244.
- 11 R. O. Jones and O. Gunnarsson, *Rev. Mod. Phys.*, 1989, **61**, 689–746.
- 12 M. K. Y. Chan and G. Ceder, *Phys. Rev. Lett.*, 2010, **105**, 196403.
- 13 E. Runge and E. K. U. Gross, *Phys. Rev. Lett.*, 1984, **52**, 997.
- 14 S. Botti, A. Schindlmayr, R. D. Sole and L. Reining, *Rep. Prog. Phys.*, 2007, **70**, 357.
- 15 A. Dreuw, J. L. Weisman and M. Head-Gordon, *J. Chem. Phys.*, 2003, **119**, 2943–2946.
- 16 A. Dreuw and M. Head-Gordon, *J. Am. Chem. Soc.*, 2004, **126**, 4007.
- 17 G. Onida, L. Reining and A. Rubio, *Rev. Mod. Phys.*, 2002, **74**, 601–659.
- 18 A. L. Fetter and J. D. Walecka, *Quantum Theory of Many-Particle Systems*, Dover, New York, 2003.
- 19 M. S. Hybertsen and S. G. Louie, *Phys. Rev. Lett.*, 1985, **55**, 1418–1421.
- 20 R. W. Godby, M. Schlüter and L. J. Sham, *Phys. Rev. Lett.*, 1986, **56**, 2415–2418.
- 21 M. S. Hybertsen and S. G. Louie, *Phys. Rev. B: Condens. Matter Mater. Phys.*, 1986, **34**, 5390–5413.
- 22 R. Shaltaf, G.-M. Rignanese, X. Gonze, F. Giustino and A. Pasquarello, *Phys. Rev. Lett.*, 2008, **100**, 186401.

- 23 M. J. van Setten, F. Weigend and F. Evers, *J. Chem. Theory Comput.*, 2013, **9**, 232–246.
- 24 H.-V. Nguyen, T. A. Pham, D. Rocca and G. Galli, *Phys. Rev. B: Condens. Matter Mater. Phys.*, 2012, **85**, 081101.
- 25 P. Umari, G. Stenuit and S. Baroni, *Phys. Rev. B: Condens. Matter Mater. Phys.*, 2009, **79**, 201104.
- 26 P. Umari, G. Stenuit and S. Baroni, *Phys. Rev. B: Condens. Matter Mater. Phys.*, 2010, **81**, 115104.
- 27 E. E. Salpeter and H. A. Bethe, *Phys. Rev.*, 1951, **84**, 1232–1242.
- 28 S. Albrecht, G. Onida and L. Reining, *Phys. Rev. B: Condens. Matter Mater. Phys.*, 1997, **55**, 10278–10281.
- 29 S. Albrecht, L. Reining, R. Del Sole and G. Onida, *Phys. Rev. Lett.*, 1998, **80**, 4510–4513.
- 30 M. Rohlfing and S. G. Louie, *Phys. Rev. B: Condens. Matter Mater. Phys.*, 2000, **62**, 4927–4944.
- 31 D. Rocca, Y. Ping, R. Gebauer and G. Galli, *Phys. Rev. B: Condens. Matter Mater. Phys.*, 2012, **85**, 045116.
- 32 L. E. Ramos, J. Paier, G. Kresse and F. Bechstedt, *Phys. Rev. B: Condens. Matter Mater. Phys.*, 2008, **78**, 195423.
- 33 L. X. Benedict, A. Puzder, A. J. Williamson, J. C. Grossman, G. Galli, J. E. Klepeis, J.-Y. Raty and O. Pankratov, *Phys. Rev. B: Condens. Matter Mater. Phys.*, 2003, **68**, 085310.
- 34 D. Rocca, D. Lu and G. Galli, *J. Chem. Phys.*, 2010, **133**, 164109.
- 35 V. M. Galitskii and A. B. Migdal, *Soviet Phys. JETP*, 1958, **7**, 96.
- 36 F. J. Dyson, *Phys. Rev.*, 1949, **75**, 1736–1755.
- 37 L. Hedin and S. Lundqvist, *Solid State Phys.*, 1970, **23**, 1–181.
- 38 M. Tassi, I. Theophilou and S. Thanos, *Int. J. Quantum Chem.*, 2013, **113**, 690–693.
- 39 S. Hirata, R. Podeszwa, M. Tobita and R. J. Bartlett, *J. Chem. Phys.*, 2004, **120**, 2581.
- 40 L. Dagens and F. Perrot, *Phys. Rev. B: Solid State*, 1972, **5**, 641–648.
- 41 G. Strinati, *Phys. Rev. B: Condens. Matter Mater. Phys.*, 1984, **29**, 5718–5726.
- 42 A. D. McLachlan and M. A. Ball, *Rev. Mod. Phys.*, 1964, **36**, 844–855.
- 43 L. Hedin, *Phys. Rev.*, 1965, **139**, A796–A823.
- 44 J. Schwinger, *Proc. Natl. Acad. Sci. U. S. A.*, 1951, **37**, 452–455.
- 45 J. C. Inkson, *Many-body theory of solids: an introduction*, Plenum Press, New York, 1984.
- 46 W. Kang and M. S. Hybertsen, *Phys. Rev. B: Condens. Matter Mater. Phys.*, 2010, **82**, 195108.
- 47 L. X. Benedict, E. L. Shirley and R. B. Bohn, *Phys. Rev. Lett.*, 1998, **80**, 4514–4517.
- 48 R. W. Godby, M. Schlüter and L. J. Sham, *Phys. Rev. B: Condens. Matter Mater. Phys.*, 1988, **37**, 10159–10175.
- 49 M. Rohlfing and S. G. Louie, *Phys. Rev. Lett.*, 1998, **81**, 2312–2315.
- 50 M. S. Hybertsen and S. G. Louie, *Phys. Rev. B: Condens. Matter Mater. Phys.*, 1987, **35**, 5585–5601.
- 51 R. W. Godby and R. J. Needs, *Phys. Rev. Lett.*, 1989, **62**, 1169–1172.
- 52 R. Bauernschmitt and R. Ahlrichs, *Chem. Phys. Lett.*, 1996, **256**, 454–464.
- 53 S. Baroni and R. Resta, *Phys. Rev. B: Condens. Matter Mater. Phys.*, 1986, **33**, 7017–7021.
- 54 S. Baroni, S. de Gironcoli, A. Dal Corso and P. Giannozzi, *Rev. Mod. Phys.*, 2001, **73**, 515–562.
- 55 M. Rohlfing, P. Krüger and J. Pollmann, *Phys. Rev. B: Condens. Matter Mater. Phys.*, 1995, **52**, 1905–1917.
- 56 X. Blase, C. Attaccalite and V. Olevano, *Phys. Rev. B: Condens. Matter Mater. Phys.*, 2011, **83**, 115103.
- 57 F. Bruneval, *J. Chem. Phys.*, 2012, **136**, 194107.
- 58 S. L. Adler, *Phys. Rev.*, 1962, **126**, 413–420.
- 59 N. Wiser, *Phys. Rev.*, 1963, **129**, 62–69.
- 60 M. Stankovski, G. Antonius, D. Waroquiers, A. Miglio, H. Dixit, K. Sankaran, M. Giantomassi, X. Gonze, M. Côté and G.-M. Rignanese, *Phys. Rev. B: Condens. Matter Mater. Phys.*, 2011, **84**, 241201.
- 61 H. F. Wilson, F. Gygi and G. Galli, *Phys. Rev. B: Condens. Matter Mater. Phys.*, 2008, **78**, 113303.
- 62 H. F. Wilson, D. Lu, F. Gygi and G. Galli, *Phys. Rev. B: Condens. Matter Mater. Phys.*, 2009, **79**, 245106.
- 63 H.-V. Nguyen and S. de Gironcoli, *Phys. Rev. B: Condens. Matter Mater. Phys.*, 2009, **79**, 205114.
- 64 D. Lu, Y. Li, D. Rocca and G. Galli, *Phys. Rev. Lett.*, 2009, **102**, 206411.
- 65 E. R. Davidson, *J. Comput. Phys.*, 1975, **17**, 87.
- 66 R. Car, E. Tosatti, S. Baroni and S. Leelaprute, *Phys. Rev. B: Condens. Matter Mater. Phys.*, 1981, **24**, 985–999.
- 67 D. Rocca, R. Gebauer, Y. Saad and S. Baroni, *J. Chem. Phys.*, 2008, **128**, 154105.
- 68 H. N. Rojas, R. W. Godby and R. J. Needs, *Phys. Rev. Lett.*, 1995, **74**, 1827–1830.
- 69 C. Rostgaard, K. W. Jacobsen and K. S. Thygesen, *Phys. Rev. B: Condens. Matter Mater. Phys.*, 2010, **81**, 085103.
- 70 F. Gygi and A. Baldereschi, *Phys. Rev. B: Condens. Matter Mater. Phys.*, 1986, **34**, 4405–4408.
- 71 C. Friedrich, M. C. Müller and S. Blügel, *Phys. Rev. B: Condens. Matter Mater. Phys.*, 2011, **83**, 081101.
- 72 F. Giustino, M. L. Cohen and S. G. Louie, *Phys. Rev. B: Condens. Matter Mater. Phys.*, 2010, **81**, 115105.
- 73 H. Hübener, M. A. Pérez-Osorio, P. Ordejón and F. Giustino, *Phys. Rev. B: Condens. Matter Mater. Phys.*, 2012, **85**, 245125.
- 74 J. A. Berger, L. Reining and F. Sottile, *Phys. Rev. B: Condens. Matter Mater. Phys.*, 2010, **82**, 041103.
- 75 J. A. Berger, L. Reining and F. Sottile, *Phys. Rev. B: Condens. Matter Mater. Phys.*, 2012, **85**, 085126.
- 76 F. Bruneval and X. Gonze, *Phys. Rev. B: Condens. Matter Mater. Phys.*, 2008, **78**, 085125.
- 77 G. Samsonidze, M. Jain, J. Deslippe, M. L. Cohen and S. G. Louie, *Phys. Rev. Lett.*, 2011, **107**, 186404.
- 78 A. Stan, N. E. Dahlen and R. van Leeuwen, *J. Chem. Phys.*, 2009, **130**, 114105.
- 79 T. Kotani, M. van Schilfgaarde and S. V. Faleev, *Phys. Rev. B: Condens. Matter Mater. Phys.*, 2007, **76**, 165106.

- 80 M. van Schilfgaarde, T. Kotani and S. Faleev, *Phys. Rev. Lett.*, 2006, **96**, 226402.
- 81 I. Tamblyn, P. Darancet, S. Y. Quek, S. A. Bonev and J. B. Neaton, *Phys. Rev. B: Condens. Matter Mater. Phys.*, 2011, **84**, 201402.
- 82 M. Shishkin and G. Kresse, *Phys. Rev. B: Condens. Matter Mater. Phys.*, 2007, **75**, 235102.
- 83 F. Bruneval, N. Vast and L. Reining, *Phys. Rev. B: Condens. Matter Mater. Phys.*, 2006, **74**, 045102.
- 84 B. Holm and U. von Barth, *Phys. Rev. B: Condens. Matter Mater. Phys.*, 1998, **57**, 2108–2117.
- 85 R. Del Sole, L. Reining and R. W. Godby, *Phys. Rev. B: Condens. Matter Mater. Phys.*, 1994, **49**, 8024–8028.
- 86 F. Bruneval, F. Sottile, V. Olevano, R. Del Sole and L. Reining, *Phys. Rev. Lett.*, 2005, **94**, 186402.
- 87 M. L. Tiago and J. R. Chelikowsky, *Phys. Rev. B: Condens. Matter Mater. Phys.*, 2006, **73**, 205334.
- 88 G. Onida, L. Reining, R. W. Godby, R. del Sole and W. Andreoni, *Phys. Rev. Lett.*, 1995, **75**, 818–821.
- 89 M. Rohlfing and S. G. Louie, *Phys. Rev. Lett.*, 1998, **80**, 3320–3323.
- 90 B. Walker, A. M. Saitta, R. Gebauer and S. Baroni, *Phys. Rev. Lett.*, 2006, **96**, 113001.
- 91 A. Marini, C. Hogan, M. Gruning and D. Varsano, *Comput. Phys. Commun.*, 2009, **180**, 1392–1403.
- 92 J. Deslippe, G. Samsonidze, D. A. Strubbe, M. Jain, M. L. Cohen and S. G. Louie, *Comput. Phys. Commun.*, 2012, **183**, 1269–1289.
- 93 L. Martin-Samos and G. Bussi, *Comput. Phys. Commun.*, 2009, **180**, 1416–1425.
- 94 I. Tamm, *J. Phys.*, 1945, **78**, 382.
- 95 L. X. Benedict, E. L. Shirley and R. B. Bohn, *Phys. Rev. B: Condens. Matter Mater. Phys.*, 1998, **57**, R9385–R9387.
- 96 L. X. Benedict and E. L. Shirley, *Phys. Rev. B: Condens. Matter Mater. Phys.*, 1999, **59**, 5441–5451.
- 97 P. H. Hahn, W. G. Schmidt, K. Seino, M. Preuss, F. Bechstedt and J. Bernholc, *Phys. Rev. Lett.*, 2005, **94**, 037404.
- 98 V. Olevano and L. Reining, *Phys. Rev. Lett.*, 2001, **86**, 5962–5965.
- 99 Y. Ma, M. Rohlfing and C. Molteni, *Phys. Rev. B: Condens. Matter Mater. Phys.*, 2009, **80**, 241405.
- 100 M. Gruning, A. Marini and X. Gonze, *Nano Lett.*, 2009, **9**, 2820–2824.
- 101 P. H. Hahn, W. G. Schmidt and F. Bechstedt, *Phys. Rev. B: Condens. Matter Mater. Phys.*, 2005, **72**, 245425.
- 102 D. Rocca, Z. Bai, R.-C. Li and G. Galli, *J. Chem. Phys.*, 2012, **136**, 034111.
- 103 L. Reining, V. Olevano, A. Rubio and G. Onida, *Phys. Rev. Lett.*, 2002, **88**, 066404.
- 104 S. Botti, A. Fourreau, F. m. c. Nguyen, Y.-O. Renault, F. Sottile and L. Reining, *Phys. Rev. B: Condens. Matter Mater. Phys.*, 2005, **72**, 125203.
- 105 F. Sottile, V. Olevano and L. Reining, *Phys. Rev. Lett.*, 2003, **91**, 056402.
- 106 G. Adragna, R. Del Sole and A. Marini, *Phys. Rev. B: Condens. Matter Mater. Phys.*, 2003, **68**, 165108.
- 107 A. Marini, R. Del Sole and A. Rubio, *Phys. Rev. Lett.*, 2003, **91**, 256402.
- 108 S. Sharma, J. K. Dewhurst, A. Sanna and E. K. U. Gross, *Phys. Rev. Lett.*, 2011, **107**, 186401.
- 109 V. I. Anisimov, J. Zaanen and O. K. Andersen, *Phys. Rev. B: Condens. Matter Mater. Phys.*, 1991, **44**, 943–954.
- 110 V. I. Anisimov, F. Aryasetiawan and A. I. Lichtenstein, *J. Phys.: Condens. Matter*, 1997, **9**, 767–808.
- 111 M. Cococcioni and S. de Gironcoli, *Phys. Rev. B: Condens. Matter Mater. Phys.*, 2005, **71**, 035105.
- 112 A. Currao, *Chimia*, 2007, **61**, 815–819.
- 113 J. A. Turner, *Science*, 1999, **285**, 687–689.
- 114 A. Heller, *Acc. Chem. Res.*, 1981, **14**, 154–162.
- 115 R. van de Krol, Y. Liang and J. Schoonman, *J. Mater. Chem.*, 2008, **18**, 2311–2320.
- 116 M. Weber and M. Dignam, *Int. J. Hydrogen Energy*, 1986, **11**, 225–232.
- 117 J. R. Bolton, S. J. Strickler and J. S. Connolly, *Nature*, 1985, **316**, 495–500.
- 118 A. Murphy, P. Barnes, L. Randeniya, I. Plumb, I. Grey, M. Horne and J. Glasscock, *Int. J. Hydrogen Energy*, 2006, **31**, 1999–2017.
- 119 Y. Wu, M. K. Y. Chan and G. Ceder, *Phys. Rev. B: Condens. Matter Mater. Phys.*, 2011, **83**, 235301.
- 120 J. Cheng and M. Sprik, *Phys. Rev. B: Condens. Matter Mater. Phys.*, 2010, **82**, 081406.
- 121 J. Cheng and M. Sprik, *Phys. Chem. Chem. Phys.*, 2012, **14**, 11245–11267.
- 122 S. Chen and L.-W. Wang, *Chem. Mater.*, 2012, **24**, 3659–3666.
- 123 T. Bak, J. Nowotny, M. Rekas and C. Sorrell, *Int. J. Hydrogen Energy*, 2002, **27**, 991–1022.
- 124 Chris G. Van de Walle and J. Neugebauer, *Nature*, 2003, **423**, 626–628.
- 125 W.-J. Chun, A. Ishikawa, H. Fujisawa, T. Takata, J. N. Kondo, M. Hara, M. Kawai, Y. Matsumoto and K. Domen, *J. Phys. Chem. B*, 2003, **107**, 1798–1803.
- 126 S. Trasatti, *Pure Appl. Chem.*, 1986, **58**, 955–966.
- 127 L. Weinhardt, M. Blum, M. Bar, C. Heske, B. Cole, B. Marsen and E. L. Miller, *J. Phys. Chem. C*, 2008, **112**, 3078–3082.
- 128 M. C. Toroker, D. K. Kanan, N. Alidoust, L. Y. Isseroff, P. Liao and E. A. Carter, *Phys. Chem. Chem. Phys.*, 2011, **13**, 16644–16654.
- 129 M. R. Hoffmann, S. T. Martin, W. Choi and D. W. Bahnemann, *Chem. Rev.*, 1995, **95**, 69–96.
- 130 A. Mills and S. L. Hunte, *J. Photochem. Photobiol., A*, 1997, **108**, 1–35.
- 131 A. E. Cassano and O. M. Alfano, *Catal. Today*, 2000, **58**, 167–197.
- 132 D. Bahnemann, *Sol. Energy*, 2004, **77**, 445–459.
- 133 M. Ni, M. K. Leung, D. Y. Leung and K. Sumathy, *Renewable Sustainable Energy Rev.*, 2007, **11**, 401–425.
- 134 A. Fujishima and K. Honda, *Nature*, 1972, **238**, 37–38.
- 135 G. Hodes, D. Cahen and J. Manassen, *Nature*, 1976, **260**, 312–313.
- 136 T. W. Hamann and N. S. Lewis, *J. Phys. Chem. B*, 2006, **110**, 22291–22294.

- 137 Y. Nakato, H. Yano, S. Nishiura, T. Ueda and H. Tsubomura, *J. Electroanal. Chem.*, 1987, **228**, 97–108.
- 138 R. N. Dominey, N. S. Lewis, J. A. Bruce, D. C. Bookbinder and M. S. Wrighton, *J. Am. Chem. Soc.*, 1982, **104**, 467–482.
- 139 J. R. McKone, E. L. Warren, M. J. Bierman, S. W. Boettcher, B. S. Brunschwig, N. S. Lewis and H. B. Gray, *Energy Environ. Sci.*, 2011, **4**, 3573–3583.
- 140 J. Greeley, T. F. Jaramillo, J. Bonde, I. Chorkendorff and J. K. Norskov, *Nat. Mater.*, 2006, **5**, 909–913.
- 141 Y. Tezuka, S. Shin, T. Ishii, T. Ejima, S. Suzuki and S. Sato, *J. Phys. Soc. Jpn.*, 1994, **63**, 347–357.
- 142 S. Rangan, S. Katalinic, R. Thorpe, R. A. Bartynski, J. Rochford and E. Galoppini, *J. Phys. Chem. C*, 2010, **114**, 1139–1147.
- 143 A. X. Gray, C. Papp, S. Ueda, B. Balk e, Y. Yamashita, Y. Yamashita, L. Plucinski, J. Minr, J. Braun, E. R. Ylvisaker, C. M. Schneider, W. E. Pickett, H. Ebert, K. Kobayashi and C. S. Fadley, *Nat. Mater.*, 2011, **10**, 759–764.
- 144 W. Kang and M. S. Hybertsen, *Phys. Rev. B: Condens. Matter Mater. Phys.*, 2010, **82**, 085203.
- 145 W. von der Linden and P. Horsch, *Phys. Rev. B: Condens. Matter Mater. Phys.*, 1988, **37**, 8351–8362.
- 146 L. Chiodo, J. M. Garcia-Lastra, A. Iacomino, S. Ossicini, J. Zhao, H. Petek and A. Rubio, *Phys. Rev. B: Condens. Matter Mater. Phys.*, 2010, **82**, 045207.
- 147 A. V. Krukau, O. A. Vydrov, A. F. Izmaylov and G. E. Scuseria, *J. Chem. Phys.*, 2006, **125**, 224106.
- 148 C. E. Patrick and F. Giustino, *J. Phys.: Condens. Matter*, 2012, **24**, 202201.
- 149 M. Landmann, E. Rauls and W. G. Schmidt, *J. Phys.: Condens. Matter*, 2012, **24**, 195503.
- 150 M. Mikami, S. Nakamura, O. Kitao, H. Arakawa and X. Gonze, *Jpn. J. Appl. Phys.*, 2000, **39**, L847–L850.
- 151 F. Labat, P. Baranek, C. Domain, C. Minot and C. Adamo, *J. Chem. Phys.*, 2007, **126**, 154703.
- 152 A. Janotti, J. B. Varley, P. Rinke, N. Umezawa, G. Kresse and C. G. Van de Walle, *Phys. Rev. B: Condens. Matter Mater. Phys.*, 2010, **81**, 085212.
- 153 L. Thulin and J. Guerra, *Phys. Rev. B: Condens. Matter Mater. Phys.*, 2008, **77**, 195112.
- 154 P. E. Blöchl, *Phys. Rev. B: Condens. Matter Mater. Phys.*, 1994, **50**, 17953–17979.
- 155 G. Kresse and D. Joubert, *Phys. Rev. B: Condens. Matter Mater. Phys.*, 1999, **59**, 1758–1775.
- 156 M. Shishkin and G. Kresse, *Phys. Rev. B: Condens. Matter Mater. Phys.*, 2006, **74**, 035101.
- 157 Y. Ping, D. Rocca and G. Galli, *Phys. Rev. B*, submitted.
- 158 Y. Ping, Y. Li, F. Gygi and G. Galli, *Chem. Mater.*, 2012, **24**, 4252–4260.
- 159 J. Meyer, M. Kroger, S. Hamwi, F. Gnam, T. Riedl, W. Kowalsky and A. Kahn, *Appl. Phys. Lett.*, 2010, **96**, 193302.
- 160 M. N. Huda, Y. Yan, C.-Y. Moon, S.-H. Wei and M. M. Al-Jassim, *Phys. Rev. B: Condens. Matter Mater. Phys.*, 2008, **77**, 195102.
- 161 G. A. d. Wijs, P. K. d. Boer, R. A. d. Groot and G. Kresse, *Phys. Rev. B: Condens. Matter Mater. Phys.*, 1999, **59**, 2684–2693.
- 162 F. Wang, C. Di Valentin and G. Pacchioni, *J. Phys. Chem. C*, 2011, **115**, 8345–8353.
- 163 R. Chatten, A. V. Chadwick, A. Rougier and P. J. D. Lindan, *J. Phys. Chem. B*, 2005, **109**, 3146–3156.
- 164 F. Koffyberg, K. Dwight and A. Wold, *Solid State Commun.*, 1979, **30**, 433–437.
- 165 E. Salje, *J. Appl. Crystallogr.*, 1974, **7**, 615–617.
- 166 T. Iwai, *J. Phys. Soc. Jpn.*, 1960, **15**, 1596–1600.
- 167 M. Morkel, L. Weinhardt, B. Lohmuller, C. Heske, E. Umbach, W. Riedl, S. Zweigart and F. Karg, *Appl. Phys. Lett.*, 2001, **79**, 4482–4484.
- 168 R. F. Berger and J. B. Neaton, *Phys. Rev. B: Condens. Matter Mater. Phys.*, 2012, **86**, 165211.
- 169 V. Fiorentini and A. Baldereschi, *Phys. Rev. B: Condens. Matter Mater. Phys.*, 1995, **51**, 17196–17198.
- 170 C. G. Van de Walle and R. M. Martin, *Phys. Rev. B: Condens. Matter Mater. Phys.*, 1987, **35**, 8154–8165.
- 171 H. Jiang, *J. Phys. Chem. C*, 2012, **116**, 7664–7671.
- 172 K. Schierbaum, S. Fischer, M. Torquemada, J. de Segovia, E. Romn and J. Martn-Gago, *Surf. Sci.*, 1996, **345**, 261–273.
- 173 G. Xiong, R. Shao, T. Droubay, A. Joly, K. Beck, S. Chambers and W. Hess, *Adv. Funct. Mater.*, 2007, **17**, 2133–2138.
- 174 J. P. Perdew and M. Levy, *Phys. Rev. Lett.*, 1983, **51**, 1884–1887.
- 175 S. Maldonado, K. E. Plass, D. Knapp and N. S. Lewis, *J. Phys. Chem. C*, 2007, **111**, 17690–17699.
- 176 B. Jaeckel, R. Hunger, L. J. Webb, W. Jaegermann and N. S. Lewis, *J. Phys. Chem. C*, 2007, **111**, 18204–18213.
- 177 E. Johansson, S. W. Boettcher, L. E. OLeary, A. D. Poletayev, S. Maldonado, B. S. Brunschwig and N. S. Lewis, *J. Phys. Chem. C*, 2011, **115**, 8594–8601.
- 178 L. E. OLeary, E. Johansson, B. S. Brunschwig and N. S. Lewis, *J. Phys. Chem. B*, 2010, **114**, 14298–14302.
- 179 J. M. Bolts and M. S. Wrighton, *J. Phys. Chem.*, 1976, **80**, 2641–2645.
- 180 S. D. Solares, D. J. Michalak, W. A. Goddard and N. S. Lewis, *J. Phys. Chem. B*, 2006, **110**, 8171–8175.
- 181 E. J. Nemanick, S. D. Solares, W. A. Goddard and N. S. Lewis, *J. Phys. Chem. B*, 2006, **110**, 14842–14848.
- 182 Y. Kanai and A. Selloni, *J. Am. Chem. Soc.*, 2006, **128**, 3892–3893.
- 183 Y. Li and G. Galli, *Phys. Rev. B: Condens. Matter Mater. Phys.*, 2010, **82**, 045321.
- 184 Y. Li, L. O'Leary, N. S. Lewis and G. Galli, *J. Phys. Chem. C*, 2013, DOI: 10.1021/jp3124583.
- 185 X. Blase, X. Zhu and S. G. Louie, *Phys. Rev. B: Condens. Matter Mater. Phys.*, 1994, **49**, 4973–4980.
- 186 S. Lebègue, B. Arnaud, M. Alouani and P. E. Bloechl, *Phys. Rev. B: Condens. Matter Mater. Phys.*, 2003, **67**, 155208.
- 187 K. Hricovini, R. Günther, P. Thiry, A. Taleb-Ibrahimi, G. Indlekofer, J. E. Bonnet, P. Dumas, Y. Petroff, X. Blase, X. Zhu, S. G. Louie, Y. J. Chabal and P. A. Thiry, *Phys. Rev. Lett.*, 1993, **70**, 1992–1995.
- 188 K.-H. Hellwege and O. Madelung, *Semiconductors. Physics of Group IV Elements and III-V Compounds*,

- Landolt-Brnstein, New Series, Group III, Springer, Berlin, 1982, vol. 17, Pt. A.
- 189 R. Hunger, R. Fritsche, B. Jaeckel, W. Jaegermann, L. J. Webb and N. S. Lewis, *Phys. Rev. B: Condens. Matter Mater. Phys.*, 2005, **72**, 045317.
- 190 B. Jaeckel, R. Hunger, L. J. Webb, W. Jaegermann and N. S. Lewis, *J. Phys. Chem. C*, 2007, **111**, 18204–18213.
- 191 S. Maldonado, K. E. Plass, D. Knapp and N. S. Lewis, *J. Phys. Chem. C*, 2007, **111**, 17690–17699.
- 192 G. P. Lopinski, B. J. Eves, O. Hul'ko, C. Mark, S. N. Patitsas, R. Boukherroub and T. R. Ward, *Phys. Rev. B: Condens. Matter Mater. Phys.*, 2005, **71**, 125308.
- 193 A. Aliano, Y. Li, G. Cicero and G. Galli, *J. Phys. Chem. C*, 2010, **114**, 11898–11902.
- 194 S. Grimme, *J. Comput. Chem.*, 2006, **27**, 1787–1799.
- 195 S. Yang, D. Prendergast and J. B. Neaton, *Nano Lett.*, 2012, **12**, 383–388.
- 196 M. Landmann, T. Köhler, S. Köppen, E. Rauls, T. Frauenheim and W. G. Schmidt, *Phys. Rev. B: Condens. Matter Mater. Phys.*, 2012, **86**, 064201.
- 197 M. Cardona and G. Harbeke, *Phys. Rev.*, 1965, **137**, A1467–A1476.
- 198 N. Hosaka, T. Sekiya, C. Satoko and S. Kurita, *J. Phys. Soc. Jpn.*, 1997, **66**, 877–880.
- 199 J. Pascual, J. Camassel and H. Mathieu, *Phys. Rev. Lett.*, 1977, **39**, 1490–1493.
- 200 B. Cole, B. Marsen, E. Miller, Y. Yan, B. To, K. Jones and M. Al-Jassim, *J. Phys. Chem. C*, 2008, **112**, 5213–5220.
- 201 Z. Hussain, *Appl. Opt.*, 2002, **41**, 6708–6724.
- 202 J. F. Owen, K. J. Teegarden and H. R. Shanks, *Phys. Rev. B: Solid State*, 1978, **18**, 3827–3837.
- 203 F. Cor, M. G. Stachiotti, C. R. A. Catlow and C. O. Rodriguez, *J. Phys. Chem. B*, 1997, **101**, 3945–3952.
- 204 D. Lynch, R. Rosei, J. Weaver and C. Olson, *J. Solid State Chem.*, 1973, **8**, 242–252.
- 205 Q. Mi, Y. Ping, Y. Li, B. Cao, B. S. Brunshwig, P. G. Khalifah, G. A. Galli, H. B. Gray and N. S. Lewis, *J. Am. Chem. Soc.*, 2012, **134**, 18318–18324.
- 206 R. Hull, *Properties of Crystalline silicon*, INSPEC, The Institute of Electrical Engineers, London, United Kingdom, 1999, p. 395.
- 207 R. R. L. Zucca and Y. R. Shen, *Phys. Rev. B: Solid State*, 1970, **1**, 2668–2676.
- 208 J. Noffsinger, E. Kioupakis, C. G. Van de Walle, S. G. Louie and M. L. Cohen, *Phys. Rev. Lett.*, 2012, **108**, 167402.
- 209 G. G. Macfarlane, T. P. McLean, J. E. Quarrington and V. Roberts, *Phys. Rev.*, 1958, **111**, 1245–1254.
- 210 G. Giorgi, M. Palummo, L. Chiodo and K. Yamashita, *Phys. Rev. B: Condens. Matter Mater. Phys.*, 2011, **84**, 073404.
- 211 X.-Q. Gong and A. Selloni, *J. Phys. Chem. B*, 2005, **109**, 19560–19562.
- 212 A. Selloni, *Nat. Mater.*, 2008, **8**, 613–615.
- 213 A. G. Thomas, W. R. Flavell, A. K. Mallick, A. R. Kumarasinghe, D. Tsoutsou, N. Khan, C. Chatwin, S. Rayner, G. C. Smith, R. L. Stockbauer, S. Warren, T. K. Johal, S. Patel, D. Holland, A. Taleb and F. Wiame, *Phys. Rev. B: Condens. Matter Mater. Phys.*, 2007, **75**, 035105.
- 214 H. Cheng and A. Selloni, *Phys. Rev. B: Condens. Matter Mater. Phys.*, 2009, **79**, 092101.
- 215 M. Ni, M. K. Leung, D. Y. Leung and K. Sumathy, *Renewable Sustainable Energy Rev.*, 2007, **11**, 401–425.
- 216 M. Rohlffing and S. G. Louie, *Phys. Rev. Lett.*, 1999, **83**, 856–859.
- 217 O. Pulci, A. Marini, M. Palummo and R. Del Sole, *Phys. Rev. B: Condens. Matter Mater. Phys.*, 2010, **82**, 205319.
- 218 M. Palummo, N. Witkowski, O. Pluchery, R. Del Sole and Y. Borenstein, *Phys. Rev. B: Condens. Matter Mater. Phys.*, 2009, **79**, 035327.
- 219 P. H. Hahn, W. G. Schmidt and F. Bechstedt, *Phys. Rev. Lett.*, 2001, **88**, 016402.
- 220 W. Richter and J.-T. Zettler, *Appl. Surf. Sci.*, 1996, **100–101**, 465–477.
- 221 D. E. Aspnes and A. A. Studna, *Phys. Rev. Lett.*, 1985, **54**, 1956–1959.
- 222 J. F. McGilp, *Prog. Surf. Sci.*, 1995, **49**, 1–106.
- 223 S. Selci, P. Chiaradia, F. Ciccacci, A. Cricenti, N. Sparvieri and G. Chiarotti, *Phys. Rev. B: Condens. Matter Mater. Phys.*, 1985, **31**, 4096–4098.
- 224 P. Chiaradia, A. Cricenti, S. Selci and G. Chiarotti, *Phys. Rev. Lett.*, 1984, **52**, 1145–1147.
- 225 M. Palummo, G. Onida, R. Del Sole and B. S. Mendoza, *Phys. Rev. B: Condens. Matter Mater. Phys.*, 1999, **60**, 2522–2527.
- 226 M. Rohlffing, P. Krüger and J. Pollmann, *Phys. Rev. B: Condens. Matter Mater. Phys.*, 1993, **48**, 17791–17805.
- 227 W. G. Schmidt, S. Glutsch, P. H. Hahn and F. Bechstedt, *Phys. Rev. B: Condens. Matter Mater. Phys.*, 2003, **67**, 085307.
- 228 Y. Lin, G. Yuan, R. Liu, S. Zhou, S. W. Sheehan and D. Wang, *Chem. Phys. Lett.*, 2011, **507**, 209–215.
- 229 A. Kay, I. Cesar and M. Grtzel, *J. Am. Chem. Soc.*, 2006, **128**, 15714–15721.
- 230 C. Santato, M. Odziemkowski, M. Ulmann and J. Augustynski, *J. Am. Chem. Soc.*, 2001, **123**, 10639–10649.
- 231 L. E. Brus, *J. Chem. Phys.*, 1984, **80**, 4403–4409.
- 232 R. van de Kol and M. Gratzel, *Photoelectrochemical Hydrogen Production*, Springer, 2012, p. 59.
- 233 F. E. Osterloh, *Chem. Soc. Rev.*, 2013, DOI: 10.1039/c2cs35266d.
- 234 K. Sivula, R. Zboril, F. Le Formal, R. Robert, A. Weidenkaff, J. Tucek, J. Frydrych and M. Gratzel, *J. Am. Chem. Soc.*, 2010, **132**, 7436–7444.
- 235 C. Santato, M. Ulmann and J. Augustynski, *Adv. Mater.*, 2001, **13**, 511–514.
- 236 K. Sayama, A. Nomura, T. Arai, T. Sugita, R. Abe, M. Yanagida, T. Oi, Y. Iwasaki, Y. Abe and H. Sugihara, *J. Phys. Chem. B*, 2006, **110**, 11352–11360.
- 237 C. M. McShane and K.-S. Choi, *J. Am. Chem. Soc.*, 2009, **131**, 2561–2569.
- 238 G. K. Mor, K. Shankar, M. Paulose, O. K. Varghese and C. A. Grimes, *Nano Lett.*, 2005, **5**, 191–195.
- 239 X. Feng, K. Shankar, O. K. Varghese, M. Paulose, T. J. Latempa and C. A. Grimes, *Nano Lett.*, 2008, **8**, 3781–3786.

- 240 J. Su, X. Feng, J. D. Sloppy, L. Guo and C. A. Grimes, *Nano Lett.*, 2011, **11**, 203–208.
- 241 S. W. Boettcher, E. L. Warren, M. C. Putnam, E. A. Santori, D. Turner-Evans, M. D. Kelzenberg, M. G. Walter, J. R. McKone, B. S. Brunschwig, H. A. Atwater and N. S. Lewis, *J. Am. Chem. Soc.*, 2011, **133**, 1216–1219.
- 242 M. D. Kelzenberg, D. B. Turner-Evans, M. C. Putnam, S. W. Boettcher, R. M. Briggs, J. Y. Baek, N. S. Lewis and H. A. Atwater, *Energy Environ. Sci.*, 2011, **4**, 866–871.
- 243 J. R. Maiolo, H. A. Atwater and N. S. Lewis, *J. Phys. Chem. C*, 2008, **112**, 6194–6201.
- 244 M. Bruno, M. Palummo, A. Marini, R. Del Sole and S. Ossicini, *Phys. Rev. Lett.*, 2007, **98**, 036807.
- 245 L. Yang, C. D. Spataru, S. G. Louie and M. Y. Chou, *Phys. Rev. B: Condens. Matter Mater. Phys.*, 2007, **75**, 201304.
- 246 A. R. Guichard, R. D. Kekatpure, M. L. Brongersma and T. I. Kamins, *Phys. Rev. B: Condens. Matter Mater. Phys.*, 2008, **78**, 235422.
- 247 M. Palummo, F. Iori, R. Del Sole and S. Ossicini, *Phys. Rev. B: Condens. Matter Mater. Phys.*, 2010, **81**, 121303.
- 248 M. Palummo, S. Ossicini and R. Del Sole, *Phys. Status Solidi B*, 2010, **247**, 2089–2095.
- 249 L. Zhang, J.-W. Luo, A. Franceschetti and A. Zunger, *Phys. Rev. B: Condens. Matter Mater. Phys.*, 2011, **84**, 075404.
- 250 Y. Ping, D. Rocca, D. Lu and G. Galli, *Phys. Rev. B: Condens. Matter Mater. Phys.*, 2012, **85**, 035316.
- 251 J. G. Vilhena, S. Botti and M. A. L. Marques, *Appl. Phys. Lett.*, 2010, **96**, 123106.
- 252 C. A. Rozzi, D. Varsano, A. Marini, E. K. U. Gross and A. Rubio, *Phys. Rev. B: Condens. Matter Mater. Phys.*, 2006, **73**, 205119.
- 253 S. Ismail-Beigi, *Phys. Rev. B: Condens. Matter Mater. Phys.*, 2006, **73**, 233103.
- 254 M. V. Wolkin, J. Jorne, P. M. Fauchet, G. Allan and C. Delerue, *Phys. Rev. Lett.*, 1999, **82**, 197–200.
- 255 Q. Zhang and S. C. Bayliss, *J. Appl. Phys.*, 1996, **79**, 1351–1356.
- 256 K. Yabana and G. F. Bertsch, *Int. J. Quantum Chem.*, 1999, **75**, 55–66.
- 257 M. A. L. Marques, X. López, D. Varsano, A. Castro and A. Rubio, *Phys. Rev. Lett.*, 2003, **90**, 258101.
- 258 M. A. L. Marques and S. Botti, *J. Chem. Phys.*, 2005, **123**, 014310.
- 259 C. Zhang, D. Donadio, F. Gygi and G. Galli, *J. Chem. Theory Comput.*, 2011, **7**, 1443–1449.
- 260 C. Zhang, J. Wu, G. Galli and F. Gygi, *J. Chem. Theory Comput.*, 2011, **7**, 3054–3061.
- 261 A. J. Cohen, P. Mori-Sánchez and W. Yang, *Science*, 2008, **321**, 792–794.